
# The interplay between excitonic and magnetic dynamics in 2D chromium trihalides

Masoumeh Kazemi

Faculty of Physical Sciences
University of Iceland
2025

# THE INTERPLAY BETWEEN EXCITONIC AND MAGNETIC DYNAMICS IN 2D CHROMIUM TRIHALIDES

Masoumeh Kazemi

Dissertation submitted in partial fulfillment of a
*Philosophiae Doctor* degree in Physics

Advisor
Prof. Ivan Shelykh

PhD committee
Prof. Ivan Shelykh (supervisor)
Dr. Andrejs Kudlis (co-supervisor)
Dr. Pavel F. Bessarab
Dr. Christian Schneider

Opponents
Prof. Mikhail Katsnelson
Dr. Martin Veis

Faculty of Physical Sciences
School of Engineering and Natural Sciences
University of Iceland
Reykjavik, January 2025

The interplay between excitonic and magnetic dynamics in 2D chromium trihalides

Dissertation submitted in partial fulfillment of a *Philosophiae Doctor* degree in Physics



Faculty of Physical Sciences
School of Engineering and Natural Sciences
University of Iceland
Dunhagi 3
IS-107, Reykjavik, Reykjavik
Iceland

Telephone: 525 4000

Bibliographic information:
Masoumeh Kazemi, 2025, *The interplay between excitonic and magnetic dynamics in 2D chromium trihalides*, PhD dissertation, Faculty of Physical Sciences, University of Iceland, 170 pp.

ISBN: 978-9935-9826-0-5

Printing: Háskólaprent, Fálkagata 2, 107 Reykjavík
Reykjavik, Iceland, January 2025

*This thesis is dedicated to my dear mother and my dear father, for their endless kindness and support.*

*And to my lovely husband, Hamed, for his amour, encouragement and continued support.*

# Abstract

The present thesis is devoted to a theoretical analysis of optical excitonic response and magnetic lattice dynamics in two-dimensional materials, in particular monolayers of $CrI_3$. Combining the results of DFT and Bethe-Salpeter simulations describing excitons with Landau-Lifshits equation describing the dynamics of lattice spin, we construct a microscopic theory of complex magneto-excitonic response and in particular the effect of resonant optical magnetization switching. In addition, our investigation focuses on achieving tunable control over the life time and size of magnetic topological defects such as Néel-type skyrmion. Which is important for advancing information storage and processing applications. We also demonstrate that the possibility of the formation of magnetic skyrmions, together with large excitonic Zeeman splitting leads to giant scattering asymmetry, which is the necessary prerequisite for the excitonic anomalous Hall effect. This will make it possible to simulate various phenomena associated with coupled exciton-skyrmion dynamics.

# Útdráttur

Þessi ritgerð er tileinkuð fræðilegri greiningu á ljósfræðilegri örvunarviðbrögðum og segulmögnuðum grindardýnamík í tvívíðum efnum, sérstaklega einlögum af CrI3. Með því að sameina niðurstöður frá DFT og Bethe-Salpeter hermunum, sem lýsa örvunum, við Landau-Lifshitz jöfnu sem lýsir dýnamík snúnings í grindinni, byggjum við upp örsmáa kenningu um flókna segul-örvunarsvörun og sérstaklega áhrif ómskiptandi ljóssegulmögnunar. Að auki beinist rannsókn okkar að því að ná stillanlegri stjórn á líftíma og stærð segulmögnuðra topologískra galla eins og skyrmiona af Néel-gerð. Þetta er mikilvægt til að þróa forrit fyrir upplýsingageymslu og -vinnslu. Við sýnum einnig fram á að möguleikinn á myndun segulskyrmiona ásamt stórri örvunarlegri Zeeman-skiptingu leiðir til gríðarlegrar ósamhverfu í dreifingu, sem er nauðsynleg forsenda fyrir örvunarlega óvenjulega Hall-áhrifinu. Þetta mun gera mögulegt að herma ýmis fyrirbæri sem tengjast samtvinnaðri örvunar-skyrmion-dýnamík.

# Acknowledgements

First of all, I am very grateful to my supervisor Professor Dr. Ivan Shelykh for his amazing guidance and continuous support throughout this four-year journey. I was very fortunate to have the opportunity to work with him. I also thank him for providing such interesting and novel problems and ideas. Therefore, I was able to obtain a deeper understanding of not only one aspect of physics but more. He has given me invaluable understanding and knowledge that has deeply impacted both my academic and personal life.

I would like to thank Dr. Andrejs Kudlis for all his valuable assistance and expertise. Working with him was a pleasure and enjoyable. Thanks to our meetings and effective discussion, which I have gained a great depth of knowledge. I would like to thank Dr. Pavel F.Bessarab for opening the door for me to the fascinating world of magnetism. I also would like to thank Dr. Vanik Shahnazaryan for all efficient discussion. Many thanks to my opponents Professor Mikhail Katsnelson and Dr. Martin Veis.

I would like to express my gratitude to all the wonderful people I met during my PhD journey especially Dr. Luciano Henrique Siliano Ricco for all his help, Dr. Mohammad Badarneh, Dr. Grzegorz Kwiatkowski and Vladyslav Kuchkin. Your presence made this challenging experience not only feasible, but truly enjoyable. In addition, I would like to give thanks for all the kindness and positive energy I have received from people in the Tourism faculty especially Tinna Gunnarsdóttir.

I also thanks the administrative staff at Tæknigarður especially Íris Davíðsdóttir, Harpa Sigurðardóttir, Anna Kristín Árnadóttir. In particular, I am very grateful of Icelandic Research Fund (IRF), grant number 2410537-051.

Special thanks to my brother, my sisters and my dear parents for their endless kindness and support. Particularly, I would like to express my deepest thanks to my dear husband, Dr. Hamed Gramizadeh for always being by my side throughout this journey. His constant support and encouragement has been my strength, especially during the most challenging times. He believed in me even when I doubted myself, and his faith in my abilities gave me the strength to keep going and not give up.

# Table of Contents

# 1 Introduction

The synthesis of low-dimensional materials demonstrating excitonic response with magnetic dynamics represents a highly significant and successful achievement in the field of condensed matter physics. This integration holds immense importance for both current and future devices reliant on magnetic memory. Combining these two distinct material properties not only presents a fundamentally intriguing challenge but also holds considerable technological appeal. It is crucial and potentially promising to bridge excitonic and magnetic exploration and innovation in memory technologies. In addition it is also the purpose of science to verify that advancements adhere to the principles of energy conservation and sustainability.

It is important to understand that the dimension of a system can considerably affect its physical properties. Despite living in a three-dimensional (3D) world, technology has recently enabled the experimental realization of structures with a lower dimensionality. Two-dimensional (2D) systems are particularly interesting. In recent decades, two-dimensional magnetic materials have opened the door to optically controlled magnetism and the development of novel functional devices. These are 2D antiferromagnets $MPS_3$ (M=Ni, Fe, Mn), and ferromagnets $CrX_3$ (X=I, Br). A noteworthy example in this project is the chromium trihalide family, e.g., $CrI_3$. In this material the magnetic $Cr^{3+}$ ions are arranged on the honeycomb lattice vertices surrounded by non-magnetic $I^-$ ions.

Moreover, in systems with broken structural inversion symmetry chiral exchange between magnetic atoms emerge leading to the formation of localized, topological textures such as skyrmions and beyond. Co-existence of skyrmions and excitons in a single system allows us to hypothesize that these entities can interact resulting in new phenomena that are surprisingly and extremely interesting. It is noteworthy that skyrmion is a topologically protected spin configuration that has the potential to be utilized as an information carrier in ultradense memories. Such texture can be stabilized through competition of exchange, Dzyaloshinskii–Moriya (DM), and anisotropy interactions. Additionally, it has been predicted that DM interaction plays a significant role in the creation of skyrmions. When isolated skyrmions were first discovered, significant attention was paid to them due to their ability to be easily manipulated by magnetic, optical, and electrical means. This work will make it possible to simulate various phenomena associated with coupled exciton-skyrmion dynamics.

This thesis consists of six chapters, which are described in the following paragraphs:

Chapter 1, provides a clear overview of the project's primary purpose and goals, as well as some fundamental and necessary information. We will start with an explanation of classical Atomistic Hamiltonian, Landau-Lifshitz-Gilbert equation and magnetic skyrmion then it will end with the description of Excitons.

In chapter 2, we focus on a microscopic theory of optical switching whereby a Hamiltonian is constructed that accounts for localized magnetic moments and excitons and the interactions with, and between, them. The model is parameterized from a combination of DFT calculations and Bethe-Salpeter approach. we demonstrate the possibility of a tunable control of macroscopic magnetization switching in monolayer of $CrI_3$.

In chapter 3, we focus on exploring the new concept of all-optical control over skyrmion configurations in $CrI_3$ monolayer. This work investigates the manipulation of skyrmion size using circularly polarized light pulses, showcasing the potential for energy-efficient control of these topological magnetic structures without an external magnetic field. Two-dimensional magnets hosting excitons thus represent a promising platform for the control of topological magnetic structures by light.

Chapter 4 is devoted to the potential creation of magnetic topological defects such as Néel skyrmions in conjunction with enormous excitonic Zeeman splitting leads to the gigantic scattering asymmetry, which is a precondition for the excitonic anomalous Hall effect. We also demonstrate that the diamagnetic effect can also lead to the localization of excitons on the skyrmion, which sometimes breaks the inversion symmetry. As a result, it can permit the production of magneto-excitonic quantum dots whose properties can be adjusted.

Chapter 5 is devoted to the conclusion. We give a brief summary of the main points of the thesis.

Chapter 6 contains the appendices. We provide supplementary information with more details to the relevant sections of the thesis. After appendices, we list 3 publications on which this thesis is based.

# 1.1 Magnetic states

In this section the purpose is to introduce and review some fundamental and significant concepts related to the study of magnetic textures such as skyrmions. We will begin with a description of the total energy of a magnetic system, then we will elaborate on each term.

## 1.1.1 The classical Atomistic Hamiltonian

Using the Extended Heisenberg Model, it can be described the magnetic structure of a system as a lattice of classical spins. These classical spins are each located on an atomic lattice site $i$. Let's consider a magnetic system including of $N$ localized atoms, where the $i$th atom carries a net magnetic moment $\boldsymbol{m}_i = \boldsymbol{M}_i/\mu_i$ with $i = 1, ..., N$. Here $\boldsymbol{m}_i$ is a unit vector corresponding to the orientation of the total magnetic moment $\boldsymbol{M}_i$ as well as here $\mu_i$ is denoted to the magnitude of the moment in units of Bohr magneton $\mu_B$. There are a number of noteworthy combined magnetism phenomena that emerge from the interaction of atomic magnetic moments. These phenomena include ferromagnetism, where spins align in parallel; spin structures, characterized by a helical arrangement of spins, and magnetic skyrmions, which are topologically stable spin configurations.

The definition of classical atomistic Hamiltonian includes four terms as follows:

$$H = H_{ex} + H_{DM} + H_{ani} + H_{Zee} \tag{1.1}$$

First Heisenberg exchange ($H_{ex}$), second Dzyaloshinskii–Moriya interaction ($H_{DM}$), third one is magnetic anisotropy ($H_{ani}$) and the last term corresponds to the interaction between the magnetic moments with an external magnetic field or Zeeman energy ($H_{Zee}$). We also compared the atomistic and continuous models through the connection between materials parameters. See Appendix 6.1.

### 1.1.1.1 Exchange interaction

The symmetric exchange interaction, first introduced by Heinsenberg in the 1920's [1], promotes the alignment of two neighboring magnetic moments $\boldsymbol{m_i}$ and $\boldsymbol{m_j}$. It should be noted that the exchange interaction has a strong but short-range effect, as well as in the Heisenberg model only the nearest neighbors are considered.

Based on the assumption of an atomic lattice of magnetic moments and according to

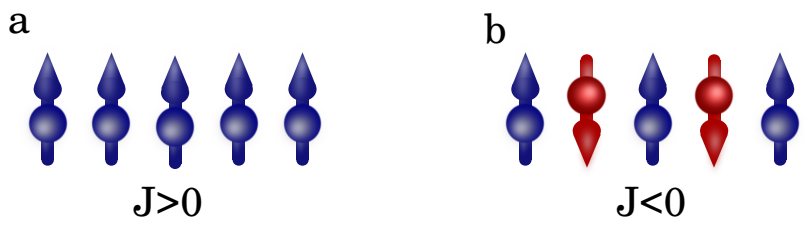


*Figure 1.1:* a) Ferromagnetic state, An illustration of the parallel alignment of magnetic moments ($J > 0$). b) Antiferromagnetic state, An antiparallel alignment of magnetic moments ($J < 0$). In blue and red, magnetic moments are displayed in an upward and downward direction, respectively.

the discrete model we can determine the exchange energy as following:

$$H_{ex} = -\frac{1}{2} \sum_{<i,j>} J_{i,j}(\boldsymbol{m_i} \cdot \boldsymbol{m_j}) \tag{1.2}$$

Where $\boldsymbol{m_i}$ represents the unit vector pointing in the direction of $i$th magnetic moment at the site $i$. The summation is carried out over all of the nearest neighbors $<i, j>$ of magnetic moments. Here $J_{i,j}$ is a coupling constant describing the strength of the interaction for pairs of neighboring magnetic moments $\boldsymbol{m_i}$ and $\boldsymbol{m_j}$.

Interaction types are determined by the sign of the coupling constant $J_{i,j}$: positive for ferromagnetic interactions and negative for antiferromagnetic interactions. Ferromagnetic and Antiferromagnetic states have collinear magnetic moments aligned parallel or antiparallel to one axis, respectively. In the case of a positive sign of $J$ ($J$>0), when the energy reaches the minimum a parallel alignment of magnetic moment $i$ can be expected, this state is called ferromagnetic state (FM) which is shown in the Fig 1.1(a). Whereas Antiferromagnetic states (AFM) typically exhibit antiparallel alignments between magnetic moments due to negative exchange parameters $J$<0 [2, 3]. As it is shown in the Fig 1.1(b) of the nearest neighbour exchange interaction.

#### 1.1.1.2 Dzyaloshinskii-Moriya Interaction

The antisymmetric exchange interaction is known as the Dzyaloshinskii-Moriya (DM) interaction. The first proposal was made by Dzyaloshinskii in 1958 [4]. For an explanation of why certain antiferromagnetic materials show weak, yet nonzero spontaneous magnetisation. In his view, the magnetic configuration had a direct connection to the crystal's symmetry. A few years later, in 1960, Moriya demonstrated how to calculate this additional exchange by considering the spin-orbit coupling (SOC) in a crystal lacking inversion symmetry [5].

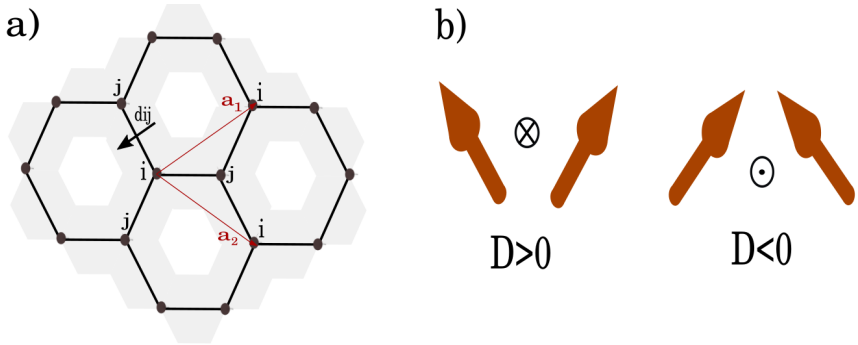


*Figure 1.2:* a) The DM unit vector in honeycomb lattice, $\boldsymbol{d}_{ij}$ is perpendicular to the vector pointing from site $i$ to $j$, shown with a black arrow. The lattice vectors are represented by the red arrows $\boldsymbol{a_1}$ and $\boldsymbol{a_2}$. b) The sign of the DM interaction parameter, positive DM indicates that spins are pointing outward and negative DM indicates that spins are pointing inward.

DM interaction is recognized to play a crucial role at the interface between ferromagnetic (FM) and heavy nonmagnetic (NM) metals to create topological textures called magnetic skyrmions, which are very attractive for ultra-dense information storage and spintronic devices [3, 6, 7]

On a discrete lattice, the DM interaction energy is given by the formula:

$$H_{DM} = -D \sum_{<i,j>} \boldsymbol{d}_{ij} \cdot (\boldsymbol{m_i} \times \boldsymbol{m_j}) \tag{1.3}$$

Here, $D$ is Dzyaloshinskii-Moriya interaction parameters and $\boldsymbol{d}_{ij} = \boldsymbol{r}_{ij} \times \boldsymbol{e}_z / |\boldsymbol{r}_{ij}|$ is the DM unit vector with $\boldsymbol{e}_z$ and $\boldsymbol{r}_{ij}$ being the unit vector along the $z$ direction and the vector pointing from site $i$ to site $j$, respectively. As shown in figure 1.2(a) that $\boldsymbol{d}_{ij}$ is perpendicular to the vector pointing from site $i$ to $j$. We also introduced $\boldsymbol{m}_i$ previously.

It is important to note that the chirality of spin structures is defined by DM interaction parameter sign. Positive($D > 0$) and negative($D < 0$) sign results in certain chirality and opposite chirality, respectively. According to figure 1.2(b).

#### 1.1.1.3 Magnetic anisotropy

Magnetic anisotropy plays a crucial role in various magnetic phenomena, including magnetic domain formation, magnetization reversal processes, and magnetic state stability. Understanding and controlling this interaction is of significant importance in the design and development of magnetic materials for various applications. These include magnetic storage devices, spintronics, and magnetic sensors.

It is common in magnetic materials for the magnetic moment to have a preferred axes; these are known as easy axes, which are energically the easiest axes to align along. In other words, energy is lowest when magnetic moments are aligned along easy axes and highest when magnetic moments are aligned along hard axes. The contribution due to magnetic anisotropy is written in the form:

$$H_{ani} = -K \sum_i \left(\boldsymbol{m_i} \cdot \boldsymbol{e_k}\right)^2 \tag{1.4}$$

Where $\boldsymbol{e_k}$ is the unit vector along the anisotropy axis which represents the direction of the easy axis and $K$ is the anisotropy constant. Based on the sign of the anisotropy constant, a positive sign of $K$ gives rise to an easy axis parallel to $\boldsymbol{e_k}$ and an easy plane can be realized for a negative sign of $K$, resulting in an orientation of magnetization perpendicular to $\boldsymbol{e_k}$.

#### 1.1.1.4 Zeeman interaction

Zeeman energy arises from the interaction of magnetic moments with an external magnetic field. In general, the Zeeman interaction tends to rotate the magnetization in the same direction as the magnetic field applied to it.

$$H_{Zee} = -\mu \sum_i \boldsymbol{B} \cdot \boldsymbol{m_i} \tag{1.5}$$

Where $\mu$ is the magnitude of the magnetic moments, which is assumed to be the same at all lattice sites and $\boldsymbol{B}$ is the external magnetic field.

## 1.2 Landau-Lifshitz-Gilbert equation

Landau-Lifshitz-Gilbert (LLG) equation is a fascinating nonlinear equation both from mathematical and physical points of view. For many years, a well-accepted model, the LLG equation has been used to study and describe magnetization dynamics in ferromagnetic materials.

First Landau and Lifshitz introduced the generally used equation of motion for interacting magnetic moments of an atomic lattice in 1935 [8], See equation 1.6. Landau and Lifshitz included a double cross product damping term in addition to the precession term which known as the Landau-Lifshitz (LL) equation:

$$\frac{d\boldsymbol{m}_i}{dt} = -\gamma \boldsymbol{m}_i \times \boldsymbol{B}_i^{\text{eff}} + \frac{\lambda}{m} \boldsymbol{m}_i \times \left(\boldsymbol{m}_i \times \boldsymbol{B}_i^{\text{eff}}\right), \tag{1.6}$$

Where, $\boldsymbol{m}_i$ is the magnetic moment of an atom at site $i$ in the lattice, $\gamma$ is the gyromagnetic ratio and $\boldsymbol{B}_i^{\text{eff}}$ is effective magnetic field. The first term at the right hand side of the equation is precessional motion and second term is responsible for the damping contribution.

Figure 1.3 shows how the magnetic moment becomes aligned gradually with the effective magnetic field because of the contribution of damping under the effect of an effective magnetic field $\boldsymbol{B}_i^{\text{eff}}$, where the damping motion is perpendicular on the precessional one . As a matter of fact, in the precession term, the size of the damping is controlled by the parameter $\lambda$. In 2004 Gilbert introduced another form of the damping term which known as Landau-Lifshitz-Gilbert (LLG) equation[9].

$$\frac{d\boldsymbol{m_i}}{dt} = -\gamma \boldsymbol{m}_i \times \boldsymbol{B}_i^{\text{eff}} + \frac{\alpha}{m} \left(\boldsymbol{m}_i \times \frac{d\boldsymbol{m_i}}{dt}\right), \tag{1.7}$$

Here $\alpha$ is Gilbert damping parameter which plays a critical role in the dynamics of magnetization. As the damping parameter $\alpha$ increases, stabilization or convergence to a steady state occurs faster and the overall speed decreases. There is a close correspondence between the Landau–Lifshitz–Gilbert equation and the Landau–Lifshitz equation with a small effect of the damping parameter. Meaning that when damping ($\alpha$) increases, the difference between the two solutions (see equation 1.6 and 1.7) becomes more obvious and clear. [10].

A critical aspect of Atomistic model is establishing a practical expression for $\boldsymbol{B}_i^{\text{eff}}$. The effective magnetic field $\boldsymbol{B}_i^{\text{eff}}$, defined in equation 1.8, should take into account all interactions that each magnetic moments may potentially experience. Such as

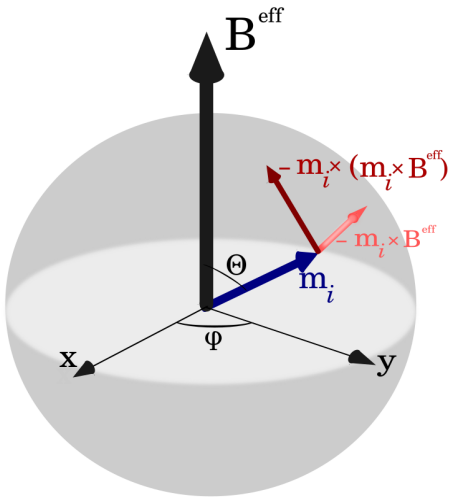


*Figure 1.3:* Schematic of the magnetization dynamics of Landau-Lifshitz equation. Black and blue arrows represent the effective magnetic field ($\boldsymbol{B}^{\text{eff}}$) and magnetic moment ($\boldsymbol{m}_i$), respectively. The directions of the precession term ($-\boldsymbol{m}_i \times \boldsymbol{B}^{\text{eff}}$) and the damping term ($-\boldsymbol{m}_i \times (\boldsymbol{m}_i \times \boldsymbol{B}^{\text{eff}})$) are denoted by pink and red arrows, respectively. The orientation of magnetic moment is presented by the polar ($\theta$) angle and an azimuthal ($\varphi$) angle.

exchange interactions between neighboring magnetic moments, Dzyaloshinskii–Moriya (DM) interaction, and interactions with external magnetic field.

In order to accurately describe and predict the behavior and dynamics of the magnetic moments in a system under consideration, it is imperative to include these diverse interactions within the magnetic field. A definition of it would be as follows:

$$\boldsymbol{B}_i^{\text{eff}} = -\frac{\partial H}{\partial \boldsymbol{m}_i}. \tag{1.8}$$

The magnetic field, characterized by its dimension of energy, can be obtained by taking the functional derivative of the applied model Hamiltonian, see equation 1.1. $H$ is Extended Heisenberg Hamiltonian, as described in the previous section.

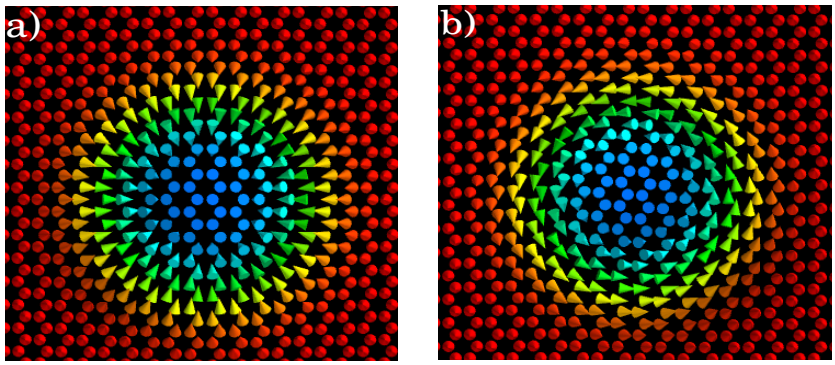


*Figure 1.4:* Topview of two different magnetic skyrmions. a) Néel skyrmion b) Blokh skyrmion. Red and blue colors indicate upward and downward direction of spin, respectively.

## 1.3 Magnetic skyrmion

Magnetic skyrmion is a remarkable spin texture of non-collinear order with integer topological winding number or charge. Skyrmions, originally introduced as a topological soliton in non-linear field theory by Tony Skyrme, a British high energy physicist in 1961 [10]. After about three decades Bogdanov and Yablonskii predicted magnetic skyrmion in a real material in 1989 [13]. Following this discovery, a lot of researchers conducted investigations and experiments on the formation and creation of skyrmions by applying magnetic field and electric field, the imaging of the process of skyrmion nucleation, the manipulation of skyrmions radius and the dynamics of skyrmions [14–16]. It is important to note that, as part of this work, we control skyrmions' size by all optical means(see chapter 3 ).

Among several types of skyrmions, this fascinating particle-like, here we just classified it as either Néel or Bloch type; depending on the orientation of the axis of rotation of the magnetic moments relative to the radial direction. Néel-type skyrmions have their rotational axis perpendicular to the radial direction, while Bloch-type skyrmions have their axis parallel to the radial direction. This distinction is illustrated in Figure 1.4. In this figure red and blue colors indicate upward and downward direction of spin, respectively. As well as Fig 1.4 (a) represents Néel skyrmion and Fig 1.4 (b) represents Blokh skyrmion in ferromagnetic background. For this project, we will only consider the Néel skyrmion type.

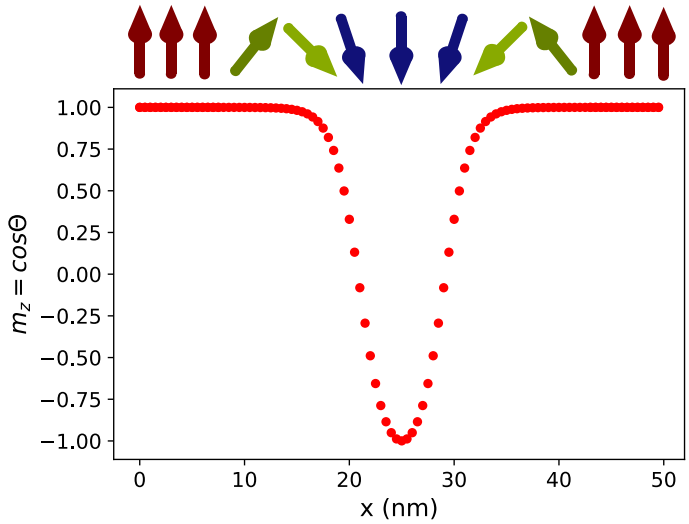


*Figure 1.5:* Skyrmion profile of the z-component of the corresponding magnetization ($m_z$). The magnetic structure of the skyrmion is displayed above the plot. Here blue and red arrows correspond to spin down and up of the magnetization, respectively. As the figure illustrates the direction of the magnetization at the center of skyrmion is down meaning that $m_z = -1$

Magnetic skyrmion has non-zero skyrmion number or topological charge. The topological charge $Q$ is defined in a Cartesian coordinate system and is given by the integral over the two-dimensional plane of the skyrmion configuration:

$$Q = \frac{1}{4\pi} \int \mathbf{m} \cdot (\frac{\partial \mathbf{m}}{\partial x} \times \frac{\partial \mathbf{m}}{\partial y}) dx dy \tag{1.9}$$

Where $\mathbf{m}$ is magnetic unit vector that representing the direction of the local magnetization. For instance here for both Néel and Bloch skyrmions that is shown in Figure 1.4 , the topological charge $Q$ is an integer and is $Q = 1$. The fact is, topological charge determines how many times the spin configuration wraps around the unit sphere. It is relevant to note that the topological charge for a ferromagnetic state, where all spins are uniformly aligned and an antiferromagnetic state, is zero ($Q = 0$). It is important to note that the vector of magnetization $\mathbf{m}$ is described in terms of spherical coordinates in the magnetic state which is shown in Figure 1.3. $\mathbf{m}$ = (sin$\theta$ cos$\varphi$, sin$\theta$ sin$\varphi$, cos$\theta$ ) with the polar ($\theta$) and azimuthal ($\varphi$) angle. Meaning that $m_x$ = sin$\theta$ cos$\varphi$, $m_y$ = sin$\theta$ sin$\varphi$ and $m_z$ = cos$\theta$.

### 1.3.1 Skyrmion profile

The skyrmion profile can be described by a 360° domain wall using the following ansatz:

$$\theta\left(r;c,w\right)=2arctan\left(\frac{cosh\frac{c}{w/2}}{sinh\frac{r}{w/2}}\right) \tag{1.10}$$

Where $\theta$ defines the polar angle of the magnetization at position $r$. Here, the magnitude of $r$ is the distance from the skyrmion center. $c$, $\omega$ are the fit parameters that $c$ approximately corresponds to the center of the domain wall and $\omega$ indicates the domain wall width. It should be noted that, the skyrmion profile obtained in experiments has already been described using 360° domain wall profiles [17]. Figure 1.5 illustrates skyrmion profile of the z-component of the magnetization $m_z = \cos\theta$ versus $x$ in $nm$. Where blue and red arrows correspond to the spin down (the centre of skyrmion) and up (the edge of skyrmion) in the direction of magnetization, respectively.

### 1.3.2 Skyrmion radius

The skyrmion radius is fundamental quantities of a skyrmion that depends sensitively on material parameters such as exchange energy, anisotropy, Dzyaloshinskii–Moriya interaction, and magnetic field [71] (Detailed information about them can be found in Section 1.1). A magnetic skyrmion consists of a central region where magnetic moments are aligned in the opposite direction of spins at the boundary of skyrmion. As it is shown in 1.7, It is obvious that skyrmion's radius ($R$) and domail wall ($W$) are in the central region. This figure is taken from [71]. The orientation of the spin along the $x$ axis is shown below the schematic figure. Blue and red arrows define the direction of spin toward down and up, respectively.

Various studies have shown that the size of isolated skyrmions tends to increase with the Dzyaloshinskii–Moriya interaction strength, and reduces with magnetic anisotropy and external magnetic field [12, 71]. For instance, figure 1.6 demonstrates the skyrmion radius versus magnetic field and DM interaction in honeycomb lattice in $CrI_3$ monolayer.

Skyrmion size is really critical and crucial for some reasons specially in terms of data storage density and energy efficiency. Compared to big size skyrmion, smaller one is more stable and it is more easy to move and manipulate. An example that can be understood, skyrmions represent bits of data, so when we have smaller sizes, we can have more skyrmions in the same physical space. One of the part of this work is controlling skyrmion size by all optical means that is more convenient than old approach like magnetic field [18].

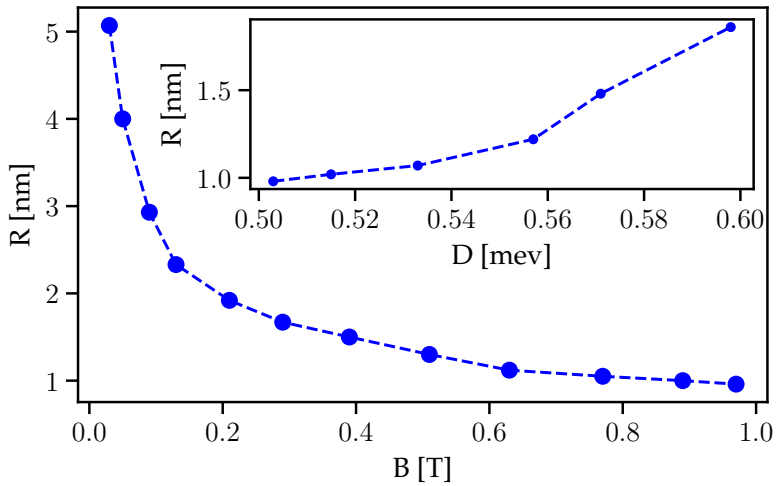


*Figure 1.6:* Skymion radius versus magnetic field and DM interaction in honeycomb lattice. As the magnetic field and DM interaction increase, the radius of the skyrmion decreases and increases respectively.

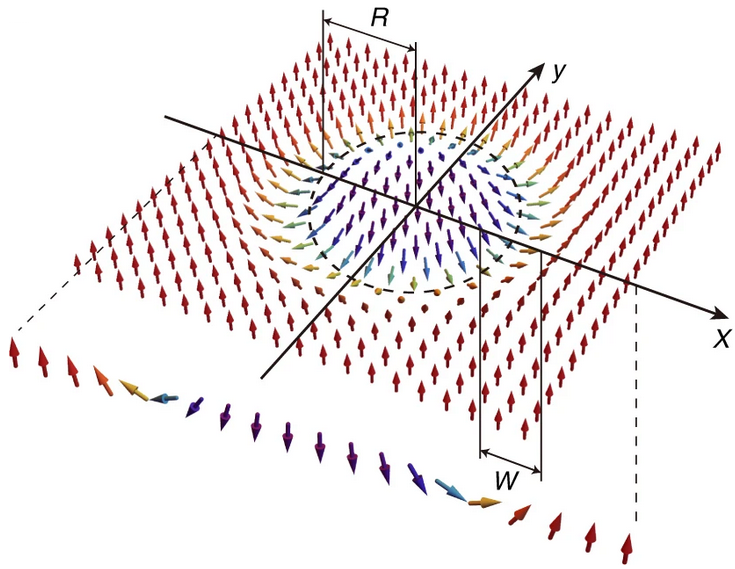


*Figure 1.7:* The schematic representation of the skyrmion radius $R$ and its domain wall $W$. Here blue and red arrows correspond to the orientation of the spin toward down and up, respectively. The figure is from Ref [71].

There are various ways in which skyrmion size and radius can be defined, as follows: first let's point out to the skyrmion size which has been proposed by Bogdanov and Hubert [67].

$$R_{BH} = r_0 - \theta(r_0)(\frac{d\theta}{dr})^{-1} \tag{1.11}$$

Here, $r_0$ is the steepest slope point and $\theta$ is the polar angle of the magnetization which is defined in equation 1.10.

The following equation is the definition of skyrmion center and how we can achieve to skyrmion radius: In the centre of skyrmion $m_z = 1$ and an alternative definition of the skyrmion center that is more relevant to experiments is based on the out-of-plane component of the spin [20],

$$\mathbf{R}(x, y) = \frac{\int \mathbf{r}(m_z - 1)d\mathbf{r}}{\int (m_z - 1)d\mathbf{r}} \tag{1.12}$$

And in order to obtain the radius of the skyrmion, it is feasible to calculate it between $m_z = 1$ center of skyrmion and where magnetic moments lie in plane $m_z = 0$. It would be better to comment we implemented both definitions of skyrmion radius for this project.

## 1.4 Band structure of materials

The electronic band structure of a solid or simply band structure is unique and distinct to each material or crystal due to the arrangement and type of atoms. Depending on the materials, the band structure can reveal a large amount of information such as electronic, magnetic and optical properties. The band structure of a crystal describes the range of energy levels that electrons are allowed to occupy. But the energy range that they are forbidden from occupying, known as band gap energy. In other words, band gap energy in solid-state physics, for insulators and semiconductors, refers to the difference of energy between the top of the valence band and the bottom of the conduction band (in the figure 1.8(a) you will find more information about the valence band and the conduction band).

As density functional theory (DFT) has been an invaluable tool for understanding, analyzing and studying the band structure and optical properties of materials. In this work we calculate the electronic structure of ferromagnetic $CrI_3$ monolayer from the first principles using the density functional theory. DFT approach obtains a ground state structure of the system, by solving Hohenberg-Kohn theorems and later extended by Kohn-Sham(KS) equations, often in Local Density Approximation (LDA), which utilizes the exchange and correlation energies from the free electron gas. Actually LDA is a class of approximations to the exchange–correlation (XC) energy functional in density functional theory (DFT) that depends only on the value of the electron density at each point, In other words, the system behaves like a uniform electron gas with the same local electron density. In general, for a spin-unpolarized system, a local-density approximation for the exchange-correlation energy is a function of the local electron density $\rho(\mathbf{r})$ which is written as follows:

$$E_{\mathrm{xc}}^{\mathrm{LDA}}[\rho(\mathbf{r})] = \int \rho(\mathbf{r})\, \epsilon_{\mathrm{xc}}(\rho(\mathbf{r}))\, d\mathbf{r} \tag{1.13}$$

Meaning that at each point in space, the exchange-correlation energy is approximately equal as if the electrons at that point experience the same environment as in a uniform electron gas with the same density. Where, $E_{\mathrm{xc}}^{\mathrm{LDA}}[\rho(\mathbf{r})]$ is the exchange-correlation energy, $\rho(\mathbf{r}) = \sum_i |\psi_i(\mathbf{r})|^2$ is the electron density, and $\epsilon_{\mathrm{xc}}(\rho(\mathbf{r}))$ is the exchange-correlation energy per electron for a uniform electron gas with density $\rho(\mathbf{r})$. To arrive at LDA, the exchange-correlation potential is often decomposed into the exchange and correlation parts as: $E_{XC} = E_X + E_C$. Exchange interactions are caused by the Pauli exclusion principle and correlation effects are due to Coulomb interactions. The exchange energy:

$$E_x^{LDA}[\rho(\mathbf{r})] = -\frac{4}{3}\left(\frac{3}{\pi}\right)^{1/3} \int \rho^{4/3}(\mathbf{r})\, d\mathbf{r} \tag{1.14}$$

The correlation energy in general:

$$E_{\mathrm{c}}^{\mathrm{LDA}}[\rho(\mathbf{r})] = \int \rho(\mathbf{r})\, \epsilon_{\mathrm{c}}(\rho(\mathbf{r}))\, d\mathbf{r} \tag{1.15}$$

Non-local interactions aren't considered in LDA, since it takes into account only the local value of the electron density. In the section 1.6 we discuss more about the properties and band structure of the $CrI_3$ monolayer from DFT approach.

## 1.5 Excitons

Perfect semiconductors have a completely filled valence band and an empty conduction band at their ground state. It is known as the "zero" energy or "vacuum" state. Additionally, its total momentum (K) and angular momentum (L) are both zero, and its spin S = 0 [21].

The electronic absorption process in a semiconductor occurs through an interband transition with an energy above the bandgap that promotes electrons from the valence band (VB) to the conduction band (CV). During this transition, a hole (with the opposite sign compared to the charge of the electron) remains in the valence band, and because of the Coulomb attraction between them electron and hole form a quasi particle which is called an exciton (see Fig 1.8 (a)), meaning that it is the bound state of an electron and a hole that behaves like a single particle with distinct properties from that of the individual electrons and holes [48].

The presence of excitons can be detected in semiconductor materials like gallium arsenide (GaAs), two-dimensional materials like graphene, and transition metal dicholcogenides (TMDs), like molybdenum disulfide ($MoS_2$) and $CrI_3$ monolayers. In this project we focus exclusively on the chromium(III) iodide ($CrI_3$) monolayer.

### 1.5.1 Frenkel and Wannier excitons

It is shown in Fig 1.8 (b) that excitons can be classified into two categories based on their size and formation mechanism: Wannier-Mott and Frenkel excitons. The Frenkel and Wannier excitons concepts were introduced in the second half of the 1930s [23, 24]. Frenkel excitons are tightly bound excitons which have a smaller radius than the lattice constant or they have a radius similar in magnitude to the crystal unit cell or atomic radii, and Wannier-Mott excitons, which have a larger radius, where the distance between the electron and the hole greatly exceeds the size of a unit cell [21].

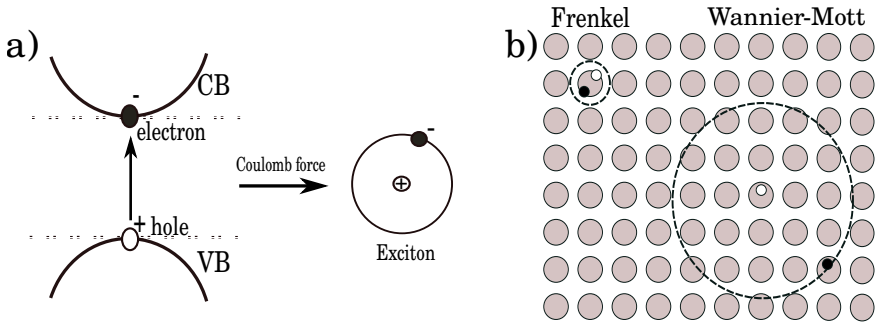


*Figure 1.8:* a) The schematic figure illustrates the creation of exciton. Small black circle is negative electron in conduction band and small white circle is positive hole in valence band. b) Two types of exciton, Frenkel and Wannier-Mott from left to right respectively.

The Wannier exciton typically occurs in inorganic semiconductors, while the Frenkel exciton often found in insulators or organic semiconductors.

In a Wannier-Mott exciton, the Hamiltonian can be written as a two-body bound state with Coulomb interactions between electrons and holes that produces a hydrogen-like problem with a Coulomb potential term: $U = -e^2/4\pi\epsilon_0\epsilon|\boldsymbol{r}_e - \boldsymbol{r}_h|$.

$$H = -\frac{\hbar^2}{2m_c}\Delta_e^2 - \frac{\hbar^2}{2m_v}\Delta_h^2 - \frac{e^2}{4\pi\epsilon_0\epsilon|\boldsymbol{r}_e - \boldsymbol{r}_h|} \tag{1.16}$$

Where the first two terms describe the kinetic energies of the electron with the effective mass $m_c$ and the hole with the effective mass $m_v$ respectively, and the last term describes the Coulomb attraction between the electron and hole. Here $\epsilon$ is the effective dielectric permittivity.

An exciton absorption spectrum plays a crucial role in providing information on the energy levels and dynamics within a material, as well as the electronic and optical properties of that material. The best illustration of absorption spectrums of a direct band-gap semiconductor can be seen in Fig 1.9. Initially, photons with an energy less than band gap energy incident to a semiconductor then electrons move from VB to CB without absorbing(dashed blue line in Fig 1.9), but once the photons have an energy greater than band gap energy, absorption occurs (red line in Fig 1.9). As an analogy to the hydrogen Rydberg series, the exciton states are named accordingly with principal quantum number (n = 1, 2, 3...) and orbital labels (s, p, d...). In this figure the

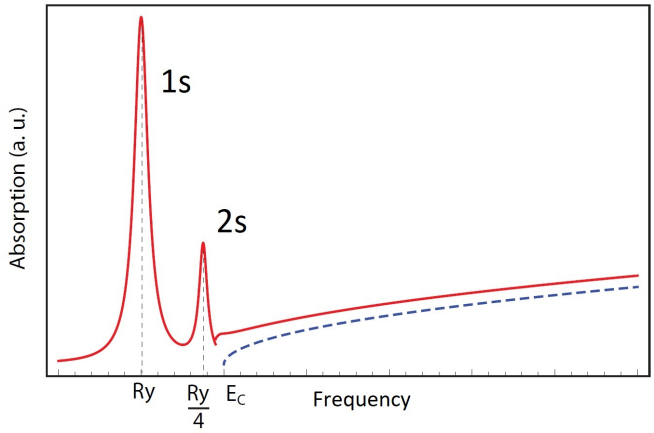


*Figure 1.9:* Schematic representation of an absorption spectrum as a function of frequency for a typical semiconductor is shown in this figure. Exciton transitions are shown by red solid lines, while no transitions are shown by blue dashed lines.

ground state (n = 1) and excited state (n > 1) are often referred to as 1s, 2s, 3s and so on. The absorption of excitonic resonances decreases with the increasing exciton principal quantum number n, that representing gradual weakening of the light-matter interaction.

In the present thesis we deal with the Frenkel type of excitons. Therefore, to describe the Hamiltonian of Frenkel exciton, based on the BSE equation, we describe it as follows: As the excitonic binding energy and optical absorption spectra will not be accurately predicted by standard DFT (ground-state theory), therefore, we calculate the exciton absorption spectrum using the numerical solution of the Bethe-Salpeter equation, which is designed specifically to describe the excited states, such as electron-hole pairs (excitons). The BSE is a very successful theoretical method used to study and investigate particles' bound states, as well as to calculate the electronic and optical properties of systems. In other words the Bethe-Salpeter equation approach uses information from DFT calculations to analyze excited state properties. The diagram of BSE is shown in Fig 1.10. This figure first describes that using Kohn-Sham equation it is possible to obtain non interacting particles energies and provide the fundamental band gap as well as GW Approximation corrects the Kohn-Sham energies and provide more accurate band gap for single-particle excitations, then BSE equation combines excitonic effects ( two-particle excitations) to calculate optical excitation.

The BSE equation was developed by Hans Bethe and Edwin Salpeter in the 1950s, which originally formulated for the case of relativistic particles [26]. Then the first absorption spectrum within BSE was obtained by Hanke and Sham in 1980, which the

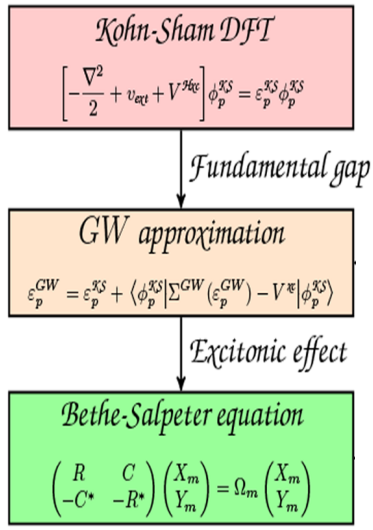


*Figure 1.10:* The general workflow of Bethe-Salpeter Equation to calculate the optical excitation. Kohn-Sham equation is used to obtain single-particle energies and band gaps, followed by GW Approximation to include many-body effects, then BSE equation combines excitonic effect to calculate optical excitation.

combined electron-hole interactions introduced in the example Si significant modifications of the theoretical absorption strength [27].

The general form of BSE Hamiltonian is like following:

$$\sum_{c'v'} H^{BSE}_{cvc'v'} A^{n}_{c'v'} = E^{n} A^{n}_{cv} \tag{1.17}$$

Where, $H^{BSE}_{cvc'v'}$ are the matrix elements of the BSE Hamiltonian for excitons, $A^{n}_{cv}$ and $E^{n}$ are the $n$th exciton wave function and energy, respectively. The indices $c$ ($c'$), $v$ ($v'$), denote the conduction band and valence band. There are distinct approaches to calculating the BSE Hamiltonian. Here we calculated the Hamiltonian using the Tamm-Dancoff approximation, which is particularly well-suited for wide-gap semiconductors. Actually, this approximation disregards the coupling between resonance and anti-resonance poles while preserving the Hermitian character of the Hamiltonian [143].

## 1.6 $CrI_3$ monolayer. A promising candidate

One of the most intriguing and promising candidates among the various two-dimensional (2D) magnetic materials is Chromium Triiodide ($CrI_3$). Due to its unique optical effects, such as excitonic formation and interaction and magnetic properties. Both experimental and theoretical research demonstrates that chromium triiodide ($CrI_3$) is a two-dimensional (2D) ferromagnetic (FM) semiconductor [28, 29]. Throughout the following sections, we will discuss the crystal and electronic structures of $CrI_3$ monolayers.

The magnetic chromium atoms in the $CrI_3$ monolayer form a honeycomb lattice organization similar to the crystal lattice of graphene, with each chromium atom surrounded by six iodine atoms arranged in an octahedron [44]. The structure of both top and side view of the monolayer is shown in Fig 1.11. In this figure the black thin line presents the unit cell consisting of two magnetic Cr atoms. Which the atoms of chromium and iodine are represented by red and pink spheres, respectively.

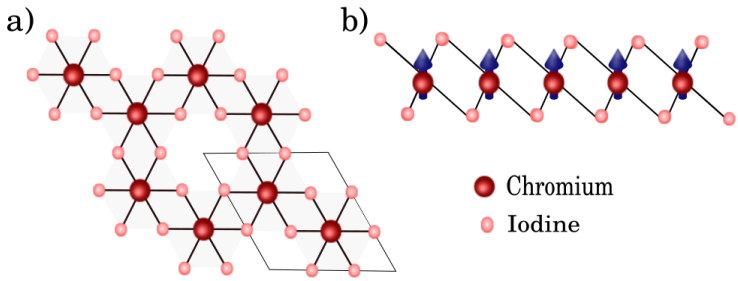


*Figure 1.11:* Crystal structure of ferromagnetic monolayer $CrI_3$. a) top view and b) side view of ferromagnetic monolayer $CrI_3$. The atoms of chromium and iodine are represented by red and pink spheres, respectively. The unit cell of $CrI_3$ consists of two Cr atoms and six I atoms, with the Cr atoms forming a honeycomb structure.

It is important to note that using density functional theory (DFT) and a few different way, we can predict and analyze the existence and properties of excitons in $CrI_3$ monolayers. As it was mentioned previously, in this work we investigate the electronic band structure of ferromagnetic monolayers via first principles calculations employing DFT approach, which is shown in Fig 1.12.

The computations were executed using the GPAW package [51, 150]. We use the cut-off energy of 600 eV for the plane-wave basis set and the LDA exchange-correlation functional incorporating spin-orbit effects [52]. To avoid interaction between periodic images, We use a slab model with a vacuum thickness of 16 Å in the supercell. Lattice constant for the $CrI_3$ ferromagnetic monolayer was determined via crystal lattice relax-

ation procedures, resulting in the value of 6.69 Å. The force convergence criteria were set at 1 meV/Å per atom. Spin-orbit effects are treated at the level of perturbation theory.

In this thesis, the exciton spectrum was acquired utilizing the GPAW implementation of the Bethe-Salpeter equation [53–56]. Screened Coulomb potential expressions were derived with the dielectric cutoff of 50 eV, 200 electronic bands, and a 2D truncated Coulomb potential [55]. The exciton basis was configured with 16 valence bands and 14 conduction bands on a 6×6 grid of the first Brillouin zone. To address the DFT bandgap issue, a scissor operator was employed to adjust the bandgap value to the experimental value of 2.59 eV in agreement with previous calculations [122, 124]. We found the transition energy of the brightest low-lying exciton is $E_X = 1.65$ eV, which is observed in the experimental differential reflection spectrum as the T2 state [114], as well as in theoretical studies [122, 124, 125].

The corresponding exciton state is formed near direct bandgap at the crystallographic point G by the electrons mainly located in the $m_c = 5.09m_0$, and the holes in the upper valence band with effective mass $m_v = -0.59m_0$, with $m_0$ being the free electron mass. The exciton has a clearly defined spin structure since it is completely localised in the upper valence band and the three lower conduction bands, which have strictly determined spin direction.

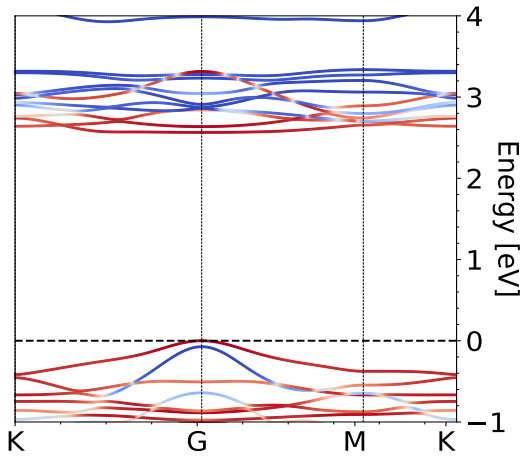


*Figure 1.12:* Electronic band structure of ferromagnetic monolayer $CrI_3$ using density functional theory (DFT) with showing the direct bandgap at point G. Colour codes the spin projection value.

# 2 A microscopic theory of all-optical magnetization control.

Bright excitons in ferromagnetic monolayers $CrI_3$ efficiently interact with lattice magnetization, which makes all-optical resonant magnetization control possible in this material. Using the combination of ab-initio simulations within Bethe-Salpeter approach, semiconductor Bloch equations, and Landau-Lifshitz equations, we construct a microscopic theory of this effect. By solving numerically the resulting set of coupled equations describing the dynamics of atomic spins and spins of the excitons, we demonstrate the possibility of a tunable control of macroscopic magnetization of a sample.

## 2.1 Introduction

Efficient control of the properties of layered structures is an important problem in both fundamental and applied research. In particular, a great demand exists for the development of optimal methods for control of magnetic characteristics of materials. This is not surprising, given the ever-increasing requirements for data-recording capacities of magnetic memory elements. The most important of them are compactness, energy efficiency, and recording speed. Regarding the latter, all-optical methods for the magnetic order manipulation look very promising as compared to traditional approaches based on the application of external magnetic field, as device operating frequencies can be enhanced by several orders of magnitude.

To date, there already exists a number of theoretical [31, 32] and experimental works confirming the possibility of all-optical magnetization switching (AOMS) in a variety of magnetic compounds, including GdFeCo [33–37] and TbFeCo [38] ferrimagnetic alloys, as well as in Pt/Co or Co/Gd multilayers [39, 40]. Among all candidates where such a reorientation of magnetization is possible, materials combining ferromagnetic ordering with the presence of robust bright excitons are of particular interest [41]. The examples of such materials are chromium trichalides, such as $CrCl_3$, $CrBr_3$ or $CrI_3$ [42].

In the present work, we take $CrI_3$ as an example, but the reported results should

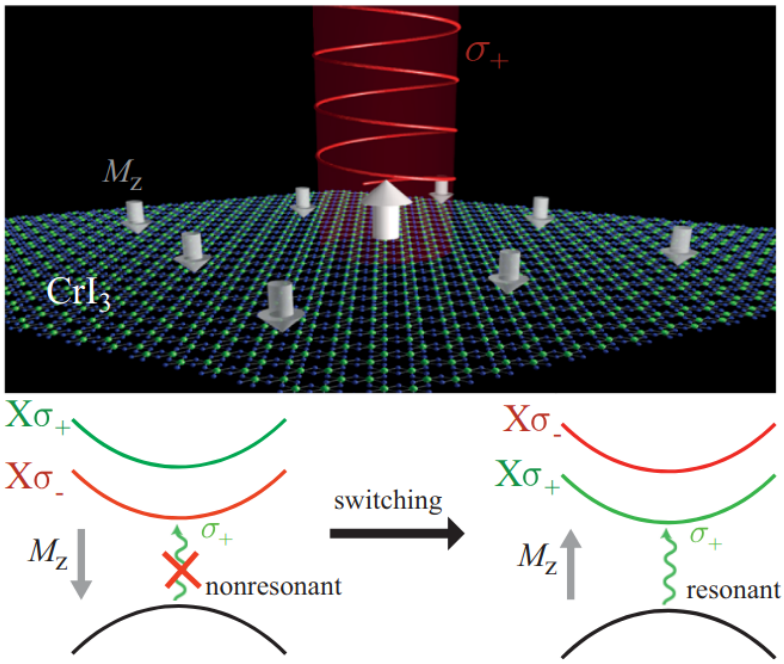


*Figure 2.1:* Upper panel: The magnetization of a monolayer of $CrI_3$ is reversed by irradiating it with circularly polarized light. Lower panel: The mechanism of the magnetization switching. The circular polarized pump is not resonant with the corresponding exciton transition if magnetization is pointing down (left part), but becomes resonant if the direction of the magnetization is switched. The figure is from [49].

remain qualitatively the same for other members of the family. In the material we consider, the $Cr^{3+}$ ions are arranged on the honeycomb lattice vertices surrounded by non-magnetic $I^-$ ions [43]. Being a 2D Ising ferromagnet, this material demonstrates robust optical excitonic response, with record high values of excitonic binding energies and oscillator strengths [44], exceeding even the values reported for transition metal dichalcogenides [45–48].

The combination of such unique properties allowed some of us to propose that chromium trihalides were suitable candidates for polarization-sensitive resonant optical magnetization switching [49], which was later on confirmed experimentally [41]. The process of magnetic reorientation is connected with the transfer of angular momentum from excitons (electron-hole pairs) to the quasi-localized $d$-electrons of the Cr atoms, and corresponding phenomenological theory was developed in Ref. [49]. The general idea of

the current work is coming from Ref [49], which it was demonstrated that the presence of the robust bright excitonic resonances coupled to lattice magnetization leads to the possibility of polarization-sensitive magnetization switching in the nonlinear regime. The main idea of the proposed effect is illustrated schematically in Fig. 2.1. The band structure of a monolayer of $CrI_3$ is shown schematically in lower panel of Fig. 2.1. As $CrI_3$ is a direct band semiconductor, the optical transition is allowed from the top of the valence band to the bottom of the conduction band. Attraction between an electron and a hole leads to the formation of strongly coupled bright excitons.

Depending on the direction of the magnetization of a sample, ground-state excitons can be excited by $\sigma_+$ or $\sigma_-$ light. Consider the geometry shown in the lower panel of Fig. 2.1, when the ground state corresponds to $\sigma_-$ excitation and we send a pulse of $\sigma_+$ light in resonance with it. As the $\sigma_+$ transition is strongly offset in energy due to the giant Zeeman splitting produced by the lattice magnetization, the absorption of $\sigma_+$ photons is only virtual. However, this virtual absorption creates an effective magnetic field, which tends to invert the magnetization. This process is favored by the fact that the magnetization switch will make optical absorption resonant, and if the intensity of the optical pump exceeds some threshold value, it finally happens.

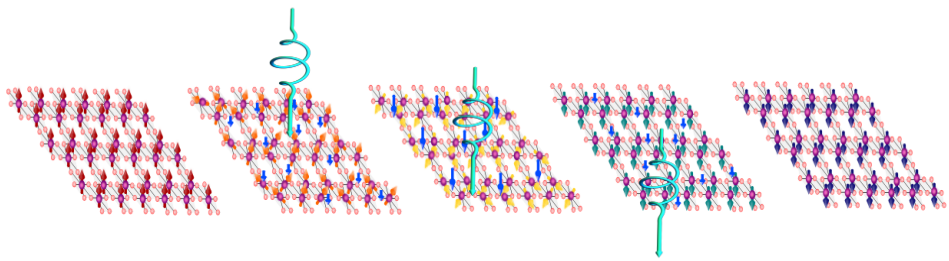

*Figure 2.2:* Schematic representation of the process we are studying. $CrI_3$ layer is irradiated with circular polarized light. The polarization vector lies in the sample plane. Due to pumping, excitons appear in the system, which themselves have an effective magnetic moment. Depending on the polarization of light, the magnetic moment can be oriented both up and down.

However, the full microscopic theory of the effect is still absent. In the current chapter, we make an attempt to construct such microscopic theory. We apply the well-established atomistic spin dynamics (ASD) formalism as basis of our work and couple it with the equations for the exciton dynamics by adding the terms describing the interaction between the spins of the excitons and the magnetic lattice. Numerical solution of the resulting set of equations allows us to analyze in detail the dynamics of the magnetization switching in real space and time.

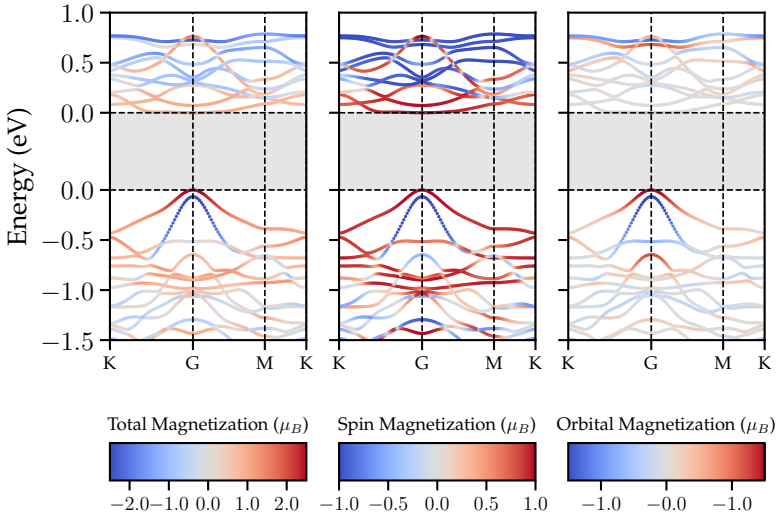


*Figure 2.3:* DFT band structure of excitons in $CrI_3$ monolayer with lattice constant 6.69 Å. The color code shows total, spin, and orbital magnetization in the left, middle and right panel, respectively. The bandgap energy E=2.59 eV is indicated by gray shading. According to the first Brillouin zone grid, we have selected 16 valence bands and 14 conduction bands for the exciton basis.

This chapter is organized as follows: First we present the DFT band structure and absorption spectrum of $CrI_3$ monolayer. Second we introduce the model Hamiltonian for coupled systems of excitons, lattice spins and the dynamic equations. Finally, we will provide a summary of the most important results of our research at the end of this chapter, including the dependence of the switching properties on the parameters of the incident light beam.

As it was mentioned in section 1.6, we calculate the electronic structure of ferromagnetic $CrI_3$ monolayer from the first principles using the density functional theory (DFT), Here the value of the lattice constant is 6.69 Å. For more details see section 1.6.

As shown in Fig. 2.2, we can see a schematic representation of the process we are studying in this chapter. $CrI_3$ monolayer is illuminated with circular polarized light that is shown in a light green color. As a result of pumping, excitons form in the system (they are shown with small blue arrows on the monolayer), which themselves have effective magnetic moments. In this figure from left to right, magnetic moments switch from up(red arrows) to down(blue arrows).

In Fig. 2.3, we demonstrate the band structure of the $CrI_3$ monolayer with color bars for the orbital, spin and total magnetization which are shown below the main figures. The bandgap of 2.59 eV is highlighted by the gray area. The analysis of the

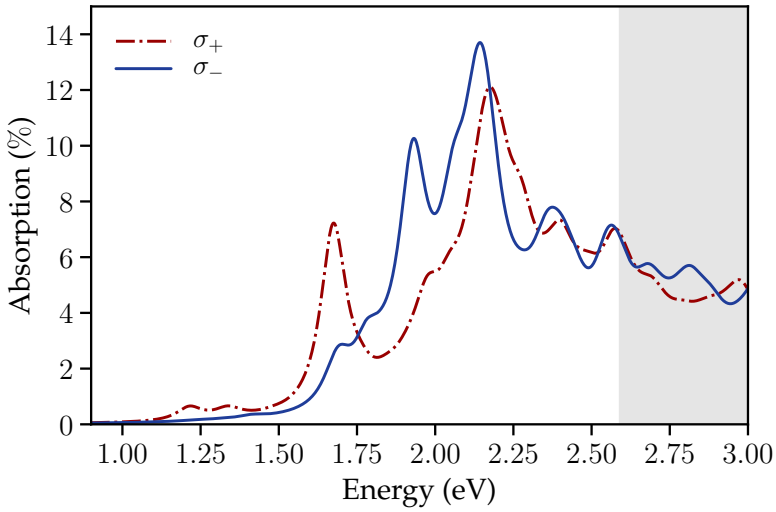


*Figure 2.4:* Absorption spectrum of $CrI_3$ sample for two circular polarizations. The solid line and the dashed line correspond to the $\sigma_-$ and $\sigma_+$ polarizations, respectively. The bandgap energy E=2.59 eV is indicated by gray shading.

polarization-resolved absorption spectrum of the $CrI_3$ monolayer is shown in Fig. 2.4. As one can see, there is a remarkable difference in the absorption of the $\sigma_+$ and $\sigma_-$ components. The prominent absorption peaks in both absorption profiles are related to the excitonic transitions.

Naturally, if the magnetization of the sample is inverted, the absorption curves corresponding to opposite polarizations interchange. This forms the basis of the magnetization switching mechanism: for a given pump frequency and polarization, the magnetic sublattice tends to orient its magnetization so as to maximize the absorption [49].

## 2.2 The model Hamiltonian

The total energy $E$ of the system includes three terms:

$$H = H_{\mathrm{m}} + H_{\mathrm{exc}} + H_{\mathrm{s}}, \tag{2.1}$$

describing the contributions from the magnetic subsystem, excitonic subsystem, and the interaction between them. The magnetic structure of the $CrI_3$ monolayer is described within the model of classical spin vectors localized on sites of the honeycomb

lattice of the Cr atoms. The corresponding energy is given by:

$$H_{\mathrm{m}} = -J \sum_{<i,j>} \boldsymbol{m}_i \cdot \boldsymbol{m}_j - D \sum_{<i,j>} \boldsymbol{d}_{ij} \cdot [\boldsymbol{m}_i \times \boldsymbol{m}_j] - K \sum_i (\boldsymbol{m}_i \cdot \boldsymbol{e}_z)^2 - \mu \sum_i \boldsymbol{B} \cdot \boldsymbol{m}_i. \quad (2.2)$$

Here, the first, second, third, and fourth terms describe the Heisenberg exchange, the Dzyaloshinskii–Moriya interaction (DMI), the uniaxial magnetocrystalline anisotropy and the Zeeman interaction, respectively; $\boldsymbol{m}_i$ is the unit vector pointing along the $i^{th}$ magnetic moment, whose magnitude is $\mu$ for each lattice site; $\boldsymbol{B}$ is the external magnetic field, and $\boldsymbol{d}_{ij} = \boldsymbol{r}_{ij} \times \boldsymbol{e}_z / |\boldsymbol{r}_{ij}|$ is the DMI unit vector with $\boldsymbol{e}_z$ and $\boldsymbol{r}_{ij}$ being the unit vector along the monolayer normal and the vector pointing from site $i$ to site $j$, respectively. These were further explained in section 1.1 with more details.

The angular brackets indicate summation over unique nearest neighbors only. The effective parameter values are taken from Ref. [57]: $J = 2.53$ meV, $D = 1.2$ meV, $K = 0.153$ meV, and $\mu = 3.0\,\mu_B$. The external magnetic field is in the monolayer plane, with the magnitude ranging from 0 T to 3.5 T. In our calculations, we use the computational domain of $N_{\mathrm{c}} = 30 \times 30 = 900$ unit cells equipped with periodic boundary conditions. Note that the number of magnetic moments $N_{\mathrm{a}}$ explicitly included in the calculations is twice as large as $N_c$ ($N_{\mathrm{a}} = 2N_c$ ).

The Hamiltonian describing the excitonic subsystem reads:

$$H_{\mathrm{exc}} = \sum_{\mathbf{q}n} E_{n\mathbf{q}} \hat{X}^{\dagger}_{n\mathbf{q}} \hat{X}_{n\mathbf{q}} + \boldsymbol{E}_{\pm} \sum_n \boldsymbol{D}_{n\mathbf{q}=0} \hat{X}^{\dagger}_{0\mathbf{q}=0} \hat{X}_{n\mathbf{k}=0} + h.c. \quad (2.3)$$

Here, $\hat{X}^{\dagger}_{n\mathbf{q}}$ ($\hat{X}_{n\mathbf{q}}$) are the exciton creation (annihilation) operators characterized by momentum $\boldsymbol{q}$ and band index $n$. $E_{n\mathbf{q}}$ is the exciton energy as well as $\boldsymbol{D}_{n\mathbf{q}=0}$ is the dipole moment of the optical transition obtained from the DFT calculations which here limited to the direct-gap transitions. Using the following equation, we calculate the dipole matrix elements:

$$\boldsymbol{D}_{n\mathbf{q}=0} = \langle 0|\boldsymbol{r}|n\mathbf{q}=0\rangle = \sum_{cv\mathbf{k}} A^{n\mathbf{q}=0}_{cv\mathbf{k}} \langle v\mathbf{k}|\boldsymbol{r}|c\mathbf{k}\rangle, \quad (2.4)$$

where $\langle v\mathbf{k}|\boldsymbol{r}|c\mathbf{k}\rangle$ is the single-particle dipole matrix element corresponding to the optical transition from the conduction band $c$ to the valence band $v$ with momentum $\mathbf{k}$. As well as $A^{n\mathbf{q}}_{cv\mathbf{q}}$ is the $n$th exciton wave function with momentum $\mathbf{q}$. For more details you can see Appendix 6.3.1.

$\boldsymbol{E}_{\pm}(t)$, In the second term of the excitonic Hamiltonian, it is described as follows:

$$\boldsymbol{E}_{\pm}(t) = \mathrm{Re}\left[(E_0, \mp \mathrm{i}E_0, 0) exp(-\mathrm{i}\omega t)\right] h(t) \quad (2.5)$$

Which is correspond to the right- or left-circularly polarized electric field characterized by the pulse envelope $h(t)$. You can find a detailed description of the pulse envelope

in the results and discussion section. The effects of both radiative and non-radiative damping are described phenomenologically, see Appendix 6.3.2 for details.

The interaction between the excitonic and magnetic subsystems is characterized by the following Hamiltonian:

$$H_{\mathrm{s}} = -g\mu \sum_{\mathbf{q}\mathbf{q}'nn'} \left( \boldsymbol{m}_{\mathbf{q}-\mathbf{q}'} - \boldsymbol{m}^{\mathrm{g}}_{\mathbf{q}-\mathbf{q}'} \right) \boldsymbol{M}^{\mathbf{q}\mathbf{q}'}_{nn'} \hat{X}^{\dagger}_{n\mathbf{q}} \hat{X}_{n'\mathbf{q}'} \tag{2.6}$$

where the term inside the parentheses is the Fourier transform of the magnetization relative to the collinear ground state. In order to calculate the Fourier transform of the magnetization, we use the formula below:

$$\boldsymbol{m}_{\mathbf{q}-\mathbf{q}'} = \frac{1}{N_c} \sum_{i}^{N_{\mathrm{c}}} \exp\left[-2\pi \mathrm{i} (\boldsymbol{r}_i \left(\mathbf{q}-\mathbf{q}'\right))_{N_c}\right] \times (\boldsymbol{m}_{2i} + \boldsymbol{m}_{2i-1}) \tag{2.7}$$

Here, $N_{\mathrm{c}} = 30 \times 30 = 900$ is the number of unit cells. The appendix 6.3.3 contains more details. In the equation 2.6. $\boldsymbol{M}^{\mathbf{q}\mathbf{q}'}_{nn'}$ is the dipole matrix element describing the interaction with local magnetic moment, $g$ is the on-site spin-exciton coupling constant.

The total exciton magnetic moment is obtained by computing a sum of the spin and orbital components as following:

$$\boldsymbol{M}^{\mathbf{q}\mathbf{q}'}_{nn'} = \boldsymbol{L}^{\mathbf{q}\mathbf{q}'}_{nn'} + \boldsymbol{S}^{\mathbf{q}\mathbf{q}'}_{nn'} \tag{2.8}$$

Where:

$$\boldsymbol{L}^{\mathbf{q}\mathbf{q}'}_{nn'} = \sum_{cv\mathbf{k},c'v'\mathbf{k}'} \left(A^{n\mathbf{q}}_{cv\mathbf{k}}\right)^* A^{n'\mathbf{q}'}_{c'v'\mathbf{k}'} \times \left[\langle c\mathbf{k}+\mathbf{q}|\boldsymbol{L}|c'\mathbf{k}'+\mathbf{q}'\rangle - \langle v'\mathbf{k}'|\boldsymbol{L}|v\mathbf{k}\rangle\right]$$

As well as,

$$\boldsymbol{S}^{\mathbf{q}\mathbf{q}'}_{nn'} = \sum_{cv\mathbf{k},c'v'\mathbf{k}'} \left(A^{n\mathbf{q}}_{cv\mathbf{k}}\right)^* A^{n'\mathbf{q}'}_{c'v'\mathbf{k}'} \times \left[\langle c\mathbf{k}+\mathbf{q}|\boldsymbol{S}|c'\mathbf{k}'+\mathbf{q}'\rangle - \langle v'\mathbf{k}'|\boldsymbol{S}|v\mathbf{k}\rangle\right]$$

Where $\langle c\mathbf{k}|\boldsymbol{S}|c'\mathbf{k}'\rangle$ is the single-particle spin matrix element between $c$ band with $\mathbf{k}$ momentum and $c'$ band with $\mathbf{k}'$ momentum. In addition, $\langle c\mathbf{k}|\boldsymbol{L}|c'\mathbf{k}'\rangle$ is the matrix elements of the orbital momentum. Please see Appendix 6.3.1 for more details. The evaluation of the coupling constant $g$ can not be performed using standard DFT approaches and requires a separate consideration which goes beyond the scope of the present work. Here, $g$ is taken as a phenomenological parameter with the value $g = 2.3$ meV, which is slightly less then the exchange interaction parameter in the magnetic lattice Hamiltonian.

Note that exciton-exciton interaction is neglected and only single exciton wavefunction $\Psi_{\mathrm{exc}}$ is considered explicitly. Therefore:

$$H_{\mathrm{s}} \approx n_{\mathrm{exc}} \langle \Psi_{\mathrm{exc}}|H_{\mathrm{s}}|\Psi_{\mathrm{exc}}\rangle = -g\mu \sum_{i} \boldsymbol{\sigma}_i (\boldsymbol{m}_i - \boldsymbol{m}^{\mathrm{g}}_i) \tag{2.9}$$

Here, $n_{\text{exc}}$ is the scaling factor proportional to the number of the unit cells (in our case $n_{\text{exc}} = 450$), $\boldsymbol{m}^{\text{g}} \equiv \boldsymbol{e}_z$ is the unit vector along the ground-state magnetization, $\boldsymbol{\sigma}_i$ is the exciton spin vector associated with the $i^{th}$ unit cell. It is better to note that excitons in $CrI_3$ are of the Frenkel type which defined via the following equation:

$$\boldsymbol{\sigma}_i = n_{\text{exc}} \sum_{\mathbf{q}\mathbf{q}'} e^{2\pi \mathrm{i}(\boldsymbol{r}_i(\boldsymbol{q}'-\boldsymbol{q}))/N_{\text{c}}} \sum_{nn'} C_n^{\mathbf{q}*} \boldsymbol{M}_{nn'}^{\mathbf{q}\mathbf{q}'} C_{n'}^{\mathbf{q}'} \tag{2.10}$$

where $\boldsymbol{r}_i$ is the position of $i^{th}$ unit cell and $C_n^{\mathbf{q}}$ are the expansion coefficients of $\Psi_{\text{exc}}$:

$$\Psi_{\text{exc}} = \sum_{n\mathbf{q}} C_n^{\mathbf{q}} \hat{X}_{n\mathbf{q}}^{\dagger} |0\rangle \tag{2.11}$$

The dynamic equations for the observables follow from the model Hamiltonian. The evolution of $\Psi_{\text{exc}}$ is accessed via the equation of motion for its coefficients:

$$i\hbar \frac{\partial C_n^{\mathbf{q}}}{\partial t} = \sum_{n'\mathbf{q}'} H_{nn'}^{\mathbf{q}\mathbf{q}'}(t) C_{n'}^{\mathbf{q}'}(t), \tag{2.12}$$

where $H_{nn'}^{\mathbf{q}\mathbf{q}'}$ are the matrix elements of the excitonic Hamiltonian $H = H_{\text{exc}} + H_{\text{s}}$.

On the other hand, the dynamics of the lattice magnetization is obtained via the time integration of the Landau-Lifshitz-Gilbert equation (LLGE) for the normalized magnetization vectors at zero temperature:

$$\frac{d\boldsymbol{m}_i}{dt} = -\gamma \boldsymbol{m}_i \times \boldsymbol{B}_i^{\text{eff}} + \eta \left( \boldsymbol{m}_i \times \frac{d\boldsymbol{m}_i}{dt} \right), \tag{2.13}$$

where $\gamma$ is the gyromagnetic ratio, $\eta$ is the dimensionless damping parameter which in the present study we take $\eta = 0.1$ and $\eta = 0.2$. Here, $\boldsymbol{B}_i^{\text{eff}}$ is the effective magnetic field defined as:

$$\boldsymbol{B}_i^{\text{eff}} = -\frac{1}{\mu} \frac{\partial H}{\partial \boldsymbol{m}_i}. \tag{2.14}$$

Note that only $H_{\text{m}} + H_{\text{s}}$ depends explicitly on $\boldsymbol{m}_i$. The effect of excitons on the magnetization dynamics is treated within the mean-field approach, where the magnetization-exciton interaction energy $H_{\text{s}}$ depends on the exciton spin vector configuration $\boldsymbol{\sigma}$ (see Eq. (2.9)), which needs to be updated every time step using Eqs. (2.12) and (2.10). Given all that has been said above, we can write the following expression:

$$\boldsymbol{B}_i^{\text{eff}} = g\sigma_i - \frac{1}{\mu} \frac{\partial H_m}{\partial \boldsymbol{m}_i}, \tag{2.15}$$

where the last term is the standard lattice contribution. The vector $\sigma_i$, defined in Eq. (2.10), depends on vector of state components $C_n^{\boldsymbol{q}}$ which in turn depend on the pump of the sample (amplitude of the electric field). In order to evolve the system of above mentioned equations, we use the semi-implicit solver by Mentink et al. [58] for the time integration of the LLGE (This is explained in greater detail in the first chapter). We do not include thermal fluctuations in our simulations so as to focus on exciton dynamics as the main driving force of the magnetization switching [49].

## 2.3 Results and discussion

We study the dynamics of the system induced by spatially homogeneous circular polarized laser pulse at normal incidence. The choice of the pulse envelope $h(t)$ is inspired by real setups [41, 59]:

$$h(t) = A\theta(t_f - |2t - t_f|) \exp\left[-B\left(\frac{t - t_f/2}{t_f}\right)^2\right]. \tag{2.16}$$

Here $t_\mathrm{f}$ is the duration of the pulse, and $A = 1.94$ and $B = 32.2$ are dimensionless parameters defining the total pulse fluence $F$:

$$F = \frac{E_0^2 c\varepsilon_0}{2} \int_0^{t_f} h(t)^2 dt = CI_0 t_f, \tag{2.17}$$

where, here:

$$I_0 = E_0^2 c\varepsilon_0 \tag{2.18}$$

$I_0$ is the intensity of the pulse.

and $C$ is the dimensionless constant as following:

$$C = A^2 \mathrm{erf}(\sqrt{B/2})\sqrt{\pi/(2B)} \tag{2.19}$$

In our calculations, the intensity never exceeds the value of 0.1 TW/cm$^2$, which is consistent with experiments [41, 59]. We take the duration of the pulse $t_f = 4$ ps and its frequency $\omega = 1.94$ eV, which is below the direct bandgap. Note that the chosen value of $\omega$ is in the vicinity of one of the $\sigma^-$ peaks in the absorption spectrum.

The initial magnetization direction is prepared by aligning all magnetic vectors along $\boldsymbol{e}_z$ and perturbing them by small random noise to break the symmetry. The simulation of the spatiotemporal magnetization pattern provides information about the evolution of the cumulative out-of-plane magnetization due to the spin lattice and excitons:

$$M_z^m(t) = \frac{1}{N_\mathrm{a}} \sum_{i=1}^{N_\mathrm{a}} m_i^z(t) \tag{2.20}$$

$$M_z^\sigma(t) = \frac{1}{N_\mathrm{c}} \sum_{i=1}^{N_\mathrm{c}} \sigma_i^z(t) \tag{2.21}$$

The dynamics of the magnetization switching is shown in Fig.2.5. The arrival of the pulse with $\sigma^-$ polarization leads to the appearance of the randomly distributed

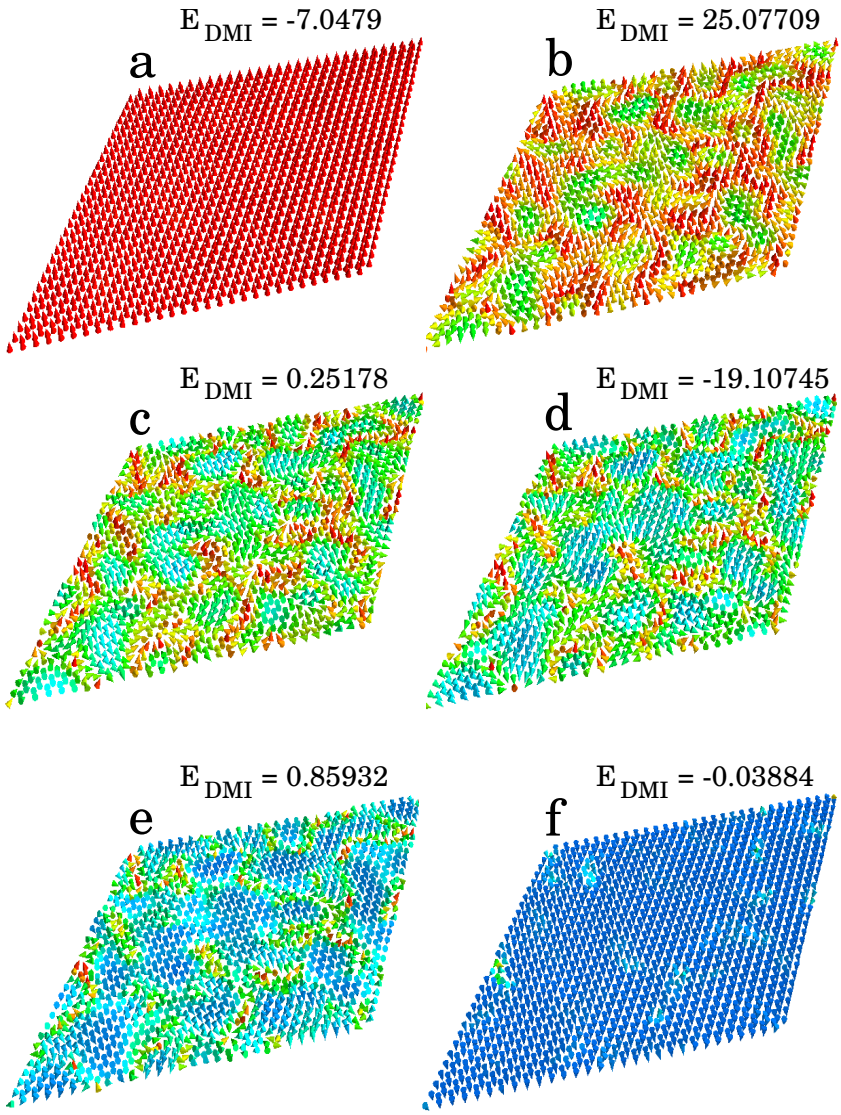


*Figure 2.5:* Evolution of the magnetic structure of the system for the pulse fluence $F_1 = 166$ mJ/cm$^2$. The fluence magnitude is sufficient to induce the magnetization reversal. The snapshots (a)-(f) correspond to 1.6 ps, 1.8 ps, 1.84 ps, 1.86 ps, 1.9 ps, and 2.04 ps, respectively. The color codes the orientation of the magnetic moments of the Cr atoms. This case corresponds to the solid line in Fig. 2.7.

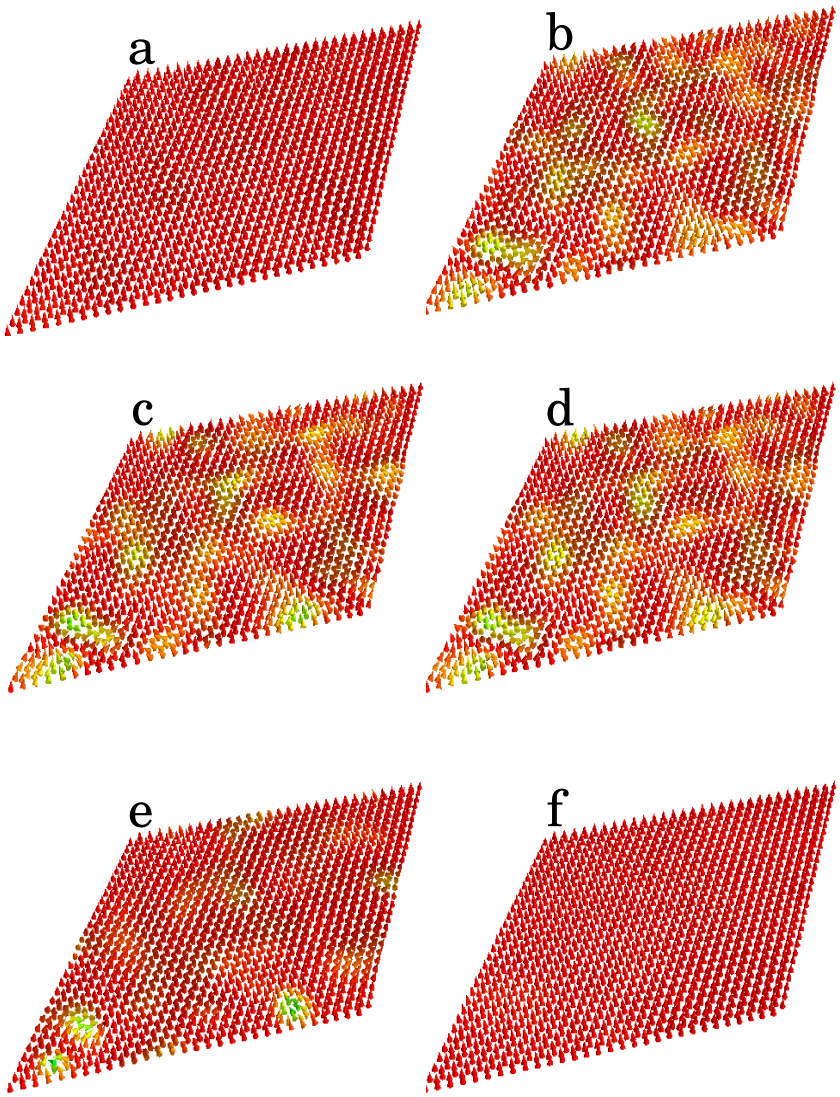


*Figure 2.6:* Evolution of the magnetic structure of the system for the pulse fluence $F_2 = 33$ mJ/cm$^2$. The fluence magnitude is insufficient to induce the magnetization reversal. The snapshots (a)-(f) correspond to 2.2 ps, 2.76 ps, 2.98 ps, 3.2 ps, 4.4 ps, and 8.0 ps, respectively. The color codes the orientation of the magnetic moments of the Cr atoms. This case corresponds to the dashed line in Fig. 2.7.

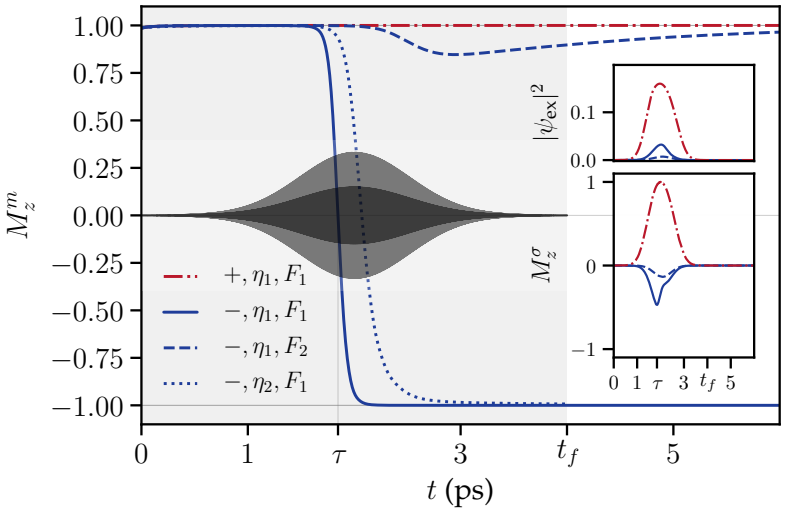


*Figure 2.7:* Time-dependence of the cumulative out-of-plane magnetization $M_z^m$ for different light polarizations. Shaded area indicates the laser pulse duration. Upper right inset shows the time dependence of $|\psi_{ex}|^2 = |\Psi_{\rm exc}|^2 - |\psi_0|^2$ describing the evolution of excited exciton states. Lower right inset shows the time dependence of the exciton magnetization. Dark grey areas show the envelope functions for the optical pump pulse with fluence $F_1 = 166$ mJ/cm$^2$ (lighter grey, magnetization reversal occurs) and $F_2 = 33.2$ mJ/cm$^2$ (darker grey, magnetization reversal does not occur). The switching time $\tau$ is defined by the instant when $M_z^m$ changes sign. Here $\tau = 1.85$ ps. The signs $+$ and $-$ correspond to right-hand and left-hand circularly polarized light, respectively. Here the values of damping constants are $\eta_1 = 0.2$ and $\eta_2 = 0.1$.

domains with inverted magnetization. This process is accompanied by the formation of magnetic vortices favored by the DM interaction. If the fluence exceeds some critical value $F_c$, the size of the domains increases with time, making the system eventually reach the state with spatially homogeneous inverted magnetization which is demonstrates in Fig. 2.5).

Moreover, it is worth noting that in the case of other materials, the switching process may be different, which will be associated with the secondary importance of the DM interaction constant for the all-spin dynamics. On the other hand, if the fluence is below the critical value, the system relaxes back to the homogeneous state without magnetization inversion that can be seen from the insufficiently large number of *islands* that have an inverted value of local magnetization as it is shown in Fig. 2.6.

The dynamics of the cumulative magnetization defined in (2.20) and (2.21) that are shown in Fig. 2.7. The transition between up and down polarized states induced by the pulse is quite abrupt, which makes it possible to introduce the characteristic switching time $\tau$ – the principal parameter that characterizing the magnetization reversal. As

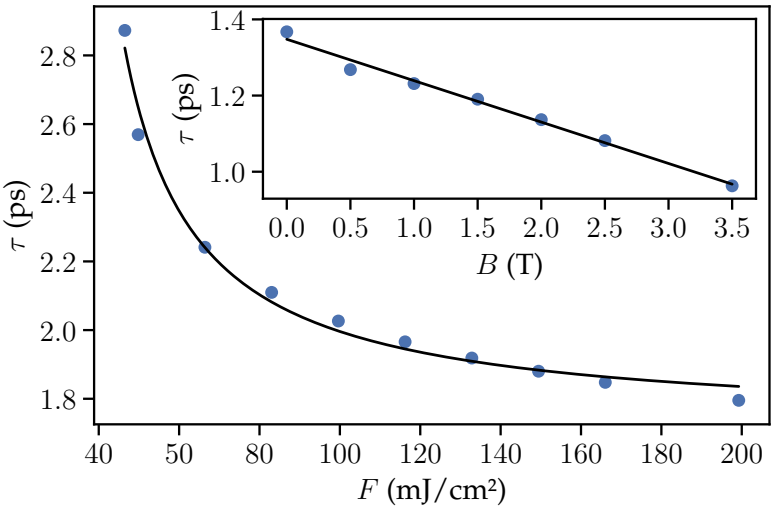


*Figure 2.8:* Magnetization switching time $\tau$ as a function of pump fluence $F$. Magnetization switching is achieved if the fluence of the pulse exceeds a critical value $F_c \approx 46$ mJ/cm$^2$, at which the switching time diverges. The inset shows the switching time as a function of the lateral external magnetic field for the fluence of 133 mJ/cm$^2$.

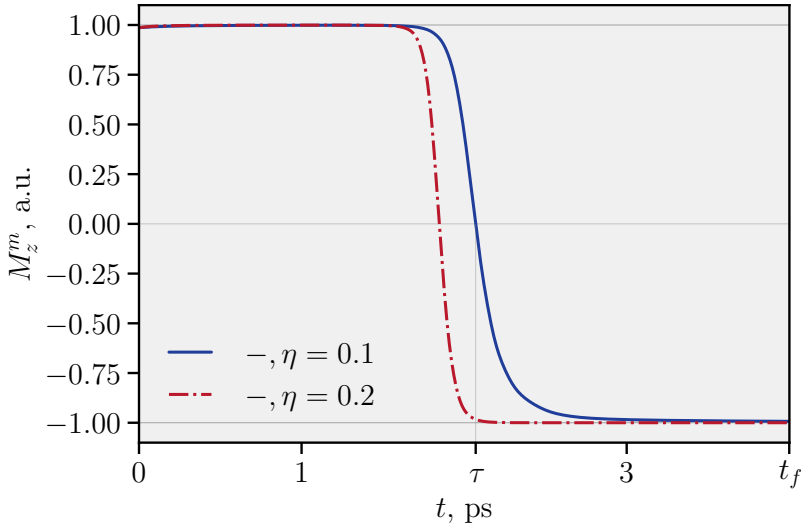


*Figure 2.9:* Magnetization switching time $\tau$ for two different value of $\eta$. For a fixed pulse fluence of $F = 166$ mJ/cm$^2$, A decrease in switching time is associated with an increase in $\eta$ (from 0.1 to 0.2).

expected, $\tau$ decreases with increasing $F$ (see Fig. 2.8).

The switching time becomes infinite when the fluence reaches the critical value $F_c \approx 46$ mJ/cm$^2$, below which no magnetization reversal is possible. This behavior agrees well with our previous study based on the phenomenological model of resonant magnetization switching [49].

If the fluence is less than this value, then switching does not occur at all (dashed line in Fig. 2.7). Here, however, it is worth noting that an important difference from the phenomenological model is the fact that the concept of critical fluence is valid for a pulse of a particular shape and the construction of dependences similar to those on main panel of Fig. 2.8 is valid for an envelope of a certain shape (we only change the field amplitude). It is clear from the model equation that switching will not be achieved if we use extremely small values of the pump intensity, albeit for huge times, this will be prevented by damping and the existing anisotropy.

Noteworthy here is the behavior of the density of excited states of excitons $|\psi_{\text{ex}}|^2$. As expected, the local magnetization affects the excitation of excitons. At the same intensity, more excitons will be excited, whose effective spin coincides with the current value of the local magnetization. This feature is clearly demonstrated in Fig. 2.7 in the upper inset.

Interestingly, the switching time is influenced by lateral magnetic field (see inset in Fig. 2.8). Linear interpolation, as it seemed to us, would be the most appropriate here, although we cannot but note that in the previous work we obtained a dependence that is fitted by a shifted hyperbola. Among other things, we analyzed the dependence of the switching time on the damping value for several specific values of fluence.

Additionally, the critical fluence and the switching time are affected by the exciton decay rate $\lambda$ and the damping parameter $\eta$. For example, for a fixed pulse fluence of $F = 166$ mJ/cm$^2$ , the switching time increases from 1.85 to 2.07 ps when the damping factor $\eta$ decreases from 0.2 to 0.1, see Fig. 2.7 and Fig. 2.9.

As discussed above, decreases in $\eta$ lead to increases in switching times for a fixed fluence value (here $F = 166$ mJ/cm$^2$), As shown in Fig. 2.9. As we can see, in contrast to our previous consideration, a moderate decrease in the damping constant does not lead to a significant increase in the switching time. The change of the circular polarization of the incident beam modifies drastically the magnetization dynamics: the switching does not occur for the initial magnetization pointing up, but can happen for the initial magnetization pointing down.

## 2.4 Conclusion

In conclusion, we developed a microscopic theory of all-optical resonant polarization-sensitive magnetization switching in monolayers of $CrI_3$. The effect is due to the combination of the peculiar optical selection rules for excitons in this material and efficient coupling of excitons to the magnetic lattice. The spatio-temporal distribution of the magnetization under circular polarized pulses was investigated, and the dependence of the parameters characterizing the switching on the properties of the optical pulse was determined.

# 3 All optical control of skyrmion configuration.

The potential for manipulating characteristics of skyrmions in a $CrI_3$ monolayer using circularly polarised light is explored. The effective skyrmion-light interaction is mediated by bright excitons whose magnetization is selectively influenced by the polarization of photons. The light-induced skyrmion dynamics is illustrated by the dependencies of the skyrmion size and the skyrmion lifetime on the intensity and polarization of the incident light pulse. Two-dimensional magnets hosting excitons thus represent a promising platform for the control of topological magnetic structures by light.

## 3.1 Introduction

Magnetic materials play a tremendous role in various applications such as magnetic memory where writing of data is associated with change in magnetization. New technological frontiers, such as terahertz speed and high energy efficiency of magnetization switching, can be reached by use of functional materials whose magnetic properties can be all-optically controlled [61, 62].

Members of the family of 2D magnetic materials known as chromium trihalides ($CrX_3$, where X = I, Br, and Cl), can be considered as prime candidates for this role. Specifically, the optical control of magnetism in monolayers of chromium triiodide ($CrI_3$) was theoretically predicted [49] and experimentally demonstrated [41]. $CrI_3$, an Ising-type ferromagnet, possesses exceptionally high excitonic binding energies and oscillator strengths [44], making this material distinguished among similar systems.

In Ref. [63] the authors developed a microscopic theory of all-optical resonant control of magnetization in excitonic materials and demonstrated reorientation of lattice magnetisation by incident pulses of light with different polarisations and certain values of light parameters. The phenomenon was elucidated through the transfer of spin angular momentum from the electric field to the excitons of a sample, ultimately acting as an effective magnetic field on the lattice magnetisation. However, any analysis of the behaviour of spatially inhomogeneous magnetic structures such as magnetic skyrmions, was not presented and possibility of controlling their properties using excitons remains

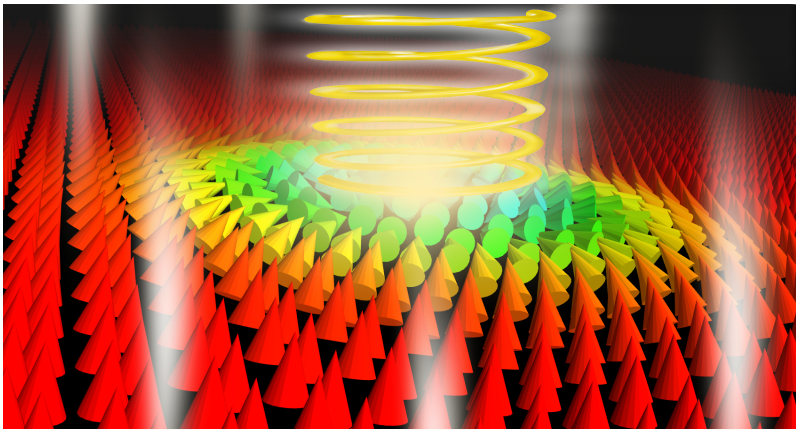

*Figure 3.1:* A sketch of all-optical control of a skyrmion in a $CrI_3$ monolayer. A light pulse with a certain frequency, polarization and time envelope is incident on the monolayer plane whose lattice magnetization is shown with the arrows. The color codes the out-of-plane projection of the magnetization. Under the influence of increasing exciton magnetization, the spins at the boundary of the skyrmion change their direction, effectively leading to either increase or decrease in the skyrmion size.

unexplored. On the other hand, skyrmions themselves are highly appealing for theoretical and experimental studies, owing to their potential utility as units of information storage [64, 65].

The formation of stable skyrmions occurs as a result of the interplay between the magnetic exchange, Dzyaloshinskii–Moriya (DM) interaction, magnetic anisotropy, and the Zeeman interaction [66–71], while the parameters of the skyrmions such as their size and shape can be controlled by changing the interactions strength. However, there remains a gap in the development of the theory for all-optical manipulation of skyrmions.

It has already been demonstrated, that manipulating magnetic spin textures like skyrmion by light beams is experimentally feasible, and both skyrmion motion control and skyrmion reconfiguration can be achieved. [72–75]

The goal of the present study is to explore the phenomenon of all-optical control over the size of magnetic skyrmions in materials hosting bright excitons. The potential for such manipulation is particularly appealing due to the prospect that achieving smaller radius skyrmions could result in more energy-efficient applications [76]. We demonstrate that by applying light pulses of varying circular polarisation and intensity, one can control the radius and profile of magnetic Néel skyrmions in $CrI_3$ ferromagnetic monolayers (see Fig. 3.1 for the schematic representation of the setup).

Additionally, we report light-induced skyrmion collapse, and examine the correspond-

ing skyrmion lifetime as a function of pulse intensity.

The structure of this chapter is as follows. Following the introduction, we describe the formalism utilised in this study, which is based on coupled dynamics of excitons and lattice magnetization of the system. The results and analysis of numerical simulations of the skyrmion dynamics under light pulses of varying intensities and polarizations are presented in section result and discussion. The final section provides concluding remarks.

## 3.2 The model and the equations of motion

Here, we provide a concise overview of the theoretical framework for all-optical resonant control of magnetization in excitonic materials, but comprehensive details of the theory can be found in Ref. [63]. As has been discussed in chapter 2, the total energy of the system is: $H = H_{\mathrm{m}} + H_{\mathrm{exc}} + H_{\mathrm{s}}$.

which comprises contributions from the lattice magnetization, the excitons, and the interaction between these subsystems, respectively. In accordance with section 1.1, in the formalism, the lattice magnetization is modelled as an array of classical vectors localized at the hexagonal lattice sites of chromium atoms. The lattice magnetization is characterized by the equation: 2.2. As well as the excitonic subsystem is described by the equation 2.3. The interaction of the excitons with the lattice magnetization is described by the equation: 2.6.

Note that our analysis excludes exciton-exciton interaction. Therefore, the finite number of excitons in the system is taken into account by introducing the parameter $n_{\mathrm{exc}}$ proportional to the number of unit cells, chosen based on considerations of carrier population density (in our case, $n_{\mathrm{exc}} = 450$). The energy of the interaction between the excitons and the lattice magnetization becomes:

$$H_{\mathrm{s}} \approx n_{\mathrm{exc}} \langle \Psi_{\mathrm{exc}} | \hat{H}_{\mathrm{s}} | \Psi_{\mathrm{exc}} \rangle = -g\mu \sum_i \boldsymbol{\sigma}_i (\boldsymbol{m}_i - \boldsymbol{m}_i^{\mathrm{g}}) \tag{3.1}$$

Here, $\boldsymbol{m}^{\mathrm{g}} \equiv \boldsymbol{e}_z$ is the unit vector along the ground-state magnetization, and the exciton spin vector associated with the $i$th unit cell $\boldsymbol{\sigma}_i$ is defined via the equation 2.10 where $\boldsymbol{r}_i$ is the position of $i^{th}$ unit cell and $C_n^{\mathbf{q}}$ are the expansion coefficients of the exciton wave function $\Psi_{\mathrm{exc}}$:

$$\Psi_{\mathrm{exc}} = \sum_{n\mathbf{q}} C_n^{\mathbf{q}} \hat{X}_{n\mathbf{q}}^{\dagger} |0\rangle \tag{3.2}$$

The exciton dynamics is governed by the equation 2.12. As well as the lattice spin dynamics is described by the Landau–Lifshitz–Gilbert equation (see 2.13). Detailed descriptions of the model Hamiltonian can be found in the second chapter: 2.2.

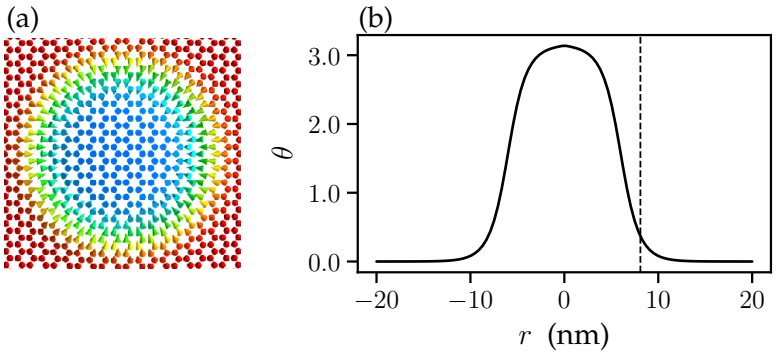


*Figure 3.2:* Equilibrium distribution of the magnetization (a) and corresponding magnetization profile (b) for an isolated skyrmion in the $CrI_3$ monolayer at $B = 0.37$ T in the absence of the light pulse. In (a), the color codes the out-of-plane projection of the magnetization. In (b), the dashed vertical line marks the skyrmion radius calculated according to Eq. (3.3).

In this work, we focus on light-driven dynamics of a single isolated skyrmion in the $CrI_3$ monolayer (see Fig. 3.2). Specifically, we study the time evolution of the skyrmion radius, here defined according to Bogdanov and Hubert [67]:

$$R = r_0 - \theta(r_0)\left(\frac{d\theta}{dr}\right)^{-1}_{r_0} \tag{3.3}$$

where $\theta(r)$ is the polar angle of the lattice magnetization as a function of the distance to the skyrmion centre and $r_0$ is the steepest slope point.

The system is initially prepared at the energy-minimum state corresponding to a single isolated skyrmion whose size can be controlled by adjusting the magnitude of the external magnetic field [67]. At $t = 0$, the dynamics of the system is induced by application of the spatially uniform laser pulse characterized by the time envelope $h(t) = \alpha_1\theta(t_f - |2t - t_f|)\exp\left[-\alpha_2\left((t - t_f/2)/t_f\right)^2\right]$ with $t_\mathrm{f}$ being the pulse duration. Dimensionless parameters $\alpha_1 = 1.94$ and $\alpha_2 = 30.2$ influence both the shape of the pulse profile and the total pulse fluence $F = E_0^2 c\varepsilon_0 \int_0^{t_f} h(t)^2 dt/2$. In our calculations, the duration of the pulse $t_f$ is chosen to be 4 ps and its central frequency $\omega$ is 1.94 eV, which lies below the direct bandgap.

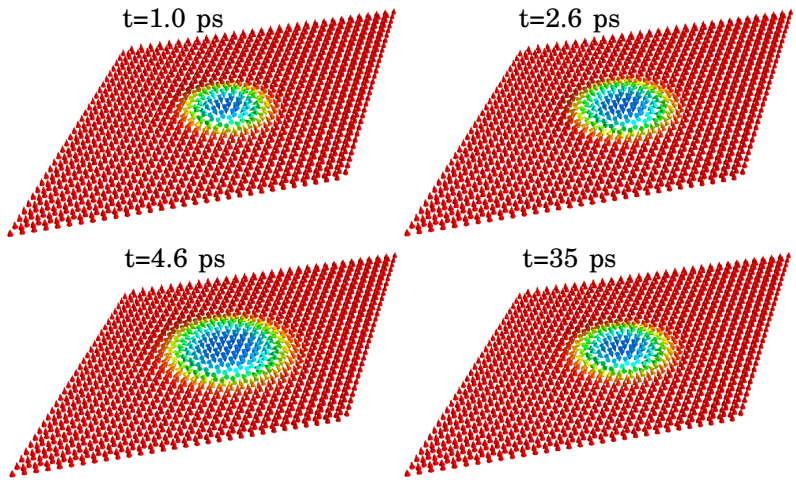


*Figure 3.3:* Snapshots of calculated skyrmion dynamics induced by the light pulse with left-handed polarization and fluence $F = 1.03$ mJ/cm$^2$. The labels indicate corresponding instants of time. The color codes the out-of-plane projection of the lattice magnetization. The equilibrium size of the skyrmion, 4.92 nm, is achieved in the external magnetic field of 0.78 T.

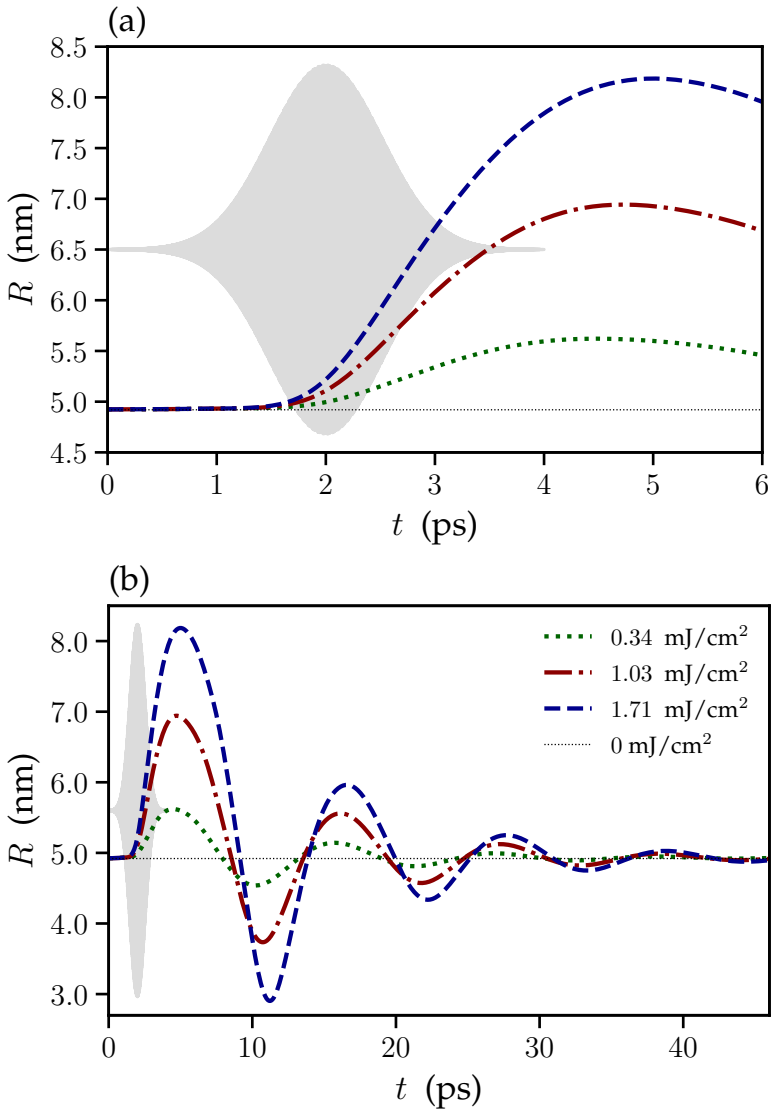


*Figure 3.4:* Calculated skyrmion radius as a function of time for several values of the fluence of the applied left-circularly polarized light pulse, as indicated in the legend. The equilibrium size of the skyrmion, 4.92 nm, corresponding to the external magnetic field of 0.78 T is indicated with the dotted horizontal line. Panel (a) corresponds to the beginning of the dynamical process, while panel (b) shows the evolution of the skyrmion radius in a broader range of time. The gray-shaded area shows the time-envelope of the applied light pulse.

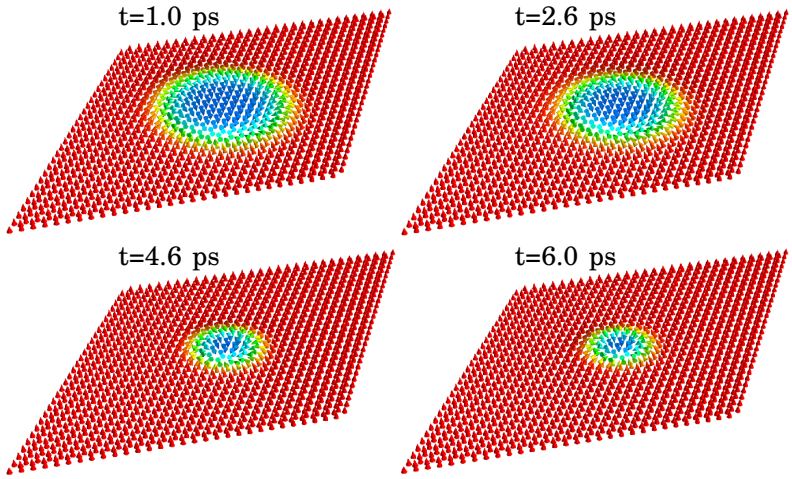


*Figure 3.5:* Snapshots of calculated skyrmion dynamics induced by the light pulse with right-handed polarization and fluence $F = 0.34$ mJ/cm$^2$. The labels indicate corresponding instants of time. The color codes the out-of-plane projection of the lattice magnetization. The equilibrium size of the skyrmion, 8.1 nm, is achieved in the external magnetic field of 0.37 T.

## 3.3 Results and discussion

Figure 3.3 shows snapshots of the calculated skyrmion configuration at several instants of time during and after the application of the left-circularly polarized light pulse with the fluence $F = 1.03$ mJ/cm$^2$. The light polarization ensures that the magnetization of the induced excitons is along the skyrmion core, which results in the skyrmion growth during the application of the light pulse. As exciton scattering is present in the system, the excitonic magnetization wanes after the application of the pulse, resulting in that the skyrmion relaxes to its equilibrium size of 4.92 nm corresponding to the static magnetic field of 0.78 T.

Figure 3.4 shows the time dependence of the skyrmion radius $R$ corresponding to several values of the fluence of the left-circularly polarized light. As expected, larger fluence results in a faster growth and larger maximum size of the skyrmion. After the application of the pulse, the dynamics is not immediately frozen. Instead, the skyrmion radius demonstrates damped oscillations, eventually converging on the equilibrium value.

Controlled shrinking of the skyrmion is demonstrated in Fig. 3.5 showing the snapshots of the magnetization dynamics induced by the right-circularly polarized light pulse with the fluence $F = 0.34$ mJ/cm$^2$. The equilibrium skyrmion radius, $R = 8.1$ nm, is achieved by application of a static magnetic field of $B = 0.37$ T. In contrast to the case of left-circular polarization, the pulse with the right-circular polarization induces excitons with the magnetization opposite to the skyrmion core.

As a result, the skyrmion size decreases. The details of this process can be seen in Fig. 3.6 showing the time-dependencies of the skyrmion radius for several values of the pulse fluence. The changes in the skyrmion size are more pronounced for larger fluence values.

Interestingly, the skyrmion shape is also affected by the light pulse, which manifests itself in a slight increase in the skyrmion size at the beginning of the dynamical process. Similar to the case of the opposite polarization, termination of the pulse is followed by damped oscillations of the skyrmion radius around the equilibrium value with eventual relaxation to the original configuration. Such dynamics suggests that to maintain the skyrmion radius near any predetermined value one should construct a specific protocol for a series of the pulses allowing to balance the effects of the skyrmion relaxation.

The possibility to control the skyrmion size signifies that the skyrmion can also be destroyed by a light pulse with large enough fluence exceeding some critical value. To analyze the skyrmion collapse in this regime, we apply the right-circularly polarized light of various fluences to the skyrmion with the equilibrium radius of 8.1 nm. In our calculations, we define the skyrmion collaspe as a moment when the skyrmion size has dropped by a factor of 10 compared to its equilibrium level, and refer to the

corresponding time as the skyrmion lifetime $\tau$.

The calculated skyrmion lifetime as a function of the flueince of the right-circularly polarized light pulse is shown in Fig. 3.7. Gray area below $F_0$ corresponds to the fluence values below the critical one, for which a skyrmion is not destroyed by a pulse (as its intensity is not enough to achieve the magnetiaztion reversal at skyrmion periphery), but rather relaxes to its original configuration after a pulse leaves, so that the skyrmion lifetime becomes infinite. We checked that this kind of dynamics is universal for a wide range of the parameters of the system (dipole matrix elements, coupling between the spins etc), which affect the details of the evolution only.

In particular, to reorient the magnetization of the sample, and thus destroy a skyrmion, in a sample with larger value of the exchange interaction constant J (see Eq. 2.2), a larger value of fluence is necessary. As anisotropy constant $K$ in this case plays the role of an energy barrier separating two equilibrium spin configurations, its increase rises the values of the critical fluence as well. On the other hand, the increase of the excitonic coupling to light characterized by corresponding optical dipole matrix elements $\boldsymbol{D}_{n\mathbf{q}=0}$ (see Eq.2.3) and exciton-skyrmion coupling described by parameters $\boldsymbol{m}_{\mathbf{q}-\mathbf{q}'}$ (see Eq.2.6) naturally decrease critical fluences.

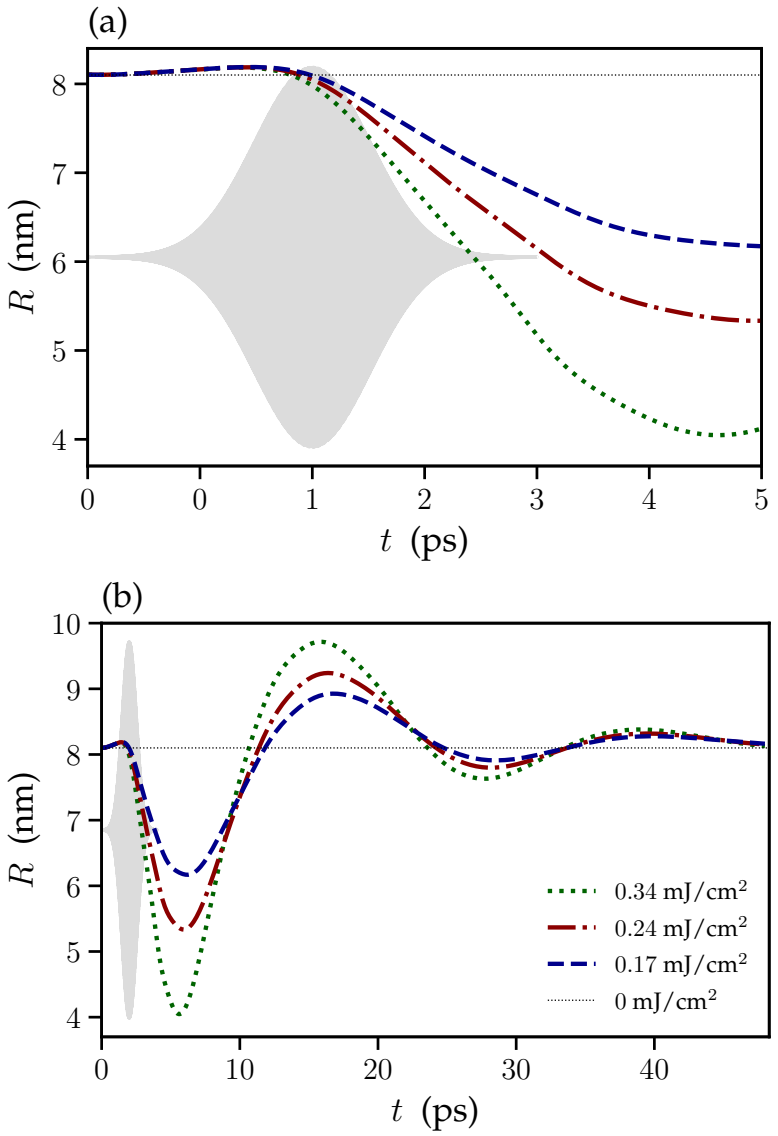


*Figure 3.6:* Calculated skyrmion radius as a function of time for several values of the fluence of the applied right-circularly polarized light pulse, as indicated in the legend. The equilibrium size of the skyrmion, 8.1 nm, corresponding to the external magnetic field of 0.37 T is indicated with the dotted horizontal line. Panel (a) corresponds to the beginning of the dynamical process, while panel (b) shows the evolution of the skyrmion radius in a broader range of time. The gray-shaded area shows the time-envelope of the applied light pulse.

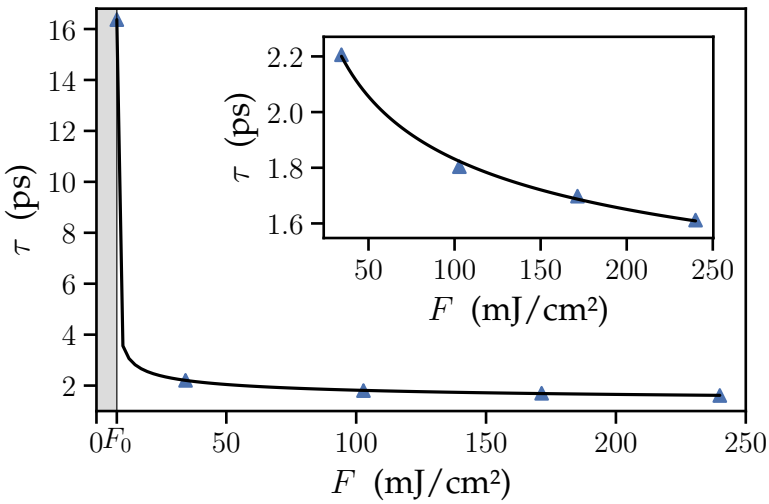


*Figure 3.7:* Calculated skyrmion lifetime as a function of the fluence of the incident light pulse with right-circular polarization. The equilibrium skyrmion radius, 8.1 nm, corresponds to a static magnetic field of 0.37 T. The gray-shaded area marks the fluence magnitudes below the critical value $F_0 = 7.84$ mJ/cm$^2$ for which the skyrmion collapse is not possible.

## 3.4 Conclusion

We demonstrated the possibility to control the characteristic parameters of a skyrmion in monolayers of chromium triiodide, by specific laser pulses. By employing the formalism which couples together the dynamics of atomistic spins and excitons, we investigated, how the parameters of the pulses, in particular their polarization and intensity, affect skyrmion radia and lifetimes. The discovered effects can have potential applications in the domains of spintronics and nanophotonics, allowing, in particular, to reach ultrafast procession rates in future information storage devices based on magnetic monolayers, where skyrmions can be considered as elementary information units. Perspectives in this direction are related to search for other classes of 2D materials, which combine the ambiental stability with robust optical excitonic response and high-temperature magnetic ordering.

# 4 Interaction of exciton with magnetic skyrmion: Localization and anomalous Hall effect

Novel 2D material $CrI_3$ reveals unique combination of 2D ferromagnetism and robust excitonic response. We demonstrate that the possibility of the formation of magnetic topological defects, such as Néel skyrmions, together with large excitonic Zeeman splitting, leads to giant scattering asymmetry, which is the necessary prerequisite for the excitonic anomalous Hall effect. In addition, the diamagnetic effect breaks the inversion symmetry, and in certain cases can result in exciton localization on the skyrmion. This enables the formation of magnetoexcitonic quantum dots with tunable parameters.

## 4.1 Introduction

In low dimensional systems the motion of a particle is restricted to one or two dimensions, which results in certain peculiarities of their physical behavior coming from dramatic enhancement of the role of quantum fluctuations. In particular, we are interested in two-dimensional (2D) systems, as they lie between 3D systems where under certain conditions, Off-Diagonal Long-Range Order (ODLRO) can form at finite temperatures and 1D systems where fluctuations completely destroy long range order and lead to the exponential decay of quantum correlations in real space at any finite temperature. In 2D systems, the situation is more tricky: although long range correlations are destroyed, their decay at low temperature is much slower than in the 1D case.

This is a characteristics of the Berezinskii-Kosterlitz-Thouless phase which is intimately connected with spontaneous creation of topological excitations. Their type depends on the nature of the system in question. In 2D magnets, they are skyrmions [80–82]. For 2D superfluid systems, characteristic for geometries with excitons [83–87] or exciton polaritons [88–90], such defects are vortex-antivortex pairs [91–94].

Systems where several order parameters interact via particle-like entities exhibit particularly interesting, hybrid behavior. In multiferroics, magnetic skyrmions induce

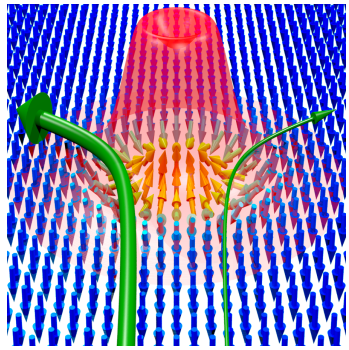

*Figure 4.1:* a) Exciton scattering and localization on a skyrmion in $CrI_3$. The arrows indicate the calculated magnetization at each lattice site, with corresponding winding at the skyrmion area. The pair of green arrows illustrates the exciton scattering paths, with the arrow thickness being proportional to the scattering amplitude. The red dome is the calculated exciton center-of-mass wave function, strongly localized on the skyrmion.

nontrivial dielectric order, which enables a mechanism for an electric-field control of skyrmions [95]. In heterostructures combining chiral magnet and superconductor, co-existing magnetic skyrmions and superconducting vortices create a platform for nucleation and control of Mayorana fermions, a prerequisite for topological quantum computing [96].

Recently, materials combining magnetic properties with robust excitonic response have been discovered [97] such as $CrI_3$. In seeming contradiction to the Mermin-Wagner theorem [106], the finite-temperature long-range magnetic order is enabled in these systems thanks to the magnetic anisotropy [107]. Even more intriguingly, application of electric field or stress breaks the structural inversion symmetry leading to the emergence of uncompensated anti-symmetric exchange between the magnetic atoms [108–110] – the Dzyaloshinskii-Moriya (DM) interaction – that favors noncollinear alignment of magnetic moments. Interplay between magnetic anisotropy, Heisenberg exchange and DM interaction opens a possibility for complex magnetic order in 2D magnets, including the emergence of localized states with nontrivial topology such as skyrmions [111, 112].

The combination of huge optical oscillator strengths with giant Zeeman splitting in $CrI_3$ leads to various magneto-optical phenomena including giant Kerr response [102],

giant magneto band-structure effect [113], magnetic circular dichroism [114], onset of 2D magnetoplasmons [115] and resonant inverse Faraday effect [116]. Moreover, potential emergence of magnetic skyrmions in 2D excitonic materials opens up new exciting physics and interesting applications.

Here, we demonstrate the effects of scattering and localization of excitons on magnetic skyrmions in 2D ferromagnets, as illustrated in Fig. 4.1. We focus on the $CrI_3$ monolayer system, but also study the effect of the parameter variation to demonstrate the relevance of our results to 2D ferromagnets with excitonic response in general.

The scattering on a skyrmion is characterized by strong asymmetry, implying the possibility of anomalous Hall transport of excitons. The first experimental demonstration of exciton anomalous Hall effect was in 2017[117], where the effect originates from the valley-selective helicity of the quantum Berry phase in transition-metal dichalcogenide monolayers, i.e. is of intrinsic type. The exciton Hall effect due to the asymmetric scattering on phonons and impurities was discussed in [118, 119]. The exciton spin Hall effect was intensively studied in the context of strong light-matter coupling [120, 121]. Our proposal thus represents a novel mechanism for exciton amonalous Hall effect. Finally, the possibility to localize excitons leads to the formation of analogs of quantum dots with tunable properties, which can be used as polarization selective single photon emitters.

The band structure of a ferromagnetic single-layered $CrI_3$ is calculated using the density functional theory (DFT) approach implemented in the GPAW [126–128] code with LDA exchange-correlation functional. The lattice constant is taken as $a_0 = 6.69$ Å [122] and the vacuum distance is 16 Å. The discussion went into more detail regarding electronic band structure of $CrI_3$ monolayer in section 1.6. The most straightforward possible estimation of exciton Zeeman splitting is the difference between the energies of the lower conduction band and the fourth conduction band, which correspond to different spin directions, plus the energy difference between the upper conduction band and the second upper conduction band at the crystallographic point G. The resulting value of the Zeeman splitting is equivalent to 0.37 eV.

In this chapter we discuss the result of asymmetry scattering of exciton which is an essential prerequisite for the anomalous Hall effect. Therefore let us first point out the main differences between the anomalous Hall effect and ordinary Hall effect. As it is shown in Fig 4.2. When a non-ferromagnetic materials is exposed to a perpendicular external magnetic field, the Lorentz force acting on the current carriers gives rise to a transverse voltage (Hall voltage) in the plane of the sample, which the Hall voltage depends on the magnetic field. This phenomenon is known as the ordinary Hall effect. But the anomalous Hall effect occurs as a result of spin-orbit coupling and magnetization of ferromagnetic materials, even with weak external magnetic field.

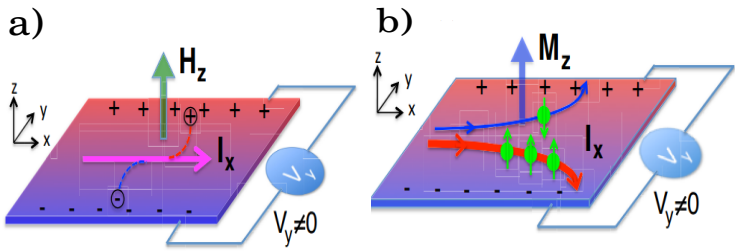


*Figure 4.2:* (a) Ordinary Hall effect. The longitudinal current $I_x$ under vertical external magnetic filed $H_z$ contributes to the transversal voltage $V_y$ due to the Lorentz force experienced by carriers. (b) Anomalous Hall effect. Due to spontaneous magnetization $M_z$ and spin-orbit coupling, which causes unbalanced electron concentration at two transversal sides and leads to finite voltage $V_y$. This figure is from Ref [123]

.

## 4.2 Magnetic Skyrmion in 2D honeycomb lattice in $CrI_3$ monolayer

According to the first chapter, which provides a more detailed explanation of magnetic skyrmion, it is possible to describes magnetic systems as a lattice of classical spins in honeycomb lattices. Within the 2D atomistic model the total energy E of the system includes four terms: Due to the Heisenberg exchange, Dzyaloshinskii–Moriya ($DM$) interaction, magnetic anisotropy and external magnetic field, respectively. Each contribution is characterized by an effective interaction parameter: the exchange interaction energy $J$, the $DM$ interaction parameter D, and the out-of-plane anisotropy parameter $K$. Which is coorespond to equation 2.2.

In calculations we consider the exchange and DM interactions only between the nearest neighbors. In the current work, the computational domain size is chosen to be ($50 \times 50$) lattice sites. Periodic boundary conditions are applied so as to model the extended two dimensional systems. There is an assumption that the system is subject to the external electric field breaking structural inversion symmetry.

The skyrmion profile obtained by fitting the following ansatz data to the simulation data:

$$\theta(\rho, c, w) = 2 \arctan\left(\frac{\cosh(\frac{c}{w/2})}{\sinh(\frac{\rho}{w/2})}\right) \tag{4.1}$$

where $\theta(\rho, c, w)$ is the polar angle of the magnetization at the distance $\rho$ from the skyrmion center and $c$, $w$ are the fit parameters. The normal and the radial components of the unit magnetization vector $\vec{\mathcal{M}}$ are defined as:

$$\mathcal{M}_z = \cos\theta, \quad \mathcal{M}_\rho = \sin\theta \tag{4.2}$$

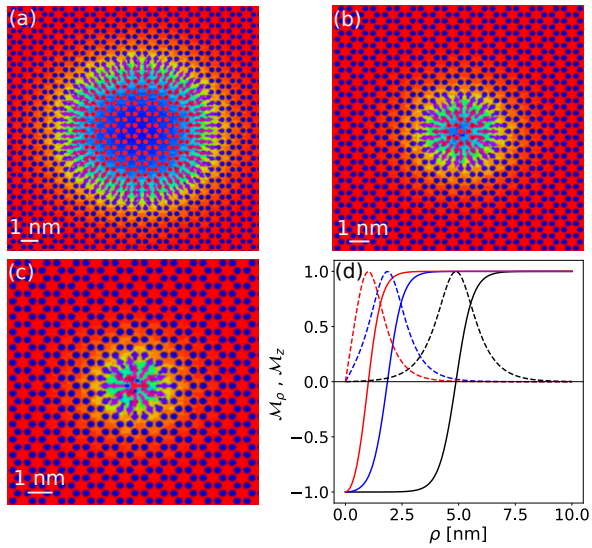


*Figure 4.3:* (a)-(c) Equilibrium magnetic configuration of Néel-type skyrmions in a 2D honeycomb lattice for various values of the magnetic interaction parameters. Color codes the out-of-plane component of magnetization. (a) $D = 0.59$ meV, $K = 0.50$ meV, $J = 1.26$ meV. (b) The same as in (a), but $D = 0.54$ meV. (c) The same as in (a), but $B = 0.8$ T. (d) The radial profiles of the magnetization vector components $\mathcal{M}_z$ (solid curves), and $\mathcal{M}_\rho$ (dashed curves) corresponding to the configurations (a), (b), and (c) shown with black, blue, and red curves, respectively.

Where the radial component is $\mathcal{M}_\rho = \sqrt{\mathcal{M}_x^2 + \mathcal{M}_y^2}$

Here, $\mathcal{M}_x$ and $\mathcal{M}_y$ are magnetization components in $x$ and $y$ direction. (more details in section 1.1):

$$\mathcal{M}_x = \sin\theta\cos\varphi \quad \mathcal{M}_y = \sin\theta\sin\varphi \tag{4.3}$$

The configuration and profile of Neel type skyrmions which is obtained via energy minimization of the system for different values of magnetic field and $DM$ interaction is shown in the Fig 4.3(a)-(d). As shown in this figure, blue and red areas correspond to spin down and spin up, respectively.

Figure 4.3(a) shows the minimum energy of the skyrmion state for $J = 1.26$ meV, $D = 0.59$ meV, $K = 0.50$ meV, and zero magnetic field. Figures 4.3(b) and (c) illustrate that how the skyrmion state changes with the $DM$ interaction and external magnetic field, respectively. The skyrmion profiles corresponding to Figures 4.3(b) and (c) are shown in Fig 4.3(d).

It is important to note that the size of a skyrmion is a fundamental quantity that is sensitive to material parameters such as exchange energy, anisotropy, Dzyaloshinskii-Moriya interaction, and magnetic field. According to Fig 4.4(a) and (b), the skyrmion radius decreases and increases with changing magnetic field and DM interactions, respectively, which is consistent with the general theory of the skyrmion states. In this work we used an alternative definition of the skyrmion center $\vec{R}(x, y)$ that is more relevant to experiments is based on the out-of-plane component of the spin:

$$\vec{R}(x, y) = \frac{\int \vec{r}(\mathcal{M}_z - 1)d^2r}{\int (\mathcal{M}_z - 1)d^2r} \tag{4.4}$$

Moreover the skyrmion radius R, is between the centre of skyrmion in $\mathcal{M}_z = -1$ and $\mathcal{M}_z = 0$ where magnetic moment lie in plane. The non-coplanar magnetic texture of a skyrmion creates an electromagnetic field leading to the asymmetrical scattering and localization of excitons, as explained in what follows.

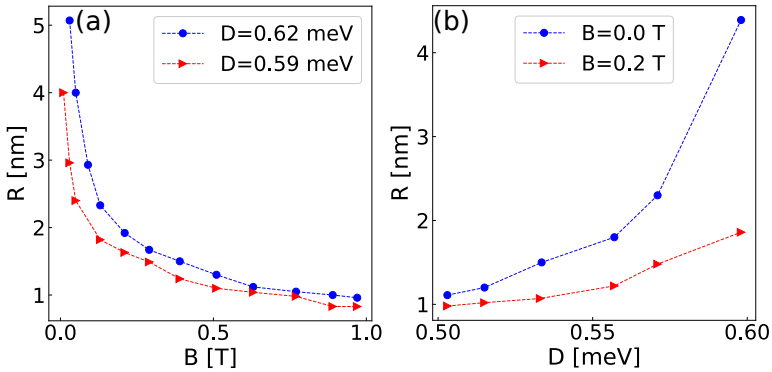


*Figure 4.4:* (a) The skyrmion radius versus the applied magnetic field for different values of the DM interaction parameter, as indicated in the legend. (b) The skyrmion radius versus the DM interaction parameter for different values of the applied magnetic field, as indicated in the legend.

## 4.3 Exciton scattering

Let us take into account the scattering of individual exciton on skyrmion. We consider the center-of-mass dynamics of spinor exciton interacting with the magnetization field due to the skyrmion state. The corresponding Schrödinger equation has the form:

$$\left[-\frac{\hbar^2}{2\mu_X}\nabla^2\mathbf{1}_2+\hat{U}\right]|\Psi\rangle = E_{CM}|\Psi\rangle, \tag{4.5}$$

$$U=\lambda\begin{pmatrix}\mathcal{M}_z & \mathcal{M}_r e^{-i\varphi}\\ \mathcal{M}_r e^{i\varphi} & -\mathcal{M}_z\end{pmatrix} \tag{4.6}$$

where $\mu_X$ is the exciton total mass, $\mathbf{1}_2$ is the $2\times 2$ identity matrix, $\hat{U}=\lambda\vec{\mathcal{M}}\vec{\sigma}$, where $\lambda$ is the interaction energy, and $E_{CM}$ is the exciton center of mass energy. We restrict the treatment with the spin conserving exciton elastic scattering off the skyrmion. The general scattering of massive spinor particle on magnetic skyrmion is discussed in Refs [133, 134]. In order to exclude the spin degree of freedom, we apply the adiabatic elimination approach [135].

We apply the following anzats and expanding the exciton state in the basis $|\Psi\rangle = \psi_1|\chi_1\rangle+\psi_2|\chi_2\rangle$. Here $\chi_{1,2}$ are the eigenstates of skyrmion potential $\hat{U}$, corresponding

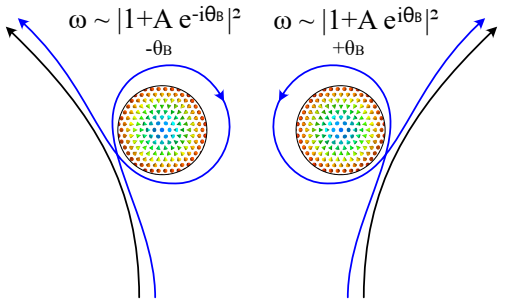


*Figure 4.5:* The schematic representation illustrates a round trip around the skyrmion in clockwise (scattering to the right) and anticlockwise (scattering to the left) directions. $\theta_B$ is geometric phase

to eigenvalues $u_{1,2} = \mp\lambda$. Assuming $\psi_2 = 0$, we project the Schrödinger equation to the state $|\chi_1\rangle$. It is of crucial importance, that in the effective spinless model, synthetic U(1) gauge field appears. It plays the role of an effective magnetic field and is responsible for giant asymmetry of the scattering.

Physically, the presence of a skyrmion means, that the symmetry of the system in z-direction is broken, i.e. the unity vectors $\hat{e}_z$ and $-\hat{e}_z$ are not equivalent. Therefore, if an exciton possesses a finite value of wave vector $\vec{k}$, directions $[\vec{k} \times \hat{e}_z]$ and $-[\vec{k} \times \hat{e}_z]$, corresponding to the scattering to the right and to the left are not equivalent as well. Moreover, non-equivalence of these two directions can be understood if one considers a scattering of an exciton on a skyrmion in adiabatic approximation using the Berry phase argument.

Indeed, consider the contribution of the trajectories with exciton making a round trip around the skyrmion in clockwise (scattering to the right) and anticlockwise (scattering to the left) directions. It is shown in Figure 4.5. The spin of the exciton in this approximation follows the magnetization pattern of the skyrmion, and it can be seen from Figure 4.1 that it will cover a non-zero solid angle, which means that a wavefunction of the exciton will acquire a geometric phase $\theta_B$ whose sign depends on the direction of the circumvention around the skyrmion. Therefore, the trajectories with round trips contribute differently to the total scattering amplitude for scattering angles $\theta$ and $-\theta$ due to the opposite signs of the phase in the interference terms.

So with using the completeness relation $|\chi_1\rangle\langle\chi_1| + |\chi_2\rangle\langle\chi_2| = \mathbf{1}$, and expanding the Schrödinger equation we can reach at:

$$\frac{1}{2\mu_X}\langle\chi_1|\hat{P}(|\chi_1\rangle\langle\chi_1| + |\chi_2\rangle\langle\chi_2|)\hat{P}\psi_1|\chi_1\rangle = (E_{CM} + \lambda)\psi_1. \tag{4.7}$$

and,

$$\frac{1}{2\mu_X}\Big[\langle\chi_1|\hat{P}|\chi_1\rangle(\hat{P}\psi_1)+\hat{P}^2\psi_1+\Big(\langle\chi_1|\hat{P}|\chi_1\rangle\psi_1+\hat{P}\psi_1\Big)\langle\chi_1|\hat{P}|\chi_1\rangle$$
$$+\psi_1\hat{P}\langle\chi_1|\hat{P}|\chi_1\rangle+\langle\chi_1|\hat{P}|\chi_2\rangle\psi_1\langle\chi_2|\hat{P}|\chi_1\rangle\Big]=(E_{\mathrm{CM}}+\lambda)\psi_1 \tag{4.8}$$

We note that $\langle\chi_1|\hat{P}\chi_2\rangle=-\langle\chi_2|\hat{P}\chi_1\rangle$, and introduce the notations

$$\vec{A}=i\frac{\hbar}{e}\langle\chi_1|\nabla\chi_1\rangle, \tag{4.9}$$

$$W=\frac{\hbar^2}{2\mu_X}|\langle\chi_2|\nabla\chi_1\rangle|^2, \tag{4.10}$$

allowing to rewrite the equation for $\psi_1$ in the form

$$\left[\frac{1}{2\mu_X}(\hat{P}-e\vec{A})^2+W-\lambda\right]\psi_1=E_{\mathrm{CM}}\psi_1. \tag{4.11}$$

We proceed with the explicit calculations of the terms involved in eq. (6.25). The eigenvectors read as

$$|\chi_1\rangle=\frac{1}{\sqrt{2(1+\mathcal{M}_z)}}\begin{pmatrix}\mathcal{M}_r\\-(1+\mathcal{M}_z)e^{i\varphi}\end{pmatrix}, \tag{4.12}$$

$$|\chi_2\rangle=\frac{1}{\sqrt{2(1-\mathcal{M}_z)}}\begin{pmatrix}\mathcal{M}_r\\(1-\mathcal{M}_z)e^{i\varphi}\end{pmatrix}. \tag{4.13}$$

The functions $\mathcal{M}_\rho$, $\mathcal{M}_z$ depend only on radial coordinate, so that

$$\vec{A}=-\frac{\hbar}{e}\frac{1+\mathcal{M}_z}{2\rho}\vec{\varphi}, \tag{4.14}$$

$$W=\frac{\hbar^2}{2\mu_X}\left[\frac{(\mathcal{M}_z\mathcal{M}_r'-\mathcal{M}_r\mathcal{M}_z')^2}{4}+\frac{\mathcal{M}_r^2}{4\rho^2}\right], \tag{4.15}$$

are vector and scalar gauge potentials, respectively. Here $e$ denotes the unit charge, $\hat{\varphi}$ is the unit vector in the azimuthal direction, and the prime denotes the derivative with respect to $\rho$. Interestingly, the gauge potentials do not depend on the interaction energy $\lambda$. Consequently, the scattering cross-section in the adiabatic elimination approach is independent of $\lambda$, as it only leads to rigid energy shift in Eq. (6.25).

The presence of the vector potential $\vec{A}$ gives rise to an effective magnetic field $\vec{B}^{\mathrm{eff}}=\nabla\times\vec{A}$. Due to the symmetry of the vector potential, the magnetic field is normal to the plane and reads:

$$B_z^{\mathrm{eff}}=\frac{A_\varphi}{\rho}+\frac{\partial A_\varphi}{\partial\rho}. \tag{4.16}$$

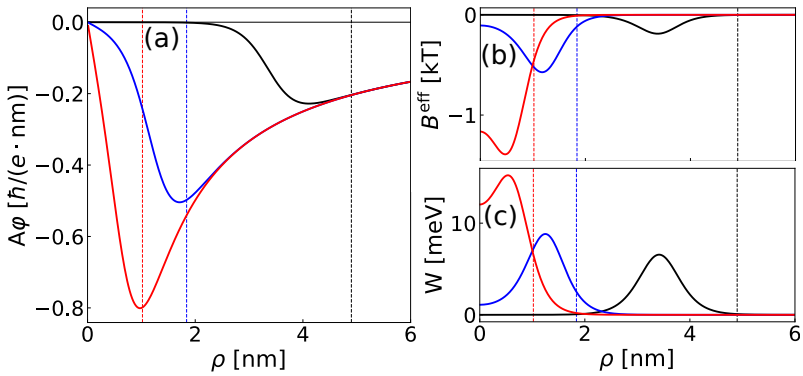


*Figure 4.6:* The radial dependence of (a) the gauge vector potential; (b) effective magnetic field; (c) scalar potential for different profiles of skyrmion corresponding to Fig. 4.3. The vertical lines denote the respective skyrmion radii. The vector potential has only azimuthal component, which scales as $1/\rho$ outside the skyrmion region. The giant values of above 1000 T for the effective magnetic field are due to the nm size of the skyrmion and the rapid variation of vector potential inside. The scalar potential has a radial symmetry, and rapidly decays outside the skyrmion area.

Notably, the maximal absolute value of the vector potential decreases versus the skyrmion size. Conversely, the maxima appears at larger distance from the skyrmion center. Outside the skyrmion region, the vector potential demonstrates a $1/\rho$ scaling.

Figure 4.6 (b) shows the emergent effective magnetic field due to skyrmion. The giant values of the field are explained by the rapid variation of vector potential at sub-nm scale, driven by the nature of the skyrmion magnetization texture. We mention that for a skyrmion having the size of $\sim 16$ nm due to topological winding of the texture an effective magnetic field of $B^{\text{eff}} \approx 13$ T was reported earlier.

The radial dependence of scalar potential is shown in Fig. 4.6 (c), demonstrating a good localization within the skyrmion. Notably, it has a local minima at $\rho = 0$, which can lead to the formation of the excitonic quasibound states and scattering resonances. However, characteristic energies of these resonances correspond to the wave vectors of the excitons lying far outside the light cone, which can not be directly created optically, and are thus not analyzed in this work.

The differential cross-section of elastic scattering reads [133, 136]:

$$\omega(\vec{k},\vec{k}') = \frac{\mu_X^2}{2\pi\hbar^4}\frac{|T(\vec{k},\vec{k}')|^2}{k}. \tag{4.17}$$

Here $\vec{k}$, $\vec{k}'$ correspond to the center of mass wave vectors of incident and scattered excitons, respectively, with $k = |\vec{k}| = |\vec{k}'|$. The scattering $T$-matrix can be expanded as

$$T(\vec{k},\vec{k}') \approx V(\vec{k},\vec{k}') + \sum_{\vec{k}''}\frac{V(\vec{k}',\vec{k}'')V(\vec{k}'',\vec{k})}{\epsilon_k - \epsilon_{k''} + i\eta}, \tag{4.18}$$

where $\epsilon_k = \hbar^2k^2/(2\mu_X)$. The matrix element $V(\vec{k},\vec{k}')$ within the first Born approximation has the form (see the appendix B for the derivation):

$$\begin{aligned} V(\vec{k}',\vec{k}) = {} & \frac{1}{2\pi}\int_0^\infty J_0(|\Delta\vec{k}|\rho)\left(\frac{e^2\vec{A}^2}{2\mu_X} + W\right)\rho\mathrm{d}\rho \\ & - \frac{i}{\pi}\frac{e\hbar}{2\mu_X}\frac{[\vec{k}'\times\vec{k}]_z}{|\Delta\vec{k}|}\int_0^\infty J_1(|\Delta\vec{k}|\rho)A(\rho)\rho\mathrm{d}\rho, \end{aligned} \tag{4.19}$$

where $\Delta\vec{k} = \vec{k}' - \vec{k}$. Thus, the differential cross-section can be expanded up to third order in skyrmion potential strength [137]:

$$\omega(\vec{k},\vec{k}') \approx \omega^{(2)}(\vec{k},\vec{k}') + \omega_s^{(3)}(\vec{k},\vec{k}') + \omega_a^{(3)}(\vec{k},\vec{k}'), \tag{4.20}$$

where the lowest order term

$$\omega^{(2)}(\vec{k},\vec{k}') = \frac{\mu_X^2}{2\pi\hbar^4}\frac{|V(\vec{k},\vec{k}')|^2}{k} \tag{4.21}$$

is symmetric. The third order terms read:

$$\omega_s^{(3)}(\vec{k},\vec{k}') = \frac{\mu_X^2}{2\pi\hbar^4 k}2\mathcal{P}\left\{\mathrm{Re}\left[V(\vec{k},\vec{k}')\sum_{\vec{k}''}\frac{V(\vec{k}',\vec{k}'')V(\vec{k}'',\vec{k})}{\epsilon_k - \epsilon_{k''}}\right]\right\}, \tag{4.22}$$

$$\omega_a^{(3)}(\vec{k},\vec{k}') = -\frac{\mu_X^2}{\hbar^4 k}\mathrm{Im}\left[V(\vec{k},\vec{k}')\sum_{\vec{k}''}V(\vec{k}',\vec{k}'')V(\vec{k}'',\vec{k})\delta(\epsilon_k-\epsilon_{k''})\right], \tag{4.23}$$

where $\mathcal{P}$ denotes the principal value integration. The details of evaluation of Eq. (4.23) are presented in appendix. where the lowest order term $\omega^{(2)}(\vec{k},\vec{k}')$ is symmetric. The third order term contains an irrelevant symmetric correction $\omega_s^{(3)}(\vec{k},\vec{k}')$ and an asymmetric contribution $\omega_a^{(3)}(\vec{k},\vec{k}')$ .

The cross-section of exciton scattering is presented in Fig. 4.7. The exciton wave vector has upper limit defined by optical excitation range $k_{\max} = nE_X/(\hbar c)$. Here $n \approx 2$ is the refractive index of surrounding media [122], $c$ is the speed of light. Together with excitonic resonance $E_X = 1.65$ eV, this yields $k_{\max} \approx 16.5\ \mu m^{-1}$, and the exciton total mass is $\mu_X = m_e + |m_h| \approx 5.6m_0$.

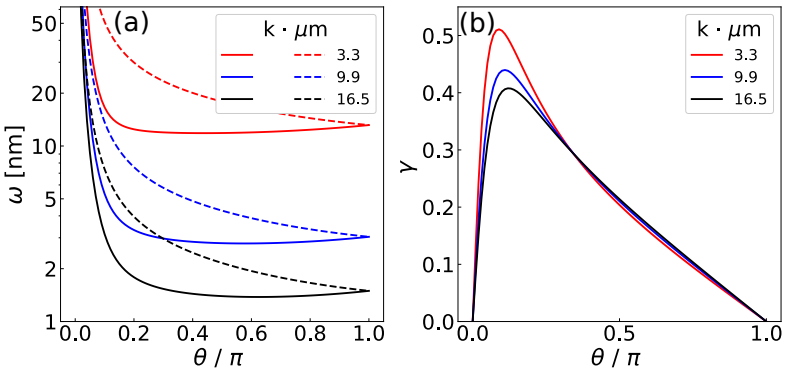


*Figure 4.7:* The cross-section of exciton scattering on skyrmion. (a) The angular dependence of amplitude for several values of the wave vector, as indicated in the legend. The solid and dashed lines correspond to anticlockwise $\omega(\theta)$ and clockwise $\omega(-\theta)$ scattering directions, respectively. The scattering amplitude monotonically decays with wave vector, and varies weakly with the scattering angle, with the rapid divergence at $\theta \to 0$ region. (b) The scattering asymmetry $\gamma = |\omega(k,\theta) - \omega(k,-\theta)|/\left(\omega(k,\theta) + \omega(k,-\theta)\right)$ versus the scattering angle for several values of the wave vector, as indicated in the legend. The giant asymmetry at small scattering angles is accompanied by moderate dependence on the wave vector.

Figure 4.7 (a) illustrates the scattering amplitude versus the scattering angle for several values of the wave vector. At the $\theta \to 0$ limit the scattering cross-section diverges as $\omega^{(2)} \xrightarrow{\theta\to 0} 4/(k\theta^2)$ due to the $A \sim 1/r$ tale of the vector potential, similar to the

scattering off the Coulomb potential [138].

Therefore, the region of divergence depends weakly on the skyrmion and exciton parameters. The universal shape of the scattering cross-section at small angles could be modified only if the skyrmion radius $R \sim 1/k$, which corresponds to the $\mu m$ scale. This is in contrast to rather small skyrmions in the $CrI_3$ system, see Fig. 4.3.

For the characterization of scattering asymmetry we introduce the asymmetry degree

$$\gamma = \frac{|\omega(k,\theta) - \omega(k,-\theta)|}{\omega(k,\theta) + \omega(k,-\theta)} \tag{4.24}$$

This quantity is illustrated in Fig. 4.7 (b). One clearly sees, that scattering is highly asymmetric ($\gamma$ can reach values of 0.5), and the asymmetry rate has a moderate dependence on scattering wave vector. At $\theta = 0$ we get $\gamma = 0$, as expected from the symmetry considerations. On the other hand, the scattering asymmetry increases as scattering trajectories with closed loops around the skyrmion become more prominent in the region where the total cross-section starts growing.

As a result, the asymmetry peaks at intermediate angles, and the position of the peak varies slowly with the exciton wave vector, for more details see Fig. 4.7(b).

The presence of asymmetric scattering results in the anomalous Hall effect for excitons, which is characterized by the Hall angle defined as the ratio between transverse and longitudinal currents. Assuming the initial excitation of excitons with wave vector $\vec{k}$ directed to the center of skyrmion, one finds the following Hall angle $\alpha$ in the regime of the elastic scattering:

$$|\alpha(k)| \approx \left|\frac{j_\perp}{j_\parallel}\right| = \left|\frac{\int\limits_{-\pi}^{\pi} k \tan\theta \omega(k,\theta) \mathrm{d}\theta}{\int\limits_{-\pi}^{\pi} k\omega(k,\theta)\mathrm{d}\theta}\right| \tag{4.25}$$

The calculated value of the Hall angle is $\alpha \sim 0.025 - 0.035$, in line with previous theoretical [119], and experimental [117] reports. The wave vector dependence of the Hall angle is shown in figure 4.8.

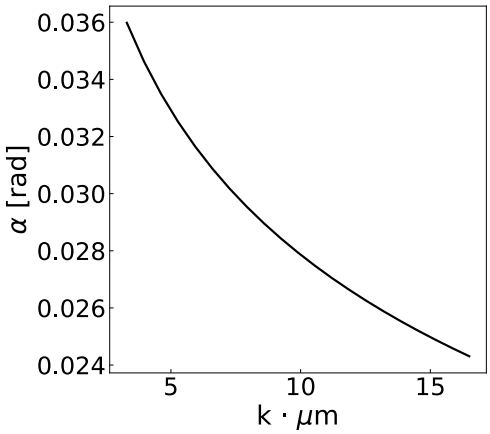


*Figure 4.8:* Hall angle, the ratio between transverse and longitudinal currents as a function of excitons wave vector $\vec{k}$.

## 4.4 Exciton localization

In the regime of large magnetic fields the diamagnetic term has a strong impact on the excitonic spectrum. Given by ferromagnetic nature of considered material, in Eq. (4.5) we account for quadratic terms in magnetic field, which can be phenomenologically included in our model:

$$\hat{H}_{\text{dia}} = \xi \mathcal{M}_z^2 \mathbb{1}_2, \tag{4.26}$$

where $\xi$ is the diamagnetic shift energy, which is taken as a phenomenological parameter. At sufficiently large values of $\xi$ the presence of diamagnetic term can result in exciton localization at skyrmion. We seek for the $s-$state solution in the form $\Psi = (\psi_+, \psi_- e^{i\varphi})$. The radial profiles of the components of exciton wave function are plotted in Fig. 4.9 (a). Quite naturally, for smaller skyrmion the area of exciton localization is more compact. Further, with the enhancement of diamagnetic term the binding energy increases, as shown in Fig. 4.9 (b). For the skyrmion of smaller radius the localized state appears at larger values of diamagnetic shift. Figure 4.9 (c) illustrates the effective radius of localization $l = \langle \Psi | \rho | \Psi \rangle$. The saturation of localization radius at elevated values of diamagnetic shift is explained by the repulsion of exciton wave function components towards the skyrmion edge, c.f. the black curves in Fig. 4.9 (a) and the inset therein.

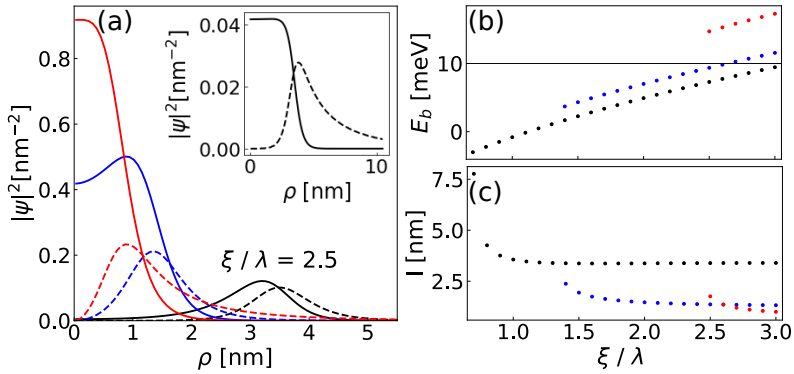


*Figure 4.9:* (a) The center-of-mass wave function of exciton localized on skyrmion. The colors correspond to different profiles of skyrmion shown in Fig. 4.3. The solid and dashed curves correspond to spin-up and spin-down components of the wave function. Here the diamagnetic ratio is $\xi/\lambda = 2.5$, and the inset illustrates the case of a large skyrmion, with moderate diamagnetic ratio $\xi/\lambda = 0.7$. (b) The binding energy, and (c) the radius of exciton localization on skyrmion versus the diamagnetic ratio. For smaller skyrmions, the localized states emerge only at very large values of diamagnetic shift. The thin line in panel (b) shows the interaction energy $\lambda$.

## 4.5 Conclusions and discussion

In conclusion, we developed a theory addressing the co-existence of excitons and magnetic skyrmions in a 2D material. Within the theory, the band structure and exciton states are calculated using DFT and the magnetic properties including the properties of skyrmion states are obtained via atomistic spin simulations. We applied the theory to the celebrated $CrI_3$ monolayer system, yet the phenomena we predicted should be relevant for a class of 2D magnetic semiconductors with the possibility of broken structural inversion symmetry necessary for the emergence of uncompensated DM interaction.

We revealed two scenarios of exciton-skyrmion interaction. The first scenario implies a spin-conserving exciton elastic scattering off the skyrmion. Here we apply an adiabatic elimination approach to discard the spin degree of freedom. Similar to the scattering of massive spinor paricle [133], the exciton scattering in spinless domain is characterized by giant asymmetry, provided by emerging synthetic U(1) gauge field.

Such asymmetric scattering is a necessary prerequisite of the excitonic anomalous Hall effect [119].

The second scenario accounts for the impact of diamagnetic effect on the exciton-skyrmion interaction. The diamagnetic term breaks the inversion symmetry, which for sufficiently large values of diamagnetic energy shift leads to an efficient localization of spinful exciton on the skyrmion. This opens a way for creation of tunable analogs of magnetic excitonic quantum dots, which can find their applications in the domain of quantum optics, for example as single photon emitters with tailored properties. Additionally, the exciton localization enables optical detection of skyrmions, which is particularly important for antiferromagnetic systems.

We indeed foresee interesting phenomena resulting from the interaction of excitons with topological magnetic textures in antiferromagnets. For example, based on the analogy with the electron transport [139–142], we conjecture that skyrmions on two antiferromagnetically coupled sublattices deflect equal amount of excitons with opposite spins to opposite directions, leading to zero net exciton Hall transport, but finite exciton spin Hall transport. Such spin exciton Hall effect induced by topological magnetic textures as well as other phenomena remain to be explored.

In our work, we focus on excitonic response to the presence of magnetic skyrmions, but the opposite effect is also feasible thus enabling resonant optical control of skyrmions. Generalization of the theory to describe the dynamical response of magnetic skyrmions should be straightforward [116]. This will make it possible to simulate various phenomena associated with coupled exciton-skyrmion dynamics.

# 5 Conclusions and outlook

This thesis presents the development of a theory aimed at studying various phenomena in the regime of co-existence of the skyrmion and bright exciton. We studied a microscopic theory of all-optical control of reorientation of magnetization in $CrI_3$ monolayers. The effect is due to the combination of the peculiar optical selection rules for excitons in this material and efficient coupling of excitons to the magnetic lattice. Our study also demonstrates the potential for manipulating the size of skyrmions in monolayers of chromium triiodide, without the need for an alternating magnetic field, solely through the use of light pulses with specific polarization and intensity. This achievement holds significant implications for modern spintronics. Ultimately, We revealed a scenario of exciton-skyrmion interaction which implies a spin conserving exciton elastic scattering off the skyrmion. Here we apply an adiabatic elimination approach to discard the spin degree of freedom. As a result, this will enable researchers to simulate a variety of phenomena connected to coupled exciton-skyrmion dynamics.

# 6 Appendices

## 6.1 Appendix A

### 6.1.1 Connection between material parameters within atomistic and micromagnetic models

The atomistic and continuous models can be compared to each other through the connection between material parameters $J$, $D$, $K$ and $\mu$ from the atomistic model and $\mathcal{A}$, $\mathcal{D}$, $\mathcal{K}$ and $\mathcal{M}$ from the continuous model.

for instance of the atomistic hamiltonian the exchange term takes the following form:

$$E_{ex} = -j \sum_{ij} (m_i \cdot m_j) \approx -Jm^2 \sum_{ij} cos\theta_{ij} \tag{6.1}$$

then we can write:

$$cos\theta ij = -1 + \frac{1}{2}\theta^2 ij \tag{6.2}$$

In continuous description , the angle between $m_i$ and $m_j$ is small, and with using the Taylor expansion:

$$\theta_{ij} \approx |m_i - m_j| \approx |(r_{ij} \cdot \nabla) m_i| \tag{6.3}$$

where vector $r_{ij}$ connects site $i$ and $j$. In case of honeycomb lattice each as we consider in this project,sites $i$ and $j$ have 3 nearest neighbors that given by the following vectors:

$$r_1 = a(1,0,0), r_2 = a(-\frac{1}{2}, \frac{\sqrt{3}}{2}, 0), r_3 = a(-\frac{1}{2}, -\frac{\sqrt{3}}{2}, 0) \tag{6.4}$$

$$r_4 = a(-1,0,0), r_5 = a(\frac{1}{2}, \frac{\sqrt{3}}{2}, 0), r_6 = a(\frac{1}{2}, -\frac{\sqrt{3}}{2}, 0) \tag{6.5}$$

$a$ is lattice constant. With substituting Eq. (6.4) into Eq. (6.3) and then Eq. (6.1), as well as changing the summation to integration, we obtain:

$$E_{ex} = \int dxdydz \frac{\sqrt{3}}{6h} J(\nabla m_x^2 + \nabla m_y^2) \tag{6.6}$$

$$E_{ex} = \mathcal{A}h \int \left[ (\frac{\partial \boldsymbol{m}}{\partial x})^2 + (\frac{\partial \boldsymbol{m}}{\partial y})^2 \right] \tag{6.7}$$

where $h$ is the thickness of the layer, $\boldsymbol{m} = (m_x, m_y, m_z)$ is a unit vector in the direction of local magnetization and integration is performed over the surface of the layer. Conversion formulas relating parameters $\mathcal{A}$, $\mathcal{D}$, $\mathcal{K}$ and $\mathcal{M}$ to their discrete-model counterparts can be derived using a standard approach presented cite aharoni

$$\mathcal{A} = \frac{\sqrt{3}}{6h} J \tag{6.8}$$

With similar way, In the continuum approximation, contributions from (DM) interaction, magnetic anisotropy and external magnetic field to the energy of a thin magnetic layer are given by the following equation:

$$E_{\mathrm{DM}} = \mathcal{D}h \int \left[ m_z \left( \frac{\partial m_x}{\partial x} + \frac{\partial m_y}{\partial y} \right) - \left( m_x \frac{\partial}{\partial x} + m_y \frac{\partial}{\partial y} \right) m_z \right] dS, \tag{6.9}$$

$$E_{\mathrm{ani}} = \mathcal{K}h \int \left(1 - m_z^2\right) dS, \tag{6.10}$$

$$E_{\mathrm{zee}} = \mathcal{M}h \int (\boldsymbol{B}.\boldsymbol{m})\, dS. \tag{6.11}$$

In particular, the relation to the parameters $D$, $K$, $\mu$ of the atomistic spin model on a honeycomb lattice is given by the following equations:

$$\mathcal{D} = \frac{\sqrt{3}}{3ah} D, \quad \mathcal{K} = \frac{4\sqrt{3}}{9a^2 h} K, \quad \mathcal{M} = \frac{4\sqrt{3}}{9a^2 h} \mu \tag{6.12}$$

Similar formulas relate $\mathcal{A}$, $\mathcal{D}$, $\mathcal{K}$ to the parameters $J'$, $D'$, $K'$ of the square-lattice model:

$$\mathcal{A} = \frac{1}{2h} J', \quad , \mathcal{D} = \frac{1}{ah} D', \quad \mathcal{K} = \frac{1}{a^2 h} K', \quad \mathcal{M} = \frac{1}{a^2 h} \mu' \tag{6.13}$$

It is assumed that both lattice models are characterized by the same nearest-neighbor distance $a$.

## 6.2 Appendix B

### 6.2.1 The adiabatic elimination

The adiabatic elimination method allows us to reduce the dimensionality of a problem by discarding fast degree of freedom. As a result of this approximation, in this work the spin of exciton follows the magnetization pattern of skyrmion.

The Schrodinger equation is written in the form:

$$\left[\frac{\hat{P}^2}{2\mu_X}\mathbf{1}_2 + \hat{U}\right]|\Psi\rangle = E_{\mathrm{CM}}|\Psi\rangle \tag{6.14}$$

where $\hat{P} = -i\hbar\nabla$ is the momentum operator and $\mathbf{1}_2$ is identity matrix of size 2. Here $\hat{U} = \lambda\vec{\mathcal{M}}\vec{\sigma}$, $\lambda$ is the interaction energy and $\vec{\sigma}$ is pauli matrix.

So,

$$U = \lambda\begin{pmatrix}\mathcal{M}_z & 0\\ 0 & -\mathcal{M}_z\end{pmatrix} + \begin{pmatrix}0 & \mathcal{M}_x - i\mathcal{M}_y\\ \mathcal{M}_x + i\mathcal{M}_y & 0\end{pmatrix} \tag{6.15}$$

$$U = \lambda\begin{pmatrix}\mathcal{M}_z & \mathcal{M}_r e^{-i\varphi}\\ \mathcal{M}_r e^{i\varphi} & -\mathcal{M}_z\end{pmatrix} \tag{6.16}$$

The eigenvectors of the matrix $U$ read are as following:

$$|\chi_1\rangle = \frac{1}{\sqrt{2(1+\mathcal{M}_z)}}\begin{pmatrix}\mathcal{M}_r\\ -(1+\mathcal{M}_z)e^{i\varphi}\end{pmatrix}, \tag{6.17}$$

$$|\chi_2\rangle = \frac{1}{\sqrt{2(1-\mathcal{M}_z)}}\begin{pmatrix}\mathcal{M}_r\\ (1-\mathcal{M}_z)e^{i\varphi}\end{pmatrix}. \tag{6.18}$$

And with applying the following anzats:

$$|\Psi\rangle = \psi_1|\chi_1\rangle + \psi_2|\chi_2\rangle, \tag{6.19}$$

where $\chi_i$ are the eigenvectors of operator $U$ with energies $u_{1,2} = \pm\lambda$. We further assume $\psi_2 = 0$ where $\psi_2$ remains negligible at all times.

$$\frac{1}{2\mu_X}\langle\chi_1|\hat{P}^2\psi_1|\chi_1\rangle = (E_{\mathrm{CM}} + \lambda)\psi_1. \tag{6.20}$$

and using the completeness relation $|\chi_1\rangle\langle\chi_1| + |\chi_2\rangle\langle\chi_2| = \mathbf{1}$, get

$$\frac{1}{2\mu_X}\langle\chi_1|\hat{P}(|\chi_1\rangle\langle\chi_1| + |\chi_2\rangle\langle\chi_2|)\hat{P}\psi_1|\chi_1\rangle = (E_{\mathrm{CM}} + \lambda)\psi_1. \tag{6.21}$$

Expanding, we reach at

$$\begin{aligned}\frac{1}{2\mu_X}\Bigg[&\langle\chi_1|\hat{P}|\chi_1\rangle(\hat{P}\psi_1) + \hat{P}^2\psi_1 + \Big(\langle\chi_1|\hat{P}|\chi_1\rangle\psi_1 + \hat{P}\psi_1\Big)\langle\chi_1|\hat{P}|\chi_1\rangle \\ &+ \psi_1\hat{P}\langle\chi_1|\hat{P}|\chi_1\rangle + \langle\chi_1|\hat{P}|\chi_2\rangle\psi_1\langle\chi_2|\hat{P}|\chi_1\rangle\Bigg] = (E_{\mathrm{CM}} + \lambda)\psi_1\end{aligned} \tag{6.22}$$

We note that $\langle\chi_1|\hat{P}\chi_2\rangle = -\langle\chi_2|\hat{P}\chi_1\rangle$, and introduce the notations

$$\vec{A} = i\frac{\hbar}{e}\langle\chi_1|\nabla\chi_1\rangle, \tag{6.23}$$

$$W = \frac{\hbar^2}{2\mu_X}|\langle\chi_2|\nabla\chi_1\rangle|^2, \tag{6.24}$$

We see two geometric potentials $A$ and $W$ emerge in adiabatic elimination. The first one is the vector potential and second one is scaler potential.

So now we can rewrite the equation for $\psi_1$ in the form:

$$\left[\frac{1}{2\mu_X}(\hat{P} - e\vec{A})^2 + W - \lambda\right]\psi_1 = E_{\mathrm{CM}}\psi_1. \tag{6.25}$$

We proceed with the explicit calculations of the terms involved in Eq. (6.25). The functions $\mathcal{M}_\rho$, $\mathcal{M}_z$ depend only on radial coordinate, so that

$$\vec{A} = -\frac{\hbar}{e}\frac{1+\mathcal{M}_z}{2\rho}\vec{\varphi}, \tag{6.26}$$

$$W = \frac{\hbar^2}{2\mu_X}\left[\frac{(\mathcal{M}_z\mathcal{M}_r' - \mathcal{M}_r\mathcal{M}_z')^2}{4} + \frac{\mathcal{M}_r^2}{4\rho^2}\right], \tag{6.27}$$

where $'$ denotes the derivative over $\rho$. The effective magnetic field is associated with $A$ is

$$\vec{B}^{\,\text{eff}} = \nabla \times \vec{A} \tag{6.28}$$

$$B_z^{\,\text{eff}} = \frac{A_\varphi}{\rho} + \frac{\partial A_\varphi}{\partial \rho}. \tag{6.29}$$

Note that if we consider the adiabatic following of $|\chi_2\rangle$ instead of $|\chi_1\rangle$, the equation of motion for $\psi_2$ contains the same scalar potential $W$ and the opposite vector potential $-A$.

## 6.2.2 Scattering cross-section

### 6.2.2.1 Matrix elements in Born approximation

The effective potential of scatterer reads as

$$\hat{V} = \frac{1}{2\mu_X}\left(-e\hat{P}\cdot\vec{A} - e\vec{A}\cdot\hat{P} + e^2\vec{A}^2\right) + W \tag{6.30}$$

Correspondingly, the scattering matrix element reads as:

$$V(\vec{k},\vec{k}') = \frac{1}{(2\pi)^2}\int e^{-i\vec{k}'\vec{\rho}}\left[\frac{1}{2\mu_X}\left(-e(\hat{P}\cdot\vec{A}) - 2e\vec{A}\cdot\hat{P} + e^2\vec{A}^2\right) + W\right] e^{i\vec{k}\vec{\rho}}d^2\rho \tag{6.31}$$

Here the term $(\hat{P}\cdot\vec{A})$ vanishes, as $\vec{A}=A(\rho)\vec{\varphi}$. Then one has

$$V(\vec{k},\vec{k}')=\frac{1}{2\pi}\int_0^\infty J_0(|\Delta\vec{k}|\rho)\left(\frac{e^2}{2\mu_X}\vec{A}^2+W\right)\rho d\rho$$
$$-\frac{e\hbar}{2\mu_X}\frac{2}{(2\pi)^2}\int e^{-i\Delta\vec{k}\vec{\rho}}A(\rho)\vec{\varphi}\cdot\vec{k}d^2\rho \tag{6.32}$$

where $\Delta\vec{k}=\vec{k}'-\vec{k}$. We further note, that $\vec{\varphi}\cdot\vec{k}=[\vec{\rho}\times\vec{k}]_z/\rho$. Substituting, and integrating over the angular variable, we get

$$V(\vec{k},\vec{k}')=\frac{1}{2\pi}\int_0^\infty J_0(|\Delta\vec{k}|\rho)\left(\frac{e^2}{2\mu_X}\vec{A}^2+W\right)\rho d\rho$$
$$-\frac{i}{\pi}\frac{e\hbar}{2\mu_X}\frac{[\vec{k}'\times\vec{k}]_z}{|\Delta\vec{k}|}\int_0^\infty J_1(|\Delta\vec{k}|\rho)A(\rho)\rho d\rho \tag{6.33}$$

We restrict the consideration with elastic scattering, so that $|\vec{k}'|=|\vec{k}|=k$, $|\Delta\vec{k}|=2k|\sin\theta/2|$, $[\vec{k}'\times\vec{k}]_z=k^2\sin\theta$. Plugging in, we finally get

$$V(k,\theta)=\frac{1}{2\pi}\int J_0(2k|\sin\theta/2|\rho)\left(\frac{e^2}{2\mu_X}\vec{A}^2+W\right)\rho d\rho$$
$$-\frac{i}{\pi}\frac{e\hbar}{2\mu_X}k(\theta)\cos\theta/2\int J_1(2k|\sin\theta/2|\rho)A(\rho)\rho d\rho. \tag{6.34}$$

To proceed further, we introduce dimensionless quantities as $\rho=ra_0$, $W(\rho)=\hbar^2/(2\mu_X a_0^2)\mathcal{W}(r)$ $A(\rho)=\hbar/(ea_0)\mathcal{A}(r)$, $k=q/a_0$. We then can rewrite

$$V(k,\theta)=\frac{\hbar^2}{2\mu_X}\left[\frac{1}{2\pi}\int_0^\infty J_0(2q|\sin\theta/2|r)\left(\vec{\mathcal{A}}^2(r)+\mathcal{W}(r)\right)rdr\right.$$
$$-\frac{i}{\pi}q(\theta)\cos\theta/2\int_0^\infty J_1(2q|\sin\theta/2|r)\mathcal{A}(r)rdr$$
$$:=\frac{\hbar^2}{2\mu_X}\left[f(q,\theta)+ig(q,\theta)\right] \tag{6.35}$$

It is thus evident, that the real part is an even function of $\theta$, and the imaginary part is odd. The vector gauge field can be presented in the form

$$\mathcal{A}(r) = \begin{cases} \mathcal{A}_1(r), & r \leq r_0, \\ -1/r, & r > r_0, \end{cases} \tag{6.36}$$

where $r_0 = \rho_0/a_0$ is the corresponding inflection point. For the imaginary part of $V(k,\theta)$ we get

$$g(q,\theta) = g_1(q,\theta) + g_2(q,\theta) \tag{6.37}$$

where

$$\begin{aligned} g_1(q,\theta) = -\frac{q}{\pi}(\theta)\cos\theta/2 \int_0^{r_0} J_1(2q|\sin\theta/2|r)\mathcal{A}_1(r)rdr \\ := \cos\theta/2 g_{01}(q,\theta) \end{aligned} \tag{6.38}$$

$$g_2(q,\theta) = \frac{1}{\pi}(\theta)\cos\theta/2 \frac{J_0(2r_0q|\sin\theta/2|)}{2|\sin\theta/2|} \tag{6.39}$$

The real part of matrix element can be presented as

$$f(q,\theta) = f_1(q,\theta) + f_2(q,\theta), \tag{6.40}$$

where

$$f_1(q,\theta) = f_{A1}(q,\theta) + f_{A2}(q,\theta) + f_W(q,\theta) \tag{6.41}$$

with

$$f_W(q,\theta) = \frac{1}{2\pi} \int_0^{\infty} J_0(2q|\sin\theta/2|r)\mathcal{W}(r)rdr \tag{6.42}$$

$$f_{A1}(q,\theta) = \frac{1}{2\pi}\int_0^{r_0} J_0(2q|\sin\theta/2|r)\mathcal{A}_1^2(r)rdr \tag{6.43}$$

$$f_{A2}(q,\theta) = \frac{1}{2\pi}\left[\frac{r_0^2q^2\sin^2(\theta/2)}{2}F(\{1,1\},\{2,2,2\},-r_0^2q^2\sin^2(\theta/2)) - \gamma\right] \tag{6.44}$$

$$f_2(q,\theta) = -\frac{1}{2\pi}\log[r_0q|\sin(\theta/2)|] \tag{6.45}$$

Here $\gamma$ is the Euler gamma, and $F$ is a Hypergeometric function.

### 6.2.3 The calculation of asymmetric correction

The symmetric and asymmetric third order terms of scattering cross-section have the form

$$\omega_s^{(3)}(\vec{k},\vec{k}') = \frac{\mu_X^2}{2\pi\hbar^4k}2\mathcal{P}\left\{Re\left[V(\vec{k},\vec{k}')\sum_{\vec{k}''}\frac{V(\vec{k}',\vec{k}'')V(\vec{k}'',\vec{k})}{\epsilon_k-\epsilon_{k''}}\right]\right\} \tag{6.46}$$

$$\omega_a^{(3)}(\vec{k},\vec{k}') = -\frac{\mu_X^2}{2\pi\hbar^4k}2\pi Im\left[V(\vec{k},\vec{k}')\sum_{\vec{k}''}V(\vec{k}',\vec{k}'')V(\vec{k}'',\vec{k})\delta(\epsilon_k-\epsilon_{k''})\right] \tag{6.47}$$

Below we evaluate the asymmetric term. This implies the calculation of the term

$$\begin{aligned} V^{(1)}_{\vec{k},\vec{k}'} &= \sum_{k''}V(\vec{k}',\vec{k}'')V(\vec{k}'',\vec{k})\delta(\epsilon_k-\epsilon_{k''}) \\ &= \frac{2\mu}{\hbar^2}\frac{1}{(2\pi)^2}\left[\int_0^{\theta}V^*(k,\theta-\varphi)V^*(k,\varphi)d\varphi + \int_{\theta}^{2\pi}V(k,\varphi-\theta)V^*(k,\varphi)d\varphi\right] \end{aligned} \tag{6.48}$$

Using the even and odd parity of real and imaginary parts of $V(q,\theta)$, we can rewrite:

$$V^{(1)}(q,\theta) = \frac{\hbar^2}{2\mu_X}\frac{1}{(2\pi)^2}\left[I_1(q,\theta)+I_2(q,\theta)+i\left(I_3(q,\theta)+I_4(q,\theta)\right)\right] \tag{6.49}$$

where

$$I_1(q,\theta) = \int_0^{2\pi} f(q,\varphi-\theta) f(q,\varphi) d\varphi \tag{6.50}$$

$$I_2(q,\theta) = \int_0^{2\pi} g(q,\varphi-\theta) g(q,\varphi)(\varphi-\theta) d\varphi \tag{6.51}$$

$$I_3(q,\theta) = -\int_0^{2\pi} f(q,\varphi-\theta) g(q,\varphi) d\varphi \tag{6.52}$$

$$I_4(q,\theta) = \int_0^{2\pi} f(q,\varphi) g(q,\varphi-\theta)(\varphi-\theta) d\varphi \tag{6.53}$$

The term $I_1$ can be directly evaluated numerically. Consider the term $I_3$. One can write

$$I_3(q,\theta) = I_{31}(q,\theta) + I_{32}(q,\theta) + I_{33}(q,\theta) + I_{34}(q,\theta) \tag{6.54}$$

where

$$I_{31}(q,\theta) = -\int_0^{2\pi} f_1(q,\varphi-\theta) g_1(q,\varphi) d\varphi \tag{6.55}$$

$$I_{32}(q,\theta) = \frac{1}{2\pi} \int_0^{2\pi} \log[r_0 q| \sin\frac{\varphi-\theta}{2}|] g_1(q,\varphi) d\varphi \tag{6.56}$$

$$I_{33}(q,\theta) = -\int_0^{2\pi} f_1(q, |\sin\frac{\varphi-\theta}{2}|)\frac{1}{\pi}\cos\frac{\varphi}{2}\frac{J_0(2r_0q|\sin\frac{\varphi}{2}|)}{2|\sin\frac{\varphi}{2}|}d\varphi \tag{6.57}$$

$$I_{34}(q,\theta) = \frac{1}{2\pi}\int_0^{2\pi} \log[r_0q|\sin\frac{\varphi-\theta}{2}|]\frac{1}{\pi}\cos\frac{\varphi}{2}\frac{J_0(2r_0q|\sin\frac{\varphi}{2}|)}{2|\sin\frac{\varphi}{2}|}d\varphi \tag{6.58}$$

Denoting $\sin\frac{\varphi}{2} = x$, we can rewrite

$$\begin{aligned} I_{31}(q,\theta) = -2\int_0^1 \Big[ & f_1(q, |x\cos\frac{\theta}{2} - \sqrt{1-x^2}\sin\frac{\theta}{2}|) \\ & - f_1(q, |x\cos\frac{\theta}{2} + \sqrt{1-x^2}\sin\frac{\theta}{2}|)\Big] \\ & g_{01}(q,|x|)dx \end{aligned} \tag{6.59}$$

$$\begin{aligned} I_{32}(q,\theta) = \frac{1}{\pi}\int_0^1 \Big[ & \log(r_0q|x\cos\frac{\theta}{2} - \sqrt{1-x^2}\sin\frac{\theta}{2}|) \\ & - \log(r_0q|x\cos\frac{\theta}{2} + \sqrt{1-x^2}\sin\frac{\theta}{2}|)\Big] \\ & g_{01}(q,|x|)dx \end{aligned} \tag{6.60}$$

$$\begin{aligned} I_{33}(q,\theta) = -\frac{2}{\pi}\int_0^1 \Big[ & f_1(q, |x\cos\frac{\theta}{2} - \sqrt{1-x^2}\sin\frac{\theta}{2}|) \\ & - f_1(q, |x\cos\frac{\theta}{2} + \sqrt{1-x^2}\sin\frac{\theta}{2}|)\Big] \\ & \frac{J_0(2r_0q|x|)}{2|x|}dx \end{aligned} \tag{6.61}$$

$$I_{34}(q,\theta) = \frac{1}{\pi^2}\int_0^1 \Big[\log(r_0 q|x\cos\frac{\theta}{2} - \sqrt{1-x^2}\sin\frac{\theta}{2}|) - \log(r_0 q|x\cos\frac{\theta}{2} + \sqrt{1-x^2}\sin\frac{\theta}{2}|)\Big] \frac{J_0(2r_0 q|x|)}{2|x|}dx, \tag{6.62}$$

which can be easily evaluated. The term $I_4$ exactly coincides with the $I_3$. We finally consider the term $I_2$, reading as:

$$I_2(q,\theta) = I_{21}(q,\theta) + I_{22}(q,\theta) + I_{23}(q,\theta) + I_{24}(q,\theta) \tag{6.63}$$

where

$$I_{21}(q,\theta) = \int_0^{2\pi} g_1(q,\varphi-\theta)g_1(q,\varphi)(\varphi-\theta)\mathrm{d}\varphi \tag{6.64}$$

$$I_{22}(q,\theta) = \frac{1}{\pi}\int_0^{2\pi} g_{01}(q,|\sin\frac{\varphi-\theta}{2}|)\cos\frac{\varphi-\theta}{2}\cos\frac{\varphi}{2}\frac{J_0(2r_0 q|\sin\frac{\varphi}{2}|)}{2|\sin\frac{\varphi}{2}|}(\varphi-\theta)d\varphi \tag{6.65}$$

$$I_{23}(q,\theta) = \frac{1}{\pi}\int_0^{2\pi} g_{01}(q,|\sin\frac{\varphi}{2}|)\cos\frac{\varphi}{2}\cos\frac{\varphi-\theta}{2}\frac{J_0(2r_0 q|\sin\frac{\varphi-\theta}{2}|)}{2|\sin\frac{\varphi-\theta}{2}|}(\varphi-\theta)\mathrm{d}\varphi \tag{6.66}$$

$$I_{24}(q,\theta) = \frac{1}{\pi^2}\int_0^{2\pi} \frac{J_0(2r_0 q|\sin\frac{\varphi}{2}|)}{2|\sin\frac{\varphi}{2}|}\cos\frac{\varphi}{2}\cos\frac{\varphi-\theta}{2}\frac{J_0(2r_0 q|\sin\frac{\varphi-\theta}{2}|)}{2|\sin\frac{\varphi-\theta}{2}|}(\varphi-\theta)\mathrm{d}\varphi \tag{6.67}$$

The term $I_{21}$ can be evaluated directly. For the term $I_{22}$ we again introduce the notation $x = \sin\frac{\varphi}{2}$, and after some computation reach to

$$I_{22}(q,\theta) = \frac{2}{\pi}\Bigg[\cos\frac{\theta}{2}\int_0^1 \sqrt{1-x^2}\frac{J_0(2r_0qx)}{2x}\Bigg(g_{01}(q,|x\cos\frac{\theta}{2}-\sqrt{1-x^2}\sin\frac{\theta}{2}|)(2\arcsin x-\theta) \\ +g_{01}(q,|x\cos\frac{\theta}{2}+\sqrt{1-x^2}\sin\frac{\theta}{2}|)(2\pi-2\arcsin x-\theta)\Bigg)dx \\ +\sin\frac{\theta}{2}\int_0^1 x\frac{J_0(2r_0qx)}{2x}\Bigg(g_{01}(q,|x\cos\frac{\theta}{2}-\sqrt{1-x^2}\sin\frac{\theta}{2}|)(2\arcsin x-\theta) \\ -g_{01}(q,|x\cos\frac{\theta}{2}+\sqrt{1-x^2}\sin\frac{\theta}{2}|)(2\pi-2\arcsin x-\theta)\Bigg)dx\Bigg] \tag{6.68}$$

The term $I_{23}$ is identical to $I_{22}$. The term $I_{24}$ after some algebra takes the form

$$I_{24}(q,\theta) = I_{241}(q,\theta) + I_{242}(q,\theta) + I_{243}(q,\theta) + I_{244}(q,\theta) \tag{6.69}$$

where

$$I_{241}(q,\theta) = \frac{2}{\pi^2}\cos\frac{\theta}{2}\int_0^1 \sqrt{1-x^2}\frac{J_0(2r_0qx)}{2x}\frac{J_0(2r_0q|x\cos\frac{\theta}{2}-\sqrt{1-x^2}\sin\frac{\theta}{2}|)}{2|x\cos\frac{\theta}{2}-\sqrt{1-x^2}\sin\frac{\theta}{2}|} \\ (2\arcsin(x)-\theta)dx \tag{6.70}$$

$$I_{242}(q,\theta) = \frac{2}{\pi^2}\cos\frac{\theta}{2}\int_0^1 \sqrt{1-x^2}\frac{J_0(2r_0kx)}{2x}\frac{J_0(2r_0q|x\cos\frac{\theta}{2}+\sqrt{1-x^2}\sin\frac{\theta}{2}|)}{2|x\cos\frac{\theta}{2}+\sqrt{1-x^2}\sin\frac{\theta}{2}|} \\ (2\pi-2\arcsin(x)-\theta)dx \tag{6.71}$$

$$I_{243}(q,\theta) = \frac{2}{\pi^2}\sin\frac{\theta}{2}\int_0^1 x\frac{J_0(2r_0qx)}{2x}\frac{J_0(2r_0q|x\cos\frac{\theta}{2}-\sqrt{1-x^2}\sin\frac{\theta}{2}|)}{2|x\cos\frac{\theta}{2}-\sqrt{1-x^2}\sin\frac{\theta}{2}|} \\ (2\arcsin(x)-\theta)dx \tag{6.72}$$

$$I_{244}(q,\theta) = \frac{2}{\pi^2}\sin\frac{\theta}{2}\int_0^1 x\frac{J_0(2r_0qx)}{2x}\frac{J_0(2r_0q|x\cos\frac{\theta}{2}+\sqrt{1-x^2}\sin\frac{\theta}{2}|)}{2|x\cos\frac{\theta}{2}+\sqrt{1-x^2}\sin\frac{\theta}{2}|} (2\pi - 2\arcsin(x) - \theta)dx \tag{6.73}$$

For the case $0 \leq \theta \leq \pi$ the terms $I_{242}$, $I_{244}$ can be evaluated directly. The terms $I_{241}$, $I_{243}$ can be treated as principal value integrals, reading as

$$I_{241}(q,\theta) = \frac{2}{\pi^2}\cos\frac{\theta}{2}\lim_{\epsilon\to 0^+}\left[\int_0^{\sin\frac{\theta}{2}-\epsilon}\sqrt{1-x^2}\frac{J_0(2r_0qx)}{2x}\frac{J_0(2r_0q|x\cos\frac{\theta}{2}-\sqrt{1-x^2}\sin\frac{\theta}{2}|)}{2\left(x\cos\frac{\theta}{2}-\sqrt{1-x^2}\sin\frac{\theta}{2}\right)}dx + \int_{\sin\frac{\theta}{2}+\epsilon}^1\sqrt{1-x^2}\frac{J_0(2r_0qx)}{2x}\frac{J_0(2r_0q|x\cos\frac{\theta}{2}-\sqrt{1-x^2}\sin\frac{\theta}{2}|)}{2\left(x\cos\frac{\theta}{2}-\sqrt{1-x^2}\sin\frac{\theta}{2}\right)}dx\right] \tag{6.74}$$

$$I_{243}(q,\theta) = \frac{2}{\pi^2}\sin\frac{\theta}{2}\lim_{\epsilon\to 0^+}\left[\int_0^{\sin\frac{\theta}{2}-\epsilon}x\frac{J_0(2r_0qx)}{2x}\frac{J_0(2r_0q|x\cos\frac{\theta}{2}-\sqrt{1-x^2}\sin\frac{\theta}{2}|)}{2\left(x\cos\frac{\theta}{2}-\sqrt{1-x^2}\sin\frac{\theta}{2}\right)}dx + \int_{\sin\frac{\theta}{2}+\epsilon}^1 x\frac{J_0(2r_0kx)}{2x}\frac{J_0(2r_0k|x\cos\frac{\theta}{2}-\sqrt{1-x^2}\sin\frac{\theta}{2}|)}{2\left(x\cos\frac{\theta}{2}-\sqrt{1-x^2}\sin\frac{\theta}{2}\right)}dx\right] \tag{6.75}$$

The same regularization is required for the terms $I_{242}$, $I_{244}$ in the region $\pi < \theta \leq 2\pi$.

# 6.3 Appendix C

## 6.3.1 Matrix elements of the exciton Hamiltonian

The matrix elements of the exciton Hamiltonian $H_{\text{exc}} + H_{\text{s}}$ are computed via the resolution of the Bethe-Salpeter equation (BSE) parameterized using the first-principles calculations. The exciton wave functions and associated energies are obtained by diagonalizing the BSE Hamiltonian [53, 143, 144] as follows:

$$\sum_{c'v'\mathbf{k}'} H^{BSE}_{cv\mathbf{k}c'v'\mathbf{k}'}(\mathbf{q}) A^{n\mathbf{q}}_{c'v'\mathbf{k}'} = E^{n\mathbf{q}} A^{n\mathbf{q}}_{cv\mathbf{q}}, \tag{6.76}$$

Here, $H^{BSE}_{cv\mathbf{k}c'v'\mathbf{k}'}(\mathbf{q})$ are the matrix elements of the BSE Hamiltonian for excitons possessing momentum $\mathbf{q}$, $A^{n\mathbf{q}}_{cv\mathbf{q}}$ and $E^{n\mathbf{q}}$ are the $n$th exciton wave function and energy, respectively. The indices $c$ ($c'$), $v$ ($v'$), and $\mathbf{k}$ ($\mathbf{k}'$) denote the conduction band, valence band, and single-particle momentum, respectively. The Hamiltonian $H^{BSE}$ is calculated using the Tamm-Dancoff approximation [143], which is particularly well-suited for wide-gap semiconductors. This approximation disregards the coupling between resonance and anti-resonance poles while preserving the Hermitian character of the Hamiltonian.

The calculation of the dipole matrix elements is carried out utilizing the following equation:

$$\boldsymbol{D}_{n\mathbf{q}=0} = \langle 0|\boldsymbol{r}|n\mathbf{q}=0\rangle = \sum_{cv\mathbf{k}} A^{n\mathbf{q}=0}_{cv\mathbf{k}} \langle v\mathbf{k}|\boldsymbol{r}|c\mathbf{k}\rangle, \tag{6.77}$$

where $\langle v\mathbf{k}|\boldsymbol{r}|c\mathbf{k}\rangle$ is the single-particle dipole matrix element corresponding to the optical transition from the conduction band $c$ to the valence band $v$ with momentum $\mathbf{k}$.

The key ingredients of the exciton-skyrmion Hamiltonian interaction are the matrix elements of the exciton magnetic moment $\boldsymbol{M}^{\mathbf{q}\mathbf{q}'}_{nn'}$. These matrix elements are assembled from the matrix elements of the spin magnetic moment $\boldsymbol{S}^{\mathbf{q}\mathbf{q}'}_{nn'}$ and the orbital magnetic moment $\boldsymbol{L}^{\mathbf{q}\mathbf{q}'}_{nn'}$. The matrix elements of the spin magnetic moment are calculated from the single-particle spin moment:

$$\begin{aligned}\boldsymbol{S}^{\mathbf{q}\mathbf{q}'}_{nn'} = &\sum_{cv\mathbf{k},c'v'\mathbf{k}'} \left(A^{n\mathbf{q}}_{cv\mathbf{k}}\right)^* A^{n'\mathbf{q}'}_{c'v'\mathbf{k}'} \\ &\times \left[\langle c\mathbf{k}+\mathbf{q}|\boldsymbol{S}|c'\mathbf{k}'+\mathbf{q}'\rangle - \langle v'\mathbf{k}'|\boldsymbol{S}|v\mathbf{k}\rangle\right],\end{aligned} \tag{6.78}$$

where $\langle c\mathbf{k}|\boldsymbol{S}|c'\mathbf{k}'\rangle$ is the single-particle spin matrix element. While the single-particle spin operators are simply defined using the Pauli matrices in the spin subspace, the

calculation of the orbital moment requires a more careful consideration. In our study, we employ a local projector augmented wave (PAW) technique to evaluate the orbital single-particle magnetic moment, as it offers a more straightforward approach compared to the previously reported perturbation theory-based methods [145–149]. All-electron orbitals inside the PAW sphere can be expanded as [150, 151]

$$|c\mathbf{k}\rangle = \sum_i \langle p_i^a | \varphi_{c\mathbf{k}} \rangle | \phi_i^a \rangle, \tag{6.79}$$

where $p_i^a$ is a projector of the smooth pseudowave function $\varphi_{c\mathbf{k}}$ for band $c$ with momentum $\mathbf{k}$ on the $i$th all-electron partial wave for atom $a$, $\phi_i^a$. We calculate the one-particle matrix elements of the orbital momentum as follows [52]:

$$\langle c\mathbf{k}|\boldsymbol{L}|c'\mathbf{k}'\rangle = \sum_{a i_1 i_2} \langle \varphi_{c\mathbf{k}}|p_{i_1}^a\rangle \langle \phi_{i1}^a|\boldsymbol{L}^a|\phi_{i2}^a\rangle \langle p_{i_2}^a|\varphi_{c'\mathbf{k}'}\rangle, \tag{6.80}$$

where $\boldsymbol{L}^a$ is the orbital momentum operator for atom $a$. Since partial waves $\phi_i^a$ are usually defined in a spherical basis, the matrix elements $\langle \phi_{i1}^a|\boldsymbol{L}^a|\phi_{i2}^a\rangle$ can be calculated analytically. Having single-particle matrix elements of the orbital magnetic moment, we compute the exciton matrix elements as follows:

$$\begin{aligned} \boldsymbol{L}_{nn'}^{\mathbf{q}\mathbf{q}'} = & \sum_{cv\mathbf{k},c'v'\mathbf{k}'} \left(A_{cv\mathbf{k}}^{n\mathbf{q}}\right)^* A_{c'v'\mathbf{k}'}^{n'\mathbf{q}'} \\ & \times \left[\langle c\mathbf{k}+\mathbf{q}|\boldsymbol{L}|c'\mathbf{k}'+\mathbf{q}'\rangle - \langle v'\mathbf{k}'|\boldsymbol{L}|v\mathbf{k}\rangle\right]. \end{aligned} \tag{6.81}$$

The total exciton magnetic moment is obtained by computing a sum of the spin and orbital components:

$$\boldsymbol{M}_{nn'}^{\mathbf{q}\mathbf{q}'} = \boldsymbol{L}_{nn'}^{\mathbf{q}\mathbf{q}'} + \boldsymbol{S}_{nn'}^{\mathbf{q}\mathbf{q}'}. \tag{6.82}$$

### 6.3.2 Introduction of damping

The effects of damping are modeled by introducing finite inverse relaxation time $\delta$, which results in the decay of excited exitonic states $\sim \exp(-\Delta t\delta)$ with time $\Delta t$. For simplicity, the damping parameter is assumed to be the same for all excited excitonic states. Therefore, at each time step of the simulation, the vector of state $\Psi_{\text{exc}} = (\psi_0, \psi_1, \ldots, \psi_n)$ with $\psi_0$ being the component responsible for vacuum, is substituted by the modified vector of state $\Psi_{\text{exc}} \leftarrow \tilde{\Psi}_{\text{exc}} = (\tilde{\psi}_0, \tilde{\psi}_1, \ldots, \tilde{\psi}_n)$, whose componens are defined via the following operations:

$$\tilde{\psi}_i = \psi_i \sqrt{1 - \Delta t\delta}, i > 0 \tag{6.83}$$

$$\Delta = 1 - \left(\sum_{i=1}^{n} |\tilde{\psi}_i|^2 + |\psi_0|^2\right), \tag{6.84}$$

$$\tilde{\psi}_0 = \psi_0 \frac{\sqrt{\Delta + |\psi_0|^2}}{|\psi_0|}. \tag{6.85}$$

Note that $|\tilde{\Psi}_{\text{exc}}| = |\Psi_{\text{exc}}| = 1$. We also should emphasize that shorter exciton lifetime (stronger damping of the excitonic states) leads to slower magnetization switching. Unfortunately, we do not have the data for the exciton damping in $CrI_3$ for each specific excitonic state. To overcome this problem, for all states we use an estimate $\delta = 80$ meV from Ref.[77], where the measurement of the broadening of a particular peak was made. This value is significantly higher than those that are usually found, for example, for TMDs. Probably, it is connected with the fact that in these materials, there is a strong exciton-phonon interaction due to the localized nature of excitons. Specifically, the localized nature of excitons makes them sensitive to local, optical, and phonon perturbations.

### 6.3.3 Fourier transforms

The definition of the direct and inverse Fourier transforms used in this study requires a special discussion since the gratings in the real space(r) and momentum space(q) have different discreteness. For an arbitrary function $f$, the Fourier transforms are defined via the following equations:

$$f(\boldsymbol{r}_i) = \sum_j^{N_q} \exp\left[2\pi \mathrm{i} (\boldsymbol{r}_i \boldsymbol{q}_j)_{N_c}\right] f(\boldsymbol{q}_j), \tag{6.86}$$

$$f(\boldsymbol{q}_j) = \frac{1}{N_c} \sum_i^{N_c} \exp\left[-2\pi \mathrm{i} (\boldsymbol{r}_i \boldsymbol{q}_j)_{N_c}\right] f(\boldsymbol{r}_i), \tag{6.87}$$

where $N_c = 30 \times 30 = 900$ is the number of unit cells and $N_q = 6 \times 6 = 36$ is the number of points in the $q$-space. We define the dot product $(\dots)_{N_c}$ as:

$$(\boldsymbol{r}\boldsymbol{q})_{N_c} = \frac{r_i^x q_j^x}{N_c^x} + \frac{r_i^y q_j^y}{N_c^y} + \frac{r_i^z q_j^z}{N_c^z}. \tag{6.88}$$

We use $N_c^x = N_c^y = 30$ and $N_c^z = 1$. Since there are two magnetic atoms per unit cell, we adhere to the following formula to compute the Fourier transform of the magnetization:

$$\boldsymbol{m}_{\mathbf{q}-\mathbf{q}'} = \frac{1}{N_c} \sum_i^{N_c} \exp\left[-2\pi \mathrm{i} (\boldsymbol{r}_i (\mathbf{q} - \mathbf{q}'))_{N_c}\right] \times (\boldsymbol{m}_{2i} + \boldsymbol{m}_{2i-1}), \tag{6.89}$$

where we use the total magnetic moment of the unit cell.

# 7 Original articles

## Article I

**Interaction of excitons with magnetic topological defects in 2D magnetic monolayers: localization and anomalous Hall effect**
M Kazemi, V A Shahnazaryan, Y V Zhumagulov, P F Bessarab and I A Shelykh
2D Mater, **10**, 015003 (2022).

## Article II

**All-optical magnetization control in $CrI_3$ monolayers: A microscopic theory**
A. Kudlis, M. Kazemi, Y. Zhumagulov, H. Schrautzer, A. I. Chernov, P. F. Bessarab, I. V. Iorsh, and I. A. Shelykh
Physical Review B, **108**, 094421 (2023)

## Article III

**All-optical control of skyrmion configuration in $CrI_3$ monolayer**
M. Kazemi, A. Kudlis, P. F. Bessarab, and I. A. Shelykh
Scientific Reports, **14.1**, 11677 (2024).

# Bibliography


[1] Heisenberg, Werner. *Zur theorie des ferromagnetismus*, Springer Berlin Heidelberg. (1985).

[2] Nolting, Wolfgang, and Anupuru Ramakanth. *Quantum theory of magnetism*, Springer Science and Business Media. (2009).

[3] Stefan Heinze et al. *Spontaneous atomic-scale magnetic skyrmion lattice in two dimensions*, nature physics. **7.9**, pp. 713–718 (2011).

[4] Dzyaloshinsky, Igor. *A thermodynamic theory of "weak" ferromagnetism of antiferromagnetics*, Journal of physics and chemistry of solids. **4.4**, 241-255 (1958).

[5] Tôru Moriya. *Anisotropic superexchange interaction and weak ferromagnetism*, Physical review. **120.1**, p. 91 (1960).

[6] XZ Yu et al. *Real-space observation of a two-dimensional skyrmion crystal*, Nature. **465.7300**, pp. 901–904 (2010).

[7] Hongxin Yang et al. *Anatomy of dzyaloshinskii-moriya interaction at Co/Pt interfaces*, Physical review letters. **115.26**, p. 267210 (2015).

[8] Landau, Lev Davidovich, and Evgenii Mikhailovich Lifshitz. *Fluid mechanics: Landau And Lifshitz: course of theoretical physics*, Volume 6. Vol. 6. Elsevier, (2013).

[9] Gilbert, Thomas L. *A phenomenological theory of damping in ferromagnetic materials*, IEEE transactions on magnetics. **40.6**, 3443-3449 (2004)

[10] Eriksson, Olle, et al. *Atomistic spin dynamics*, foundations and applications. Oxford university press, (2017).

[11] Wang, X. S., H. Y. Yuan, and X. R. Wang. *A theory on skyrmion size*. Communications Physics. **1.1**, 31 (2018).

[12] Cortés-Ortuño, David, et al. *Nanoscale magnetic skyrmions and target states in confined geometries*. Physical Review B. **99.21**, 214408 (2019).

[13] Bogdanov, Alexei N., and D. A. Yablonskii. *Thermodynamically stable "vortices" in magnetically ordered crystals*, The mixed state of magnets." Zh. Eksp. Teor. Fiz. **95.1**, 178 (1989).

[14] Casiraghi, Arianna, et al. *Individual skyrmion manipulation by local magnetic field gradients*, Communications Physics. **2.1**, 145 (2019).

[15] Wang, Weiwei, et al. *Electrical manipulation of skyrmions in a chiral magnet*, Nature Communications. **13.1**, 1593 (2022).

[16] Yang, Yang, et al. *Acoustic-driven magnetic skyrmion motion*, Nature Communications. **15.1**, 1018 (2024).

[17] Romming, Niklas, et al. *Field-dependent size and shape of single magnetic skyrmions*. Physical review letters. **114.17**, 177203 (2015).

[18] Juge, Roméo, et al. *Magnetic skyrmions in confined geometries: Effect of the magnetic field and the disorder*, Journal of Magnetism and Magnetic Materials. **455**, 3-8 (2018).

[19] Bocdanov, A., and A. Hubert. *The properties of isolated magnetic vortices*. physica status solidi (b). **186.2**, 527-543 (1994).

[20] Lin, Shi-Zeng. *Dynamics and inertia of a skyrmion in chiral magnets and interfaces: A linear response approach based on magnon excitations*. Physical Review B. **96.1**, 014407 (2017)

[21] Klingshirn, Claus F. *Semiconductor optics*, Springer Science, Business Media, 2012.

[22] Wang, Gang, et al. *Colloquium: Excitons in atomically thin transition metal dichalcogenides*, Reviews of Modern Physics. **90.2**, 021001 (2018).

[23] Frenkel, Jacov. *On the transformation of light into heat in solids*, Physical Review. **37.1**, 17 (1931).

[24] Wannier, Gregory H. *The structure of electronic excitation levels in insulating crystals*, Physical Review. **52.3**, 191 (1937).

[25] Wu, Meng, et al. *Physical origin of giant excitonic and magneto-optical responses in two-dimensional ferromagnetic insulators*, Nature communications. **10.1**, 2371 (2019).

[26] Salpeter, Edwin E., and Hans Albrecht Bethe. *A relativistic equation for bound-state problems*, Physical Review. **84.6**, 1232 (1951).

[27] Hanke, W., and L. J. Sham. *Many-particle effects in the optical spectrum of a semiconductor*, Physical Review B. **21.10**, 4656 (1980).

[28] Wang, Hao, Volker Eyert, and Udo Schwingenschlögl. *Electronic structure and magnetic ordering of the semiconducting chromium trihalides CrCl3, CrBr3, and CrI3*, Journal of Physics: Condensed Matter. **23.11**, 116003 (2011).

[29] Zhang, Wei-Bing, et al. *Robust intrinsic ferromagnetism and half semiconductivity in stable two-dimensional single-layer chromium trihalides*, Journal of Materials Chemistry C. **3.48**, 12457-12468 (2015).

[30] Kazemi, M., et al. *Interaction of excitons with magnetic topological defects in 2D magnetic monolayers: localization and anomalous Hall effect*, 2D Materials. **10.1**, 015003 (2022).

[31] Gorchon, Jon, et al. *Role of electron and phonon temperatures in the helicity-independent all-optical switching of GdFeCo*, Physical Review B. **94.18**, 184406 (2016).

[32] Moreno, Roberto, et al. *Conditions for thermally induced all-optical switching in ferrimagnetic alloys: Modeling of TbCo*, Physical Review B. **96.1**, 014409 (2017).

[33] Ignatyeva, D. O., et al. *Plasmonic layer-selective all-optical switching of magnetization with nanometer resolution*, Nature communications. **10.1**, 4786 (2019).

[34] Avilés-Félix, L., et al. *Single-shot all-optical switching of magnetization in Tb/Co multilayer-based electrodes*, Scientific reports. **10.1**, 5211 (2020).

[35] Stanciu, Claudiu D., et al. *All-optical magnetic recording with circularly polarized light*, Physical review letters. **99.4**, 047601 (2007).

[36] Davies, C. S., et al. *Pathways for single-shot all-optical switching of magnetization in ferrimagnets*, Physical Review Applied. **13.2**, 024064 (2020).

[37] Igarashi, Junta, et al. *Engineering single-shot all-optical switching of ferromagnetic materials*, Nano Letters. **20.12**, 8654-8660 (2020).

[38] Lu, Xianyang, et al. *Roles of heating and helicity in ultrafast all-optical magnetization switching in TbFeCo*, Applied Physics Letters. **113.3**, (2018).

[39] El Hadri, Mohammed Salah, et al. *Two types of all-optical magnetization switching mechanisms using femtosecond laser pulses*, Physical review B. **94.6**, 064412 (2016).

[40] van Hees, Youri LW, et al. *Deterministic all-optical magnetization writing facilitated by non-local transfer of spin angular momentum*, Nature communications. **11.1**, 3835 (2020).

[41] Zhang, Peiyao, et al. *All-optical switching of magnetization in atomically thin CrI3*, Nature materials. **21.12**, 1373-1378 (2022).

[42] Huang, Bevin, et al. *Electrical control of 2D magnetism in bilayer CrI 3*, Nature nanotechnology. **13.7**, 544-548 (2018).

[43] McGuire, Michael A., et al. *Coupling of crystal structure and magnetism in the layered, ferromagnetic insulator CrI3*, Chemistry of Materials. **27.2**, 612-620 (2015).

[44] Wu, Meng, et al. *Physical origin of giant excitonic and magneto-optical responses in two-dimensional ferromagnetic insulators*, Nature communications. **10.1**, 2371 (2019).

[45] Chernikov, Alexey, et al. *Exciton binding energy and nonhydrogenic Rydberg series in monolayer WS 2*, Physical review letters. **113.7**, 076802 (2014).

[46] Splendiani, Andrea, et al. *Emerging photoluminescence in monolayer MoS2*, Nano letters. **10.4**, 1271-1275 (2010).

[47] Steinleitner, Philipp, et al. *Direct observation of ultrafast exciton formation in a monolayer of WSe2*, Nano Letters. **17.3**, 1455-1460 (2017).

[48] Wang, Gang, et al. *Colloquium: Excitons in atomically thin transition metal dichalcogenides*, Reviews of Modern Physics. **90.2**, 021001 (2018).

[49] Kudlis, A., I. Iorsh, and I. A. Shelykh. *All-optical resonant magnetization switching in CrI 3 monolayers*, Physical Review B. **104.2**, L020412 (2021).

[50] Mortensen, Jens Jørgen, Lars Bruno Hansen, and Karsten Wedel Jacobsen. *Real-space grid implementation of the projector augmented wave method*, Physical Review B—Condensed Matter and Materials Physics. **71.3**, 035109 (2005).

[51] Enkovaara, Jussi, et al. *Electronic structure calculations with GPAW: a real-space implementation of the projector augmented-wave method*, Journal of physics: Condensed matter. **22.25**, 253202 (2010).

[52] Olsen, Thomas. *Designing in-plane heterostructures of quantum spin Hall insulators from first principles: 1 TMoS 2 with adsorbates*, Physical Review B. **94.23**, 235106 (2016).

[53] Rohlfing, Michael, and Steven G. Louie. *Electron-hole excitations and optical spectra from first principles*, Physical Review B. **62.8**, 4927 (2000).

[54] Yan, Jun, et al. *Linear density response function in the projector augmented wave method: Applications to solids, surfaces, and interfaces*, Physical Review B—Condensed Matter and Materials Physics. **83.24**, 245122 (2011).

[55] Hüser, Falco, Thomas Olsen, and Kristian S. Thygesen. *How dielectric screening in two-dimensional crystals affects the convergence of excited-state calculations: Monolayer MoS 2*, Physical Review B—Condensed Matter and Materials Physics. **88.24**, 245309 (2013).

[56] Olsen, Thomas. *Unified treatment of magnons and excitons in monolayer CrI 3 from many-body perturbation theory*, Physical Review Letters. **127.16**, 166402 (2021).

[57] Ghosh, Sukanya, Nataša Stojić, and Nadia Binggeli. *Comment on "Magnetic skyrmions in atomic thin CrI3 monolayer*, [Appl. Phys. Lett. 114, 232402 (2019)]. Applied Physics Letters. **116.8**, (2020).

[58] Mentink, J. H., et al. *Stable and fast semi-implicit integration of the stochastic Landau–Lifshitz equation*, Journal of Physics: Condensed Matter. **22.17**, 176001 (2010).

[59] Dabrowski, Maciej, et al. *All-optical control of spin in a 2D van der Waals magnet*, Nature Communications. **13.1**, 5976 (2022).

[60]

[61] Du, Ke-zhao, et al. *Weak Van der Waals Stacking, Wide-Range Band Gap, and Raman Study on Ultrathin Layers of Metal Phosphorus Trichalcogenides*, ACS nano. *10.2*, 1738-1743 (2016).

[62] F. Matsukura, Y. Tokura, and H. Ohno. *Control of magnetism by electric fields*, Nature nanotechnology. **10.3**, 209-220 (2015).

[63] Kudlis, A., et al. *All-optical magnetization control in CrI3 monolayers: A microscopic theory*, Physical Review B. **108.9**, 094421 (2023).

[64] N. Nagaosa and Y. Tokura Nagaosa, Naoto, and Yoshinori Tokura. *Topological properties and dynamics of magnetic skyrmions*, Nature nanotechnology. **8.12**, 899-911 (2013).

[65] A. Fert, V. Cros, and J. Sampaio. *Skyrmions on the track*, Nature nanotechnology. **8.3**, 152-156 (2013).

[66] A. Bogdanov and A. Hubert. *Thermodynamically stable magnetic vortex states in magnetic crystals*, Journal of Magnetism and Magnetic Materials. *138.3*, 255-269 (1994).

[67] A. Bocdanov and A. Hubert. *The properties of isolated magnetic vortices*, physica status solidi (b). *186.2*, 186, 527-543 (1994).

[68] A. Bogdanov and A. Hubert. *The stability of vortex-like structures in uniaxial ferromagnets*, Journal of Magnetism and Magnetic Materials. *195.1*, 182-192 (1999).

[69] S. Rohart and A. *Thiaville Skyrmion confinement in ultrathin film nanostructures in the presence of Dzyaloshinskii-Moriya interaction*, Physical Review B. *88.18*, 184422 (2013).

[70] M. Baćani, M. A. Marioni, J. Schwenk, and H. J. Hug. *How to measure the local Dzyaloshinskii-Moriya Interaction in Skyrmion Thin-Film Multilayers*, Scientific reports. *9.1*, 3114 (2019).

[71] X. Wang, H. Yuan, and X. Wang. *A theory on skyrmion size*, Communications Physics. *1.1*, 31 (2018).

[72] Sohn, Hayley RO, et al. *Light-controlled skyrmions and torons as reconfigurable particles*, Optics express. *27.20*, 29055-29068 (2019).

[73] Grebenchuk, Sergey, et al. *Topological Spin Textures in an Insulating van der Waals Ferromagnet*, Advanced Materials. 2311949 (2024).

[74] Tai, Jung-Shen B., et al. *Field-controlled dynamics of skyrmions and monopoles*, Science Advances. *10.4*, eadj9373 (2024).

[75] Wu, Jiang-Bin, Heng Wu, and Ping-Heng Tan. *Magneto-Optical Interactions in Layered Magnets*, Advanced Functional Materials. 2312214 (2024).

[76] H. Wu, X. Hu, K. Jing, and X. Wang. *Size and profile of skyrmions in skyrmion crystals*, Communications Physics. **4.1**, 210 (2021).

[77] M. Wu, Z. Li, T. Cao, and S. G. Louie. *Physical origin of giant excitonic and magneto-optical responses in two-dimensional ferromagnetic insulators*, Nature Communications. **10.1**, 2371 (2019).

[78] Enkovaara, Jussi, et al. *Electronic structure calculations with GPAW: a real-space implementation of the projector augmented-wave method*, Journal of Physics: Condensed Matter. **22.25**, 253202 (2010).

[79] J. J. Mortensen, L. B. Hansen, and K. W. Jacobsen. *Real-space grid implementation of the projector augmented wave method*, Physical Review B. *71.3*, 035109 (2005).

[80] U. K. Rößler, A. N. Bogdanov, and C. Pfleiderer. *Spontaneous skyrmion ground states in magnetic metals*, Nature. **442**, 797 (2006).

[81] N. S. Kiselev, A. N. Bogdanov, R. Schäfer and U. K. Rößler. *Chiral skyrmions in thin magnetic films: new objects for magnetic storage technologies*, J. Phys. D: Appl. Phys. **44**, 392001 (2011).

[82] N. Romming, A. Kubetzka, C. Hanneken, K. von Bergmann and R. Wiesendanger. *Field-dependent size and shape of single magnetic skyrmions*, Phys. Rev. Lett. **114**, 177203 (2015).

[83] L. V. Butov, A. C. Gossard, and D. S. Chemla. *Macroscopically ordered state in an exciton system*, Nature. **418**, 751 (2002).

[84] G. E. Astrakharchik, J. Boronat, I. L. Kurbakov, and Y. E. Lozovik. *Quantum Phase Transition in a Two-Dimensional System of Dipoles*, Phys. Rev. Lett. **98**, 060405 (2007).

[85] A. A. High, J. R. Leonard, A. T. Hammack, M. M. Fogler, L. V. Butov, A. V. Kavokin, K. L. Campman, and A. C. Gossard, *Spontaneous coherence in a cold exciton gas*, Nature. **483**, 584 (2012).

[86] . E. Lozovik, S. L. Ogarkov, A. A. Sokolik, *Condensation of electron-hole pairs in a two-layer graphene system: Correlation effects*, Phys. Rev. B. **86**, 045429 (2012)

[87] M. M. Fogler, L. V. Butov, K. S. Novoselov, *High-temperature superfluidity with indirect excitons in van der Waals heterostructures*, Nature Comm. **5**, 4555 (2014).

[88] J. Kasprzak, M. Richard, S. Kundermann, A. Baas, P. Jeambrun, J. M. J. Keeling, F. M. Marchetti, M. H. Szymanska, R. Andre, J. L. Staehli, V. Savona, P. B. Littlewood, B. Deveaud, and Le Si Dang. *Bose–Einstein condensation of exciton polaritons*, Nature (London). **443**, 409 (2006).

[89] R. Balili, V. Hartwell, D. Snoke, and K. West. *Bose-Einstein Condensation of Microcavity Polaritons in a Trap*, Science **316**, 1007 (2007).

[90] A. Amo, D. Sanvitto, F. P. Laussy, D. Ballarini, E. del Valle, M. D. Martin, A. Lemaitre, J. Bloch, D. N. Krizhanovskii, M. S. Skolnick, C. Tejedor, and L. Vina. *Collective fluid dynamics of a polariton condensate in a semiconductor microcavity*, Nature. **457**, 291 (2009).

[91] K. G. Lagoudakis, M. Wouters, M. Richard, A. Baas, I. Carusotto, R. Andre, L. S. Dang, and B. Deveaud-Pledran. *Quantized vortices in an exciton–polariton condensate*, Nature Phys. **4**, 706 (2008).

[92] G. Tosi, G. Christmann, N. G. Berloff, P. Tsotsis, T. Gao, Z. Hatzopoulos, P. G. Savvidis, and J. J. Baumberg, Geometrically. *locked vortex lattices in semiconductor quantum fluids*, Nat. Commun. **3**, 1243 (2012).

[93] T. Gao, O. A. Egorov, E. Estrecho, K. Winkler, M. Kamp, C. Schneider, S. Hofling, A. G. Truscott, and E. A. Ostrovskaya. *Controlled Ordering of Topological Charges in an Exciton-Polariton Chain*, Phys. Rev. Lett. **121**, 225302 (2018).

[94] M.-S. Kwon, B. Y. Oh, S.-H. Gong, J.-H. Kim, H. K. Kang, S. Kang, J. D. Song, H. Choi, and Y.-H. Cho. *Direct Transfer of Light's Orbital Angular Momentum onto a Nonresonantly Excited Polariton Superfluid*, Phys. Rev. Lett. **122**, 045302 (2019).

[95] S. Seki, X.Z. Yu, S. Ishiwata, and Y. Tokura. *Observation of Skyrmions in a Multiferroic Material*, Science. **336**, 198 (2012).

[96] A. P. Petrović, M. Raju, X. Y. Tee, A. Louat, I. Maggio-Aprile, R. M. Menezes, M. J. Wyszyński, N. K. Duong, M. Reznikov, Ch. Renner, M. V. Milošević, and C. Panagopoulos. *Skyrmion-(Anti)Vortex Coupling in a Chiral Magnet-Superconductor Heterostructure*, Phys. Rev. Lett. **126**, 117205 (2021).

[97] K. S. Burch, D. Mandrus, and J.-G. Park. *Magnetism in two-dimensional van der Waals materials*, Nature. **563**, 47 (2018).

[98] A. R. Wildes, V. Simonet, E. Ressouche, G. J. McIntyre, M. Avdeev, E. Suard, S. A. J. Kimber, D. Lançon, G. Pepe, B. Moubaraki, and T. J. Hicks. *Magnetic structure of the quasi-two-dimensional antiferromagnet NiPS3*, Phys. Rev. B **92**, 224408 (2015).

[99] S. Kang, K. Kim, B. H. Kim, J. Kim, K. I. Sim, J.-U. Lee, S. Lee, K. Park, S. Yun, T. Kim, A. Nag, A. Walters, M. Garcia-Fernandez, J. Li, L. Chapon, K.-J. Zhou, Y.-W. Son, J. H. Kim, H. Cheong, and J.-G. Park, *Coherent many-body exciton in van der Waals antiferromagnet NiPS3*, Nature. **583**, 785 (2020).

[100] C.-H. Ho, T.-Y. Hsu, and L. C. Muhimmah. *The band-edge excitons observed in few-layer NiPS3*, NPJ 2D Mater. Appl. **5**, 1 (2021).

[101] M. Birowska, P. E. Faria Junior, J. Fabian, and J. Kunstmann. *Large exciton binding energies in MnPS3 as a case study of a van der Waals layered magnet*, Phys. Rev. B. **103**, L121108 (2021).

[102] B. Huang, G. Clark, E. Navarro-Moratalla, D. R. Klein, R. Cheng, K. L. Seyler, D. Zhong, E. Schmidgall, M. A. McGuire, D. H. Cobden, W. Yao, D. Xiao, P. Jarillo-Herrero, and X. Xu. *Layer-dependent ferromagnetism in a van der Waals crystal down to the monolayer limit*, Nature. **546**, 270 (2017).

[103] F. Zheng, J. Zhao, Z. Liu, M. Li, M. Zhou, S. Zhang, and P. Zhang. *Tunable spin states in the two-dimensional magnet CrI3*, Nanoscale. **10**, 14298 (2018).

[104] I. V. Kashin, V. V. Mazurenko, M. I. Katsnelson, and A. N. Rudenko. *Orbitally-resolved ferromagnetism of monolayer CrI3*, 2D Mater. **7**, 025036 (2020).

[105] M. Kim, P. Kumaravadivel, J. Birkbeck, W. Kuang, S. G. Xu, D. G. Hopkinson, J. Knolle, P. A. McClarty, A. I. Berdyugin, M. Ben Shalom, R. V. Gorbachev, S. J. Haigh, S. Liu, J.H. Edgar, K. S. Novoselov, I. V. Grigorieva, and A. K. Geim, *Micromagnetometry of two-dimensional ferromagnets*, Nat. Electron. **2**, 457 (2019).

[106] N. D. Mermin, and H. Wagner. *Absence of ferromagnetism or antiferromagnetism in one or two-dimensional isotropic Heisenberg models*, Phys. Rev. Lett. **17**, 1133 (1966).

[107] J. L. Lado, and J. Fernández-Rossier. *On the origin of magnetic anisotropy in two dimensional CrI3*, 2D Mater. **4**, 035002271 (2017).

[108] J. Liu, M. Shi, J. Lu, and M.P. Anantram. *Analysis of electrical-field-dependent Dzyaloshinskii-Moriya interaction and magnetocrystalline anisotropy in a two-dimensional ferromagnetic monolayer*, Phys. Rev. B. **97**, 054416 (2018).

[109] S. Ghosh, N. Stojić, and N. Binggeli. *Structural and magnetic response of CrI3 monolayer to electric field*, Physica B Condens. Matter. **570**, 166 (2019).

[110] S. I. Vishkayi, Z. Torbatian, A. Qaiumzadeh, and R. Asgari. *Strain and electric-field control of spin-spin interactions in monolayer CrI3*, Phys. Rev. Mater. **4**, 094004 (2020).

[111] J. Liu, M. Shi, P. Mo, and J. Lu. *Electrical-field-induced magnetic Skyrmion ground state in a two-dimensional chromium tri-iodide ferromagnetic monolayer*, AIP Advances. **8**, 055316 (2018).

[112] A. K. Behera, S. Chowdhury, and S. R. Das. *Magnetic skyrmions in atomic thin CrI3 monolayer*, Appl. Phys. Lett. **114**, 232402 (2019).

[113] P. Jiang, L. Li, Z. Liao, Y. Zhao, and Z. Zhong. *Spin Direction-Controlled Electronic Band Structure in Two-Dimensional Ferromagnetic CrI3*, Nano Letters. **18**, 3844-3849 (2018).

[114] K. L. Seyler, D. Zhong, D. R. Klein, S. Gao, X. Zhang, B. Huang, E. Navarro-Moratalla, L. Yang, D. H. Cobden, M. A. McGuire, W. Yao, D. Xiao, P. Jarillo-Herrero, and Xiaodong Xu. *Ligand-field helical luminescence in a 2D ferromagnetic insulator*, Nat. Phys. **14**, 277 (2018).

[115] A. A. Pervishko, D. Yudin, V. Kumar Gudelli, A. Delin, O. Eriksson, and G.-Y. Guo. *Localized surface electromagnetic waves in CrI3-based magnetophotonic structures*, Optics Express. **28**, 20 (2020).

[116] A. Kudlis, I. Iorsh, and I.A. Shelykh. *All-optical resonant magnetization switching in CrI3 monolayers*, Phys. Rev. B. **104**, L020412 (2021).

[117] M. Onga, Y. Zhang, T. Ideue, and Y. Iwasa. *Exciton Hall effect in monolayer MoS2*, Nat. Mater. **16**, 1193 (2017).

[118] M. M. Glazov, and L. E. Golub. *Skew Scattering and Side Jump Drive Exciton Valley Hall Effect in Two-Dimensional Crystals*, Phys. Rev. Lett. **125**, 157403 (2020).

[119] V. K. Kozin, V. A. Shabashov, A. V. Kavokin, and I. A. Shelykh. *Anomalous Exciton Hall Effect*, Phys. Rev. Lett. **126**, 036801 (2021).

[120] C. Leyder, M. Romanelli, J. Ph. Karr, E. Giacobino, T. C. H. Liew, M. M. Glazov, A. V. Kavokin, G. Malpuech, and A. Bramati. *Observation of the optical spin Hall effect*, Nat. Phys. **3**, 628 (2007).

[121] Y.-M. Li, J. Li, L.-K. Shi, D. Zhang, W. Yang, and K. Chang. *Light-Induced Exciton Spin Hall Effect in van der Waals Heterostructures*, Phys. Rev. Lett. **115**, 166804 (2015).

[122] M. Wu, Z. Li, T. Cao, and S. G. Louie. *Physical origin of giant excitonic and magnetooptical responses in two-dimensional ferromagnetic insulators*, Nature Comm. **10**, 2371 (2019).

[123] Weng, Hongming, Xi Dai, and Zhong Fang. *From anomalous hall effect to the quantum anomalous hall effect*, arXiv preprint, 1509.05507 (2015).

[124] T. Olsen. *Unified Treatment of Magnons and Excitons in Monolayer CrI3 from Many Body Perturbation Theory*, Phys. Rev. Lett. **127**, 166402 (2021).

[125] S. Acharya, D. Pashov, A. N. Rudenko, M. Rösner, M. van Schilfgaarde, and Mikhail I. Katsnelson. *Real and momentum space description of the excitons in bulk and monolayer chromium tri-halides*, Npj 2D Mater. Appl. **6**, 33 (2022).

[126] J. J. Mortensen and L. B. Hansen and K. W. Jacobsen. *Real-space grid implementation of the projector augmented wave method*, Phys. Rev. B. **71**, 035109 (2005).

[127] J. Enkovaara, C. Rostgaard, J. J. Mortensen, J. Chen, M. Dułak, L. Ferrighi, J. Gavnholt, C. Glinsvad, V. Haikola, H. A. Hansen, H. H. Kristoffersen, M. Kuisma, A. H. Larsen, L. Lehtovaara, M. Ljungberg, O. Lopez-Acevedo, P. G. Moses, J. Ojanen, T. Olsen, V. Petzold, N. A. Romero, J. Stausholm-Møller, M. Strange, G. A. Tritsaris, M. Vanin, M. Walter, B. Hammer, H. Häkkinen, G. K. H. Madsen, R. M. Nieminen, J. K. Nørskov, M. Puska, T. T. Rantala, J. Schiøtz, K. S. Thygesen, and K. W. Jacobsen. *Electronic structure calculations with GPAW: a real-space implementation of the projector augmented-wave method*, J. Phys.: Condens. Matter. **22**, 253202 (2010).

[128] J. Yan, J. J. Mortensen, K. W. Jacobsen, and K. S. Thygesen. *Linear density response function in the projector augmented wave method: Applications to solids, surfaces, and interfaces*, Phys. Rev. B. **83**, 245122 (2011).

[129] T. Olsen. *Designing in-plane heterostructures of quantum spin Hall insulators from first principles: 1T'-MoS2 with adsorbates*, Phys. Rev. B. **94**, 235106 (2016).

[130] F. Huser, T. Olsen and K. S. Thygesen. *How dielectric screening in two-dimensional crystals affects the convergence of excited-state calculations: Monolayer MoS2*, Phys. Rev. B. **88**, 245309 (2013).

[131] Z. Levine, and D. Allan. *Linear optical response in silicon and germanium including self-energy effects*, Phys. Rev. Lett. **63**, 1719 (1989).

[132] X. Gonze, and C. Lee. *Dynamical matrices, Born effective charges, dielectric permittivity tensors, and interatomic force constants from density-functional perturbation theory*, Phys. Rev. B. **55**, 10355 (1997).

[133] K. S. Denisov, I. V. Rozhansky, N. S. Averkiev, and E. Lähderanta. *Electron Scattering on a Magnetic Skyrmion in the Nonadiabatic Approximation*, Phys. Rev. Lett. **117**, 027202 (2016).

[134] K. S. Denisov. *Theory of an electron asymmetric scattering on skyrmion textures in two-dimensional systems*, J. Phys. Condens. Matter. **32**, 415302 (2020).

[135] J. Dalibard, F. Gerbier, G. Juzeli ¯unas, and P. Öhberg. *Colloquium: Artificial gauge potentials for neutral atoms*, Rev. Mod. Phys. **83**, 1523 (2011).

[136] S. K. Adhikari. *Quantum scattering in two dimensions*, Am. J. Phys. **54**, 362 (1986).

[137] N. A. Sinitsyn, A. H. MacDonald, T. Jungwirth, V. K. Dugaev, and J. Sinova. *Anomalous Hall effect in a two-dimensional Dirac band: The link between the Kubo-Streda formula and the semiclassical Boltzmann equation approach*, Phys. Rev. B. **75**, 045315 (2007).

[138] Y. Aharonov, and D. Bohm. *Significance of Electromagnetic Potentials in the Quantum Theory*, Phys. Rev. **115**, 485 (1959).

[139] P. M. Buhl, F. Freimuth, S. Blügel, and Y. Mokrousov. *Topological spin Hall effect in antiferromagnetic skyrmions*, Phys. Status Solidi RRL. **11**, 1700007 (2017).

[140] C. A. Akosa, O. A. Tretiakov, G, Tatara, and A. Manchon, Theory of the Topological Spin Hall Effect in Antiferromagnetic Skyrmions: Impact on Current-Induced Motion, Phys. Rev. Lett. 121, 097204 (2018).

[141] B. Göbel, A. Mook, J. Henk, and I. Mertig. *Antiferromagnetic skyrmion crystals: Generation, topological Hall, and topological spin Hall effect*, Phys. Rev. B. **96**, 060406(R) (2017).

[142] B. Göbel, A. Mook, J. Henk, and I. Mertig. *The family of topological Hall effects for electrons in skyrmion crystals*, Eur. Phys. J. B. **91**, 179 (2018).

[143] Onida, Giovanni, Lucia Reining, and Angel Rubio. *Electronic excitations: density-functional versus many-body Green's-function approaches*, Reviews of modern physics. **74.2**, 601 (2002).

[144] Rohlfing, Michael, and Steven G. Louie. *Electron-hole excitations in semiconductors and insulators*, Physical review letters. **81.11**, 2312 (1998).

[145] Deilmann, Thorsten, Peter Krüger, and Michael Rohlfing. *Ab initio studies of exciton g factors: monolayer transition metal dichalcogenides in magnetic fields*, Physical review letters. **124.22**, 226402 (2020).

[146] Woźniak, Tomasz, et al. *Exciton g factors of van der Waals heterostructures from first-principles calculations*, Physical Review B. **101.23**, 235408 (2020).

[147] Lopez, M. G., et al. *Wannier-based calculation of the orbital magnetization in crystals*, Physical Review B. Condensed Matter and Materials Physics. **85.1**, 014435 (2012).

[148] Thonhauser, Timo, et al. *Orbital magnetization in periodic insulators*, Physical review letters. **95.13**, 137205 (2005).

[149] Ceresoli, Davide, et al. *Orbital magnetization in crystalline solids: Multi-band insulators, Chern insulators, and metals*, Physical Review B. Condensed Matter and Materials Physics. **74.2**, 024408 (2006).

[150] Mortensen, Jens Jørgen, Lars Bruno Hansen, and Karsten Wedel Jacobsen. *Real-space grid implementation of the projector augmented wave method*, Physical Review B. Condensed Matter and Materials Physics. **71.3**, 035109 (2005).

[151] Blöchl, Peter E. *Projector augmented-wave method*, Physical review B. **50.24**, 17953 (1994).